ASTRONOMICAL INSTITUTE
SLOVAK ACADEMY OF SCIENCES

CONTRIBUTIONS OF THE ASTRONOMICAL OBSERVATORY SKALNATÉ PLESO

• VOLUME LVI •

Number 3

August 2026

ISSN: 1336–0337 (on-line version)

CODEN: CAOPF8

Editorial Office: Astronomical Institute of the Slovak Academy of Sciences
SK - 059 60 Tatranská Lomnica, The Slovak Republic

CONTENTS

SOLAR SYSTEM

STARS

The Contributions of the Astronomical Observatory Skalnaté Pleso
are available in the full version
in the frame of ADS Abstract Service
and can be downloaded in a usual way from the URL address:

https://ui.adsabs.harvard.edu/

as well as from the website of
the Astronomical Institute of the Slovak Academy of Sciences
on the URL address:

https://www.astro.sk/caosp/caosp.php

The journal is covered/indexed by:

Web of Science (WoS)
WoS Core Collection: Science Citation Index Expanded

SCOPUS

Index Copernicus International

Contrib. Astron. Obs. Skalnaté Pleso **56/3**, 5 – 23, (2026)
https://doi.org/10.31577/caosp.2026.56.3.5

Shape model and dynamical state of the asteroid (300) Geraldina: Implications for its possible ancient origin

G. Apostolovska[1], **N. Todorović**[2], **E. Vchkova Bebekovska**[1], **G. Borisov**[3], **A. Kostov**[3] and **Z. Donchev**[3]

[1] *Institute of Physics, Faculty of Science, Ss. Cyril and Methodius University in Skopje, Arhimedova 3, 1000 Skopje, Republic of Macedonia (E-mail: gordanaapostolovska@gmail.com)*

[2] *Astronomical Observatory, Volgina 7. P.O. Box 74, 11060 Belgrade, Serbia*

[3] *Institute of Astronomy and National Astronomical Observatory, Bulgarian Academy of Sciences, Tsarigradsko Chaussee Blvd. 72, BG-1784, Sofia, Bulgaria*

Received: February 19, 2026; Accepted: March 27, 2026

Abstract. In this study, we present a comprehensive photometric and physical characterization of the main-belt asteroid (300) Geraldina. Our analysis includes determining its sidereal rotational period, shape modeling, spin-axis orientation, as well as dynamical and spectral properties. The investigation is based on two decades of archival photometry from the Bulgarian National Astronomical Observatory (BNAO) Rozhen, complemented by dense CCD lightcurve observations obtained since 2017 at the Astronomical Station Vidojevica (ASV), dense data from ALCDEF, and augmented with sparse-in-time measurements from Gaia Data Release 3 (DR3). By combining these heterogeneous datasets within and using the lightcurve inversion method, we confirmed the asteroid's prograde sense of rotation and obtained two symmetrically mirrored pole solutions for the asteroid model. Our dynamical studies show that (300) Geraldina remains stable in 100 Myr. Although close to the 2:1 mean-motion resonance with Jupiter, it is not captured into it during the observed time. Instead, it exhibits interactions with an unidentified high-order mean-motion resonance, which appears to contribute to its long-term stability. Its spectral type (C) with a primitive carbonaceous composition, in combination with low albedo and long-term stability, is consistent with the assumption that (300) Geraldina is an ancient asteroid.

Key words: (300) Geraldina – photometry – dynamical properties – spectroscopy

1. Introduction

Determining the asteroid model is an important step for further investigation of the evolution, dynamics, and future of our Solar System. Although the number of asteroids with known models is steadily increasing, it still represents only a small fraction of the total known asteroid population (about 0.8%). Specifically, out of 1,298,026 objects listed in the AstDyS[1] database, only 10,758 have shape models available in the DAMIT[2] database (in December 2025). Having an asteroid with a known model means that both synodic and siderial periods, as well as the coordinates of its axis of rotation, the sense of rotation, and its shape, are known.

Most asteroids observed today are believed to be fragments of larger parent bodies that were disrupted in past collisional events. These fragments typically remain near the original parent body until dynamical processes gradually drift them away. Such groups of related objects are known as asteroid families, in which the largest member is usually considered the remnant of the original body. Studying asteroid models helps in the reconstruction of these collisional events, and also improves our understanding of the dynamical evolution of the Solar System as a whole. By 2015, a total of 122 asteroid families had been confirmed (Nesvorný et al., 2015), and this number remained relatively unchanged until 2024, when Nesvorný et al. (2024) discovered more than 150 new collisional main belt families. Combined with Trojans and other families outside the main belt, the current number of known asteroid families exceeds 300. However, only three families are estimated to have an age of more than 3 Gyr, originating from ancient asteroids.

The asteroid (300) Geraldina, discovered in 1890 by Auguste Charlois, is an outer main-belt asteroid and is considered a possible member of the so-called ancient asteroid population. These bodies are regarded as primordial remnants of the early Solar System and are therefore of particular interest for studies of the collisional and dynamical history of the main belt. The reported diameter in the MP3C database[3], varies from 66.78 km (Masiero et al., 2012) to 91.56 km (Nugent et al., 2016), whereas the reported albedo ranges from 0.03 (Nugent et al., 2016) to 0.06 (Masiero et al., 2014). A relatively large size, lack of association with any known asteroid family, and a low albedo, make (300) Geraldina a strong candidate for a pristine main-belt object - an ancient asteroid (Delbo' et al., 2017; Ferrone et al., 2023; Athanasopoulos et al., 2022, 2024).

According to the first studies on the rotation of this asteroid, it is derived that its synodic period is 6.818 h (Ivanova et al., 2002). Later, a few more studies have been conducted on the ligthcurve of asteroid (300) Geraldina, and all of them show similar values for its rotational period. The latest value given in the

[1] https://newton.spacedys.com/astdys2/index.php?pc=1.0.0
[2] https://damit.cuni.cz/
[3] Available at https://mp3c.oca.eu/

JPL Database is 6.8423 h. Klinglesmith & Hendrickx (2018) suggested a possible bimodal period of 13.726 h.

Currently, the model of this asteroid is unknown. The only suggestion so far is given by Romanishin (2024), indicating the possibility of a binary asteroid, specifically a contact binary or an elongated single object. Still, this suggestion was based on three observational nights during one opposition, which can not provide sufficient data points for a clear statement. To construct the asteroid's model, we need photometric observations from several different oppositions, to collect data from various parts of the asteroid's surface and piece them together like a puzzle to form a picture; typically, this requires more than five observing nights, over a longer time period, and much more if the asteroid has an irregular shape. To decrease the observational time on the ground-based telescopes, photometric dense data can be combined with sparse data from space missions like NEOWISE or GAIA. While dense data from a single observational night allows us to collect hundreds of photometric points (Bebekovska et al., 2019, 2023; Apostolovska et al., 2023), sparse data are rare in time and typically provide only a few points (usually 5) per observational night, but can cover parts of the asteroid that have not been observed during the ground-based observations.

2. Instrumentation

Observations of (300) Geraldina were performed during a time span of 23 years. In this period, five different telescopes located in two observatories were used. The campaign began at the Bulgarian National Astronomical Observatory (BNAO) Rozhen, Bulgaria, with the 2m Ritchey-Chrétien-Coude (RCC) telescope, the main instrument of the observatory. The telescope is equatorial mounted, and has two optical systems: Ritchey-Chrétien (for optical observations) and Coude (for spectroscopic observations). The main mirror is two meters in diameter, the focal length is 16 m. The second telescope of BNAO is the 50/70cm Schmidt Telescope - equatorial mounted Schmidt system with 70 cm mirror and 50 cm diameter of the correction plate, and a focal length of 172 cm. The third is the 60cm Cassegrain telescope - equatorial mounted Cassegrain optical system with a main mirror of 60 cm in diameter and a focal length of 7.5 m.

The Astronomical Station Vidojevica (ASV), Serbia, participated with two more telescopes. The first one is the 1.4m Milanković telescope - alt-azimuthal mounted Ritchey-Chrétien system with main mirror of 1.4 m in diameter, and focal length of 11.2 m. The second instrument of the observatory is the 60cm Cassegrain Nedeljković telescope - equatorial mounted Cassegrain optical system with main mirror of 60 cm in diameter, and focal length of 6 m.

The detectors of the telescopes, the component of the observational system that is most frequently updated, were also changed during the observational campaign, leading to 8 different CCD's used in total. In Tab. 1 all these CCD's are listed. In the first column is the observational run (or period) in which the detector was used, followed by the telescope, where that CCD was attached, chip size in pixels, and the physical dimension of the pixel in μm.

Table 1. Instrumentation used in the observational campaign

Run	Telescope	CCD Detector Model	Chip size [px]	Pixel size [μm]
2002 Jan	2mRCC	Photometrics CE200A-SITe	1024 x 1024	24
2003 Apr	5070	SBIG ST-8E	1520 x 1020	9
2008 Jan	5070	SBIG STL-11000M	4008 x 2672	9
2009 ÷ 2010	5070	FLI PL16803	4096 x 4096	9
2011 ÷ 2023	60CAS	FLI PL09000	3056 x 3056	12
2017 Oct	EQ60	Apogee U42	2048 x 2048	13.5
2018 ÷ 2025	AZ1400	Andor iKon-L 936	2048 x 2048	13.5
2023 Oct	EQ60	FLI PL23042 MB	2048 x 2048	15

Notes: The telescope abbreviations are as follows: 2mRCC = 2m Ritchey-Chrétien-Coude (RCC) telescope of BNAO Rozhen; 5070 = 50/70cm Schmidt telescope of BNAO Rozhen; 60CAS = 60cm Cassegrain telescope of BNAO Rozhen; EQ60 = 60cm Cassegrain Nedeljković telescope of AS Vidojevica; AZ1400 = 1.4m Milanković telescope of AS Vidojevica

3. Observations and data reduction

Our first observations of (300) Geraldina were conducted over two consecutive nights, 10/11 and 11/12 January 2002, using the 2m telescope at BNAO Rozhen. In Tab. 2 the physical parameters such as diameter, absolute magnitude, albedo, and orbital parameters of (300) Geraldina are shown (as can be found in the JPL Small-Body Database Browser and Asteroid Light Curve Database[4]).

Table 2. Asteroid parameters

Asteroid	D (km)	H (mag)	Albedo	a (AU)	e	i (°)
(300) Geraldina	67.37	9.76	0.052	3.20	0.06	0.73

From the acquired photometric data, we derived—for the first time in the case of this asteroid—a synodic rotation period of 6.818 hours and amplitude of 0.317 mag (Ivanova et al., 2002). Licchelli (2006) from his observations in 2005 calculated a more precise rotational period of 6.842 h.

[4]https://ssd.jpl.nasa.gov/tools/sbdb_lookup.html

The next observations at BNAO Rozhen were performed with the 50/70cm Schmidt telescope and with the 60cm Cassegrain telescope. Since 2017, Geraldina was observed at Astronomical Station Vidojevica with the 1.4m Milanković telescope and 60cm Cassegrain Nedeljković telescope. The larger Milanković telescope was installed in 2016, and asteroids Geraldina and O'Steen were among the first targets observed with it, to determine their shapes (Todorović et al., 2020). During 2002 and 2003, photometric observations were done in the standard Johnson–Cousins V band and all others in the R band.

Table 3. Aspect data for the asteroid (300) Geraldina

Date (UT)	r (AU)	Δ (AU)	α (°)	$PLON$ (°)	$PLAT$ (°)	Filter	Note
2002 Jan 11.01	3.368	2.406	9.39	138.74	0.88	V	2mRCC
2002 Jan 12.01	3.276	2.399	9.09	138.76	0.88	V	2mRCC
2003 Apr 28.92	3.368	2.381	4.02	206.59	0.22	V	5070
2003 Apr 29.96	3.367	2.384	4.37	206.57	0.22	V	5070
2003 Apr 30.90	3.367	2.387	4.68	206.56	0.21	V	5070
2008 Jan 09.08	3.319	2.656	14.06	155.98	0.81	R	5070
2008 Jan 09.92	3.319	2.644	13.87	156.04	0.81	R	5070
2008 Jan 11.02	3.320	2.633	13.68	156.11	0.81	R	5070
2009 Apr 24.05	3.353	2.363	3.66	224.28	0.00	R	5070
2009 Apr 25.06	3.353	2.360	3.31	224.27	0.00	R	5070
2010 Jul 13.94	3.161	2.150	2.30	297.25	-0.88	R	5070
2010 Jul 14.98	3.161	2.148	1.94	297.24	-0.88	R	5070
2010 Aug 17.83	3.144	2.241	9.90	297.34	-0.88	R	5070
2011 Oct 30.96	3.037	2.078	5.90	21.62	-0.29	R	60CAS
2011 Nov 29.81	3.040	2.327	14.70	22.93	-0.19	R	60CAS
2011 Nov 30.81	3.040	2.338	14.91	23.01	-0.18	R	60CAS
2012 Nov 12.08	3.178	2.566	15.66	102.12	0.6	R	60CAS
2012 Nov 13.95	3.179	2.545	15.33	102.28	0.65	R	60CAS
2012 Dec 13.04	3.195	2.283	7.85	103.58	0.74	R	60CAS
2013 Jan 08.85	3.210	2.230	1.90	103.33	0.79	R	60CAS
2014 Mar 30.94	3.380	2.423	5.70	173.15	0.64	R	60CAS
2017 Oct 20.08	3.050	2.101	6.79	44.44	-0.03	R	EQ60
2018 Dec 04.01	3.248	2.612	14.87	121.75	0.79	R	60CAS
2018 Dec 07.11	3.250	2.576	14.29	121.98	0.79	R	60CAS
2018 Dec 12.97	3.252	2.513	13.06	122.34	0.81	R	AZ1400
2020 Feb 28.02	3.387	2.546	10.21	190.79	0.51	R	60CAS
2020 Apr 18.96	3.386	2.434	6.36	190.33	0.43	R	2mRCC
2023 Oct 07.04	3.088	2.462	16.25	64.82	0.20	R	EQ60
2023 Oct 15.00	3.092	2.374	14.70	65.52	0.22	R	60CAS
2025 Mar 05.90	3.350	2.449	8.33	140.08	0.84	R	AZ1400

Notes: In the last column, the telescope abbreviations are the same, as in Tab. 1

Geraldina was observed 30 nights during 13 oppositions over more than two decades from 2002 to 2025. In Tab. 3, the aspect data of (300) Geraldina during our observations are reported. The first column is the date of the observation referring to the mid–time of the observed lightcurve. In the other columns are as follows: asteroid distance from the Sun (r), distance from the Earth (Δ), Phase Angle (α) (the Sun-Asteroid-Observer angle), Phase Angle Bisector Longitude ($PLON$) and Phase Angle Bisector Latitude ($PLAT$) of the asteroid referred to the time in the first column, the broadband filter in which the observations were carried. The last column is a note on the telescope used to acquire images, and an explanation of the abbreviations can be found at the bottom of Tab. 1.

From the Asteroid Light Curve Data Exchange Format (ALCDEF)[5] database (Stephens & Warner, 2018), for (300) Geraldina, we collected dense photometric data from two LCs from Waszczak et al. (2015) and six LCs from Polakis (2018). Sparse data correspond to 37 photometric points from 11 August 2014 to 02 January 2017 from GAIA Data Release 3 (DR3) (Gaia Collaboration et al., 2023; Tanga et al., 2023). Our dense photometric data provide broad coverage of the phase-angle bisector (PAB) longitude distribution, while the Gaia sparse data largely overlap with already sampled regions of the PAB longitude range (Fig. 1).

The data were reduced using standard bias and flat-field corrections, followed by aperture photometry using CCDPHOT by Buie (1996).

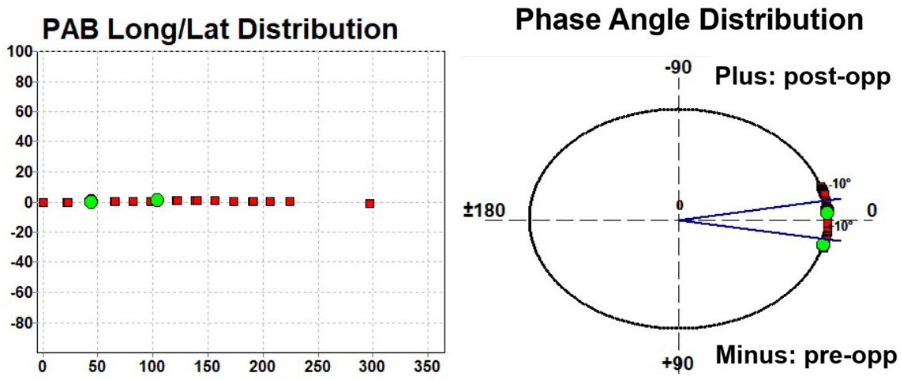

Figure 1. Left: Distribution of PAB longitude vs PAB latitude; Right: Distribution of the phase angle. On each of the two plots, the red and green points represent the dense and GAIA DR3 sparse observations, respectively.

[5]https://alcdef.org/

4. Results

4.1. Lightcurve analysis

Lightcurves obtained during three different oppositions are presented in Fig. 2, Fig. 3, and Fig. 4, illustrating how both the shape of the lightcurve and the amplitude change between apparitions.

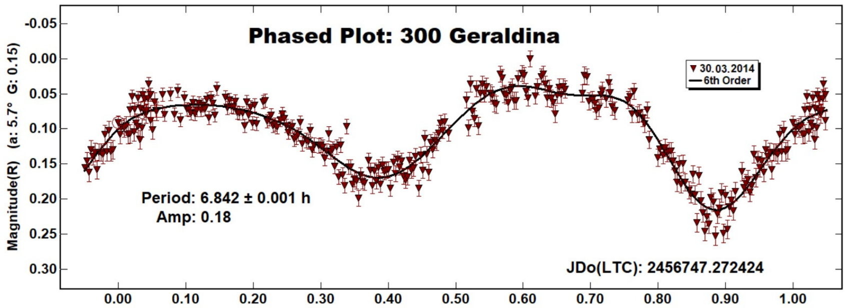

Figure 2. The single-night lightcurve of (300) Geraldina was obtained from observations carried out on 30 March 2014. Fourier analysis of the lightcurve, constructed using the accepted rotational period of 6.842 h and a 6^{th}order Fourier fit, yielded an amplitude of 0.18 mag.

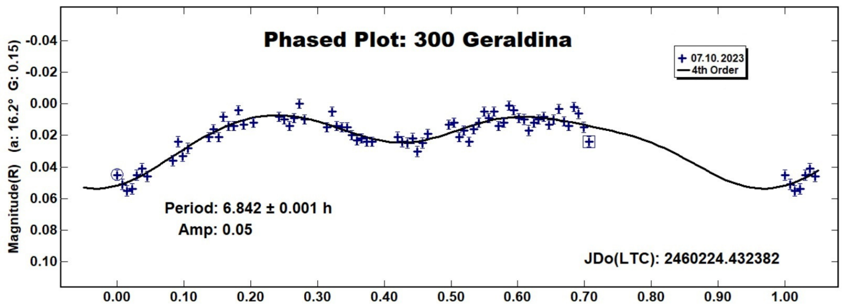

Figure 3. The single-night lightcurve of (300) Geraldina was obtained from observations carried out on 7 October 2023. Fourier analysis of the lightcurve, constructed using the accepted rotational period of 6.842 h and a 4^{th}order Fourier fit, yielded an amplitude of 0.05 mag.

For the determination of a shape model, we used the lightcurve inversion method (Kaasalainen & Torppa, 2001; Kaasalainen et al., 2001) and the LCInvert programme, part of the MPO Software. Considering the high accuracy of

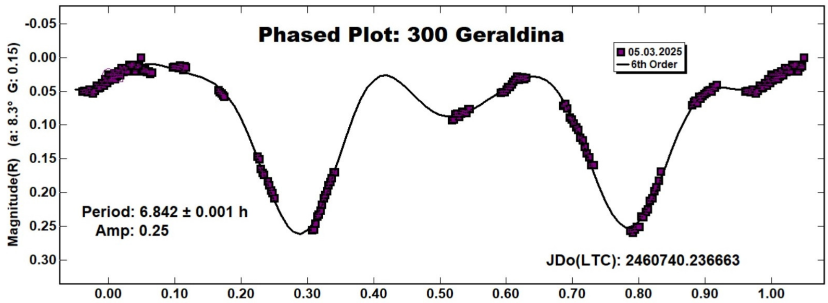

Figure 4. The single-night lightcurve of (300) Geraldina was obtained from observations carried out on 5 March 2025. Fourier analysis of the lightcurve, constructed using the accepted rotational period of 6.842 h and a 6^{th}order Fourier fit, yielded an amplitude of 0.25 mag.

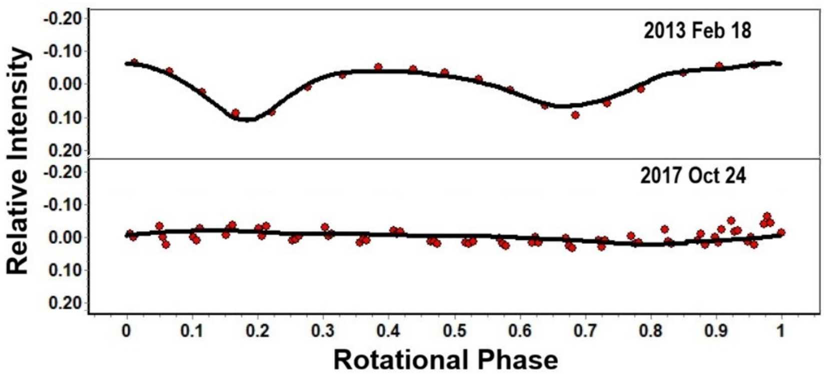

Figure 5. The observed lightcurves derived from available published data from ALCDEF from 2013 and from 2017 (red points) for selected nights are shown superimposed on the synthetic lightcurves generated by the shape–spin model obtained through a combined inversion of all dense datasets and the GAIA DR3 sparse photometry.

the DR3 photometric data, we took the weighting factor to be set to 1.0 for both sparse and for dense photometric data. The rotational period was determined using a light-curve inversion method that fits a simple 3D shape model to the data, instead of standard Fourier techniques. The best period was selected by minimizing the χ^2 value computed for the modeled and observed light curves. The analysis was carried out with the DAMIT software package (Kaasalainen et al., 2001; Durech et al., 2010). Trial periods were scanned over a wide range using the *period_scan* routine, testing six initial pole solutions for each trial

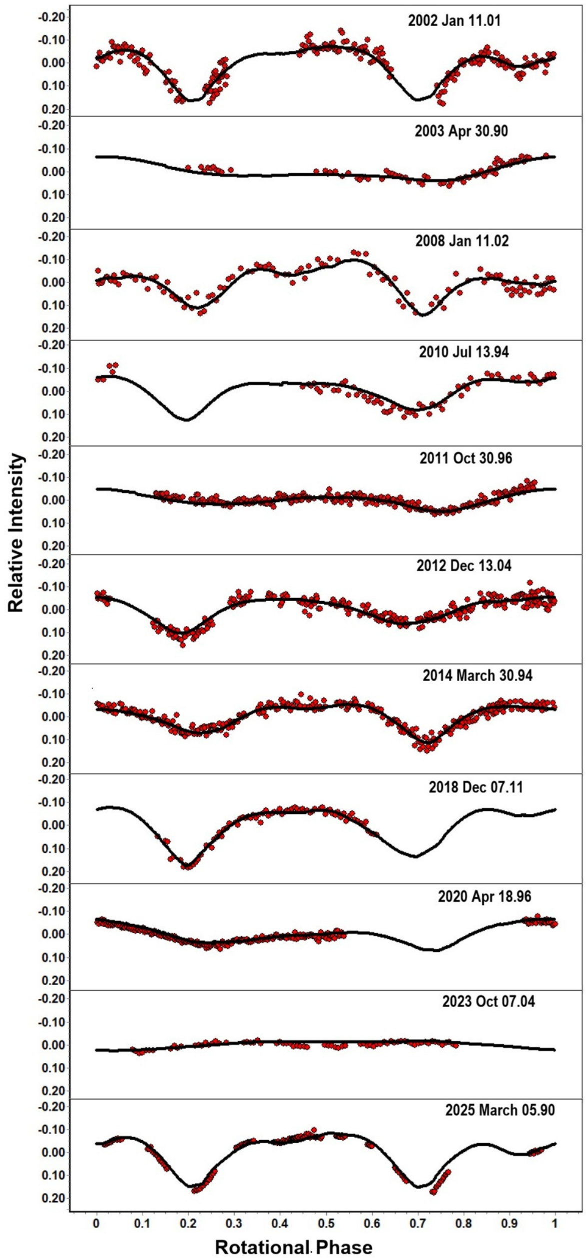

Figure 6. The observed lightcurves derived from our dense photometric measurements (red points) for selected nights are shown superimposed on the synthetic lightcurves generated by the shape–spin model obtained through a combined inversion of all dense datasets and the GAIA DR3 sparse photometry.

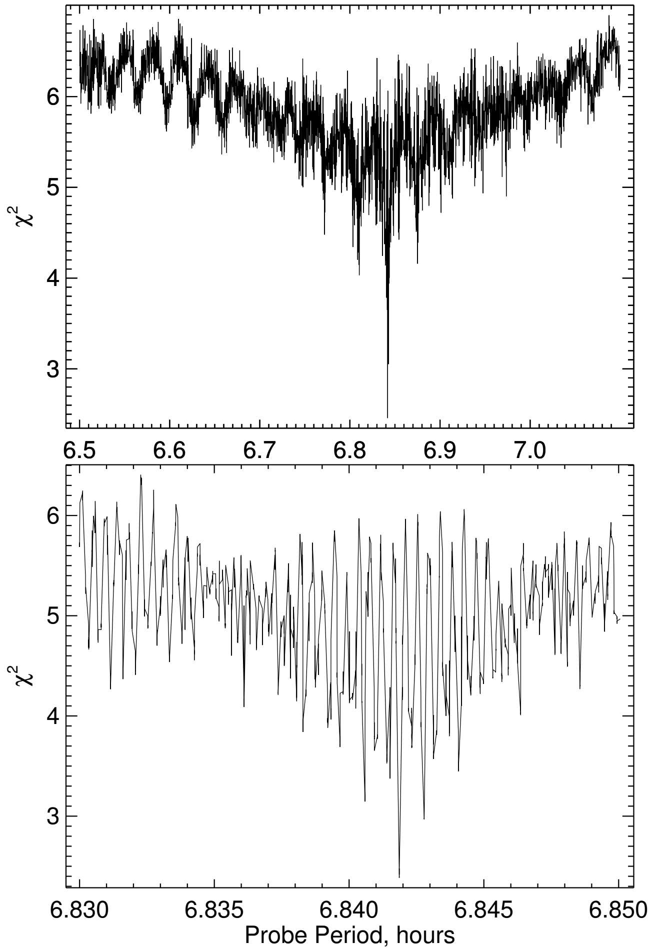

Figure 7. χ^2 vs probe period plot used for a period search (top panel) and the same plot but zoomed around the best solution with the lowest χ^2 value (bottom panel)

period, to ensure that the global χ^2 minimum was found.

We made the initial sidereal period search around 6.8 h within the interval of ± 0.3 h (see Fig. 7 top panel). Several solutions with 10% of the lowest ± 2 value were found, but a narrower period search found that the most likely period is 6.84186100 h (see Fig. 7 bottom panel.)

The pole search produced 312 discrete and fixed pole positions distributed over the unit sphere with 15° steps in ecliptic latitude and longitude, varying also the most likely input period. The resulting solutions were used to construct χ^2 maps (Fig. 8), which allowed the identification of low-χ^2 regions and the selection of the best-fitting pole. As it is expected for asteroids with orbits close to the ecliptic plane, we encounter two symmetric pole solutions with identical β and $\lambda \pm 180°$. The preliminary ecliptic coordinates for the pole are $\lambda = 45 \pm 7.5°$, $\beta = 15 \pm 7.5°$ and for the mirrored pole solution are $\lambda = 225 \pm 7.5°$, $\beta = 15 \pm 7.5°$ which suggest prograde sense of asteroid rotation. The finest search centered on these roughly obtained pole positions gave us more precisely determined solutions, presented in Tab. 4. The derived three-dimensional shape model of the asteroid (300) Geraldina is presented in Fig. 9, and the observed and synthetic (derived from the model) lightcurves are presented in Fig. 5 and Fig. 6.

Table 4. Parameters of the model of the asteroid (300) Geraldina

Sideral period (h)	Sense of rotation	Pole λ (°)	Pole β (°)	a/b	a/c	b/c
6.8418615	P	52.6 ± 5.0	9.5 ± 5.0	1.11	1.29	1.16
6.8418615	P	232.6 ± 5.0	9.1 ± 5.0	1.11	1.29	1.16

Assuming the asteroid as a triaxial ellipsoid, rotating around the shortest axis $c = 1 \quad (a > b > c)$, we derived relative shape dimensions $a/c = 1.29$. The Tab. 4 gives the sidereal rotational period, sense of rotation (P for prograde),

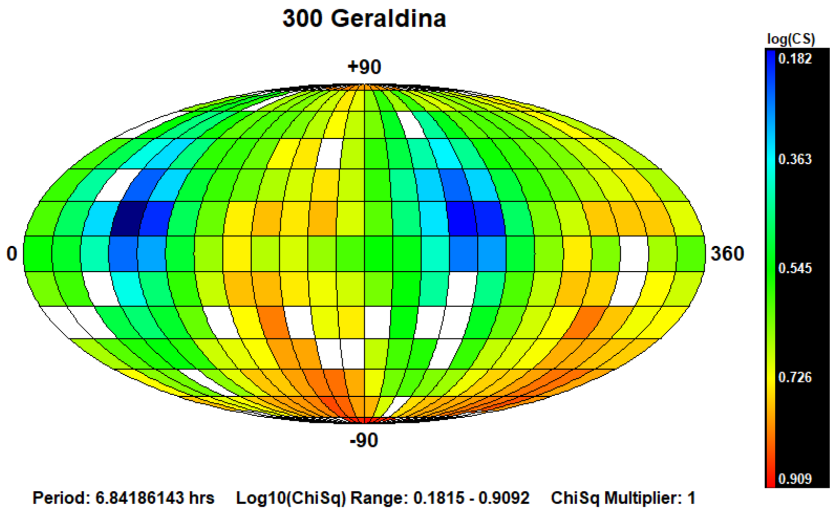

Figure 8. Pole search distribution. The dark blue regions have the smallest value of χ^2.

ecliptic coordinates λ and β of the two mirror solutions, and rough relative shape dimensions.

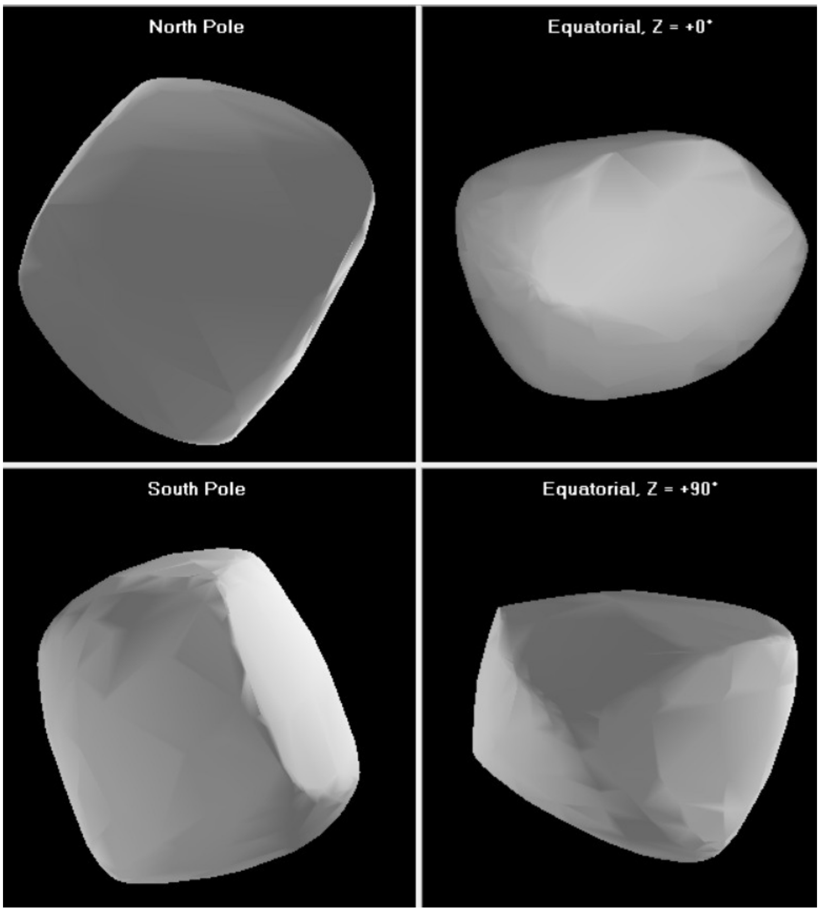

Figure 9. The three-dimensional low-resolution convex shape model of the asteroid (300) Geraldina is shown. The left panels present views of the model from the north and south rotational poles, illustrating the overall polar morphology. The right panels display equatorial perspectives separated by 90° in rotational phase, highlighting variations in the projected shape and allowing assessment of the object's elongation and symmetry during rotation.

Using the maximum observed lightcurve amplitude reported by Ivanova et al. (2002), and applying the empirical relation for C-type asteroids proposed by Zappala et al. (1990), we calculated the ratio of the maximum to minimum projected reflecting surface areas during the asteroid's rotation, as done in Vchkova

Bebekovska et al. (2021) and Borisov et al. (2024), obtaining $a/c = 1.39$. None of the composite lightcurves raises a suspicion that this might be a binary asteroid as suggested by Romanishin (2024). The minima have approximately the same depths and are separated by half a phase. If (300) Geraldina were a binary asteroid, its lightcurve should have a more irregular shape, as in the case of the suspected binary (12499) 1998 FR47 (Borisov et al., 2024).

4.2. Taxonomy from Gaia spectroscopy

The Gaia mission has been observing Solar System objects since the beginning of its operation, and the mean reflectance spectra of selected asteroids are included in its 3rd data release (DR3). As the asteroid (300) Geraldina is among the asteroids with reflectance spectra in DR3, we will use it in order to obtain its taxonomy and composition, relying on the new probabilistic approach by Mahlke et al. (2022).

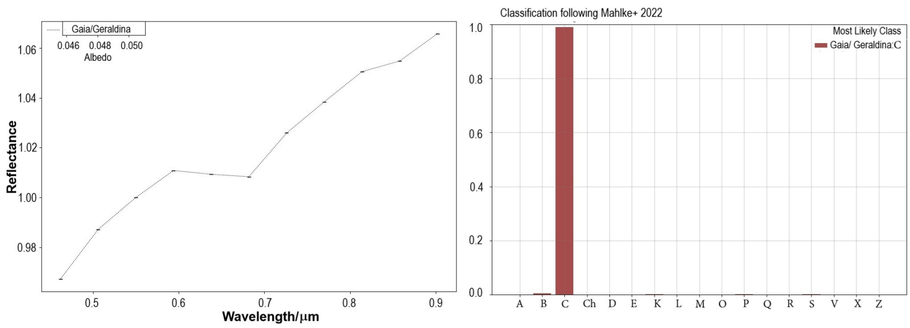

Figure 10. Gaia DR3 reflectance spectrum of (300) Geraldina and its taxonomical classification according to Mahlke et al. (2022) (see text for details).

The results are shown in Fig. 10. The left panel shows the Gaia DR3 reflectance spectra of the object, and the right panel presents the possible taxonomy classes with their probabilities. In particular, the asteroid (300) Geraldina has a 99% probability of being a C-class object and 1% for a B-class. Both of these solutions fall into classes that are primitive carbonaceous. The previous taxonomy determination shows the same classification (Carvano et al., 2010). This data set contains Sloan Digital Sky Survey (SDSS) asteroid photometric observations classified according to the SDSS-based Asteroid Taxonomy, as developed by Carvano et al.. Taking into account its reported very low albedo - 0.0331 (Carvano et al., 2010) may also lead to the idea that this object could be an "ancient asteroid"!

4.3. Dynamical properties of the asteroid (300) Geraldina

Dynamical properties of the asteroid (300) Geraldina are studied in two ways. First, we integrated the asteroid over the time span of 100 Myrs with the Orbit9 software[6], incorporating all the planets in the Solar system model. One common way to observe whether an asteroid has undergone dynamical evolution is to track changes in its semi-major axis.

Our results (see Fig. 11) show that (300) Geraldina is a stable asteroid. Its semi-major axis (a) exhibits only local oscillations ranging between a=[3.206, 3.209] AU, along with several sporadic resonant captures that stabilize the asteroid even more. In Fig. 11, these resonant episodes are visible as time intervals where the oscillation amplitudes are smaller. Before approximately 67 Myrs, the longest stays in the resonance are on the order of 100 Kyrs. After $\sim$ 67 Myrs, they become longer, with the final and longest resonant episode lasting from 90.3 Myr to the end of the integration.

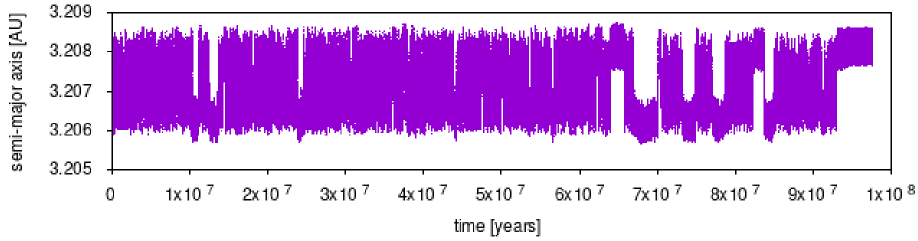

Figure 11. The stability of the asteroid (300) Geraldina over 100 Myrs shown through the evolution of its semi-major axis a. The asteroid remains stable, exhibiting only local oscillation in a, with several resonant captures (visible as intervals with oscillations of smaller amplitudes) that stabilize the asteroid even more. These captures became more frequent and lasted longer after 67 Myrs.

We also investigated the dynamical environment of the asteroid. Fig. 12 shows an Fast Lyapunov Indicator - FLI map (Froeschlé et al., 1997a,b; Borisov et al., 2024; Todorović, 2017), illustrating the stability properties within a portion of the orbital plane surrounding the asteroid, defined by $[a \times e] = [3.1\text{AU}, 3.4\text{AU}] \times [0, 0.1]$. The position of (300) Geraldina at $(a, e) = (3.204\text{AU}, 0.057)$ is indicated by a white dot, while the remaining orbital elements—the inclination i, longitude of the ascending node Ω, argument of perihelion ω, and mean anomaly M—are set equal to those of Geraldina at epoch JD 2458800.5, obtained from NASA's JPL Horizons system[7]. This choice of orbital parameters provides a realistic representation of the dynamical environ-

[6]http://adams.dm.unipi.it/orbfit/

[7]https://ssd.jpl.nasa.gov/horizons.cgi

ment around the asteroid. The map was computed using the Orbit9 integrator over a timespan of 5,000 years, adopting a full Solar System model.

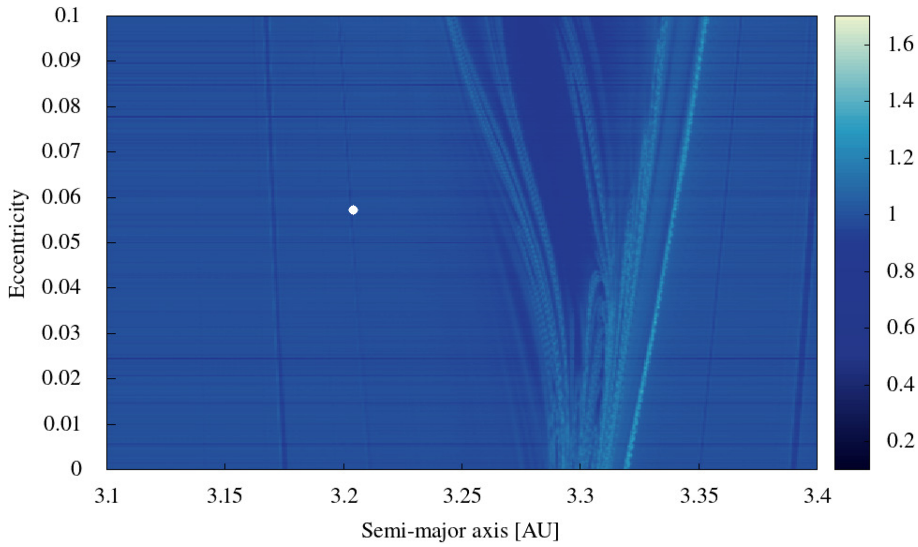

Figure 12. The FLI map showing the dynamical neighborhood of the asteroid (300) Geraldina (marked with a white dot). Lighter colors reveal instabilities, while darker shades of blue represent stable regions. The most dominant structure revealing instability appears around 3.3 AU, and represents one of the strongest resonances in the Solar system - the 2:1 MMR with Jupiter. Although relatively close, (300) Geraldina has not been captured by this resonance during 100 Myrs. The only resonant behavior of the asteroid is observed within a weak high-order MMR, visible on the map as a thin vertical line at about $a \sim 3.21$ AU.

Each point on Fig. 12 represents one orbit. Pixels colored in light blue represent orbits that have shown instabilities during 5000 years, while the darker shades show stable regions. The most dominant structure on the map is noticeable at 3.3 AU. It represents the trace of one of the strongest resonances in the Solar system, the 2:1 mean motion resonance (MMR) with Jupiter (Chrenko et al., 2015; Brož et al., 2005a). Although (300) Geraldina lies relatively close to this resonance, it has not been driven toward it during the 100 Myr integration (see changes in a in Fig. 11). Let us mention that the integration does not include the Yarkovsky effect, which could, in principle, cause an asteroid to drift into the resonance (Brož et al., 2005b). However, large asteroids, such as Geraldina, are, in general, not significantly affected by the Yarkovsky force.

Several thin and pale vertical lines in Fig. 12 represent unidentified high-order MMRs. They are not strong enough to make any significant change in the orbital evolution of an asteroid. Geraldina appears to be on one such resonance. The changes of its semi-major axis shown in Fig. 11 do reveal a resonant behavior, but as mentioned above, it was not strong enough to provide any significant shift of the asteroid. This weak MMR only contributed to the stabilization of the asteroid. Geraldina's dynamical stability, although not evaluated over a full 4 billion–year timescale, may provide additional evidence of its pristine nature.

5. Conclusions

We have presented a combined photometric, spectroscopic, and dynamical analysis of the main-belt asteroid (300) Geraldina, using dense ground-based lightcurves spanning more than two decades, complemented by available published data from ALCDEF and by sparse Gaia DR3 photometry. Application of the lightcurve inversion method yielded a well-constrained sidereal rotation period of 6.8418615 h, a prograde sense of rotation, and two mirror pole solutions consistent with the asteroid's low orbital inclination. The derived convex shape model indicates a moderately elongated body. Gaia DR3 reflectance spectroscopy classifies (300) Geraldina as a C-type asteroid, consistent with a primitive, carbonaceous composition. Together with its reported low albedo, this supports its classification as an ancient asteroid candidate.

Numerical integrations over 100 Myr show that (300) Geraldina remains dynamically stable. Despite its proximity to the 2:1 mean-motion resonance with Jupiter, no resonance capture is observed, and the asteroid instead exhibits weak interactions with a high-order mean-motion resonance without much influence on its long-term orbital evolution.

Taken together, the physical, rotational, taxonomic, and dynamical properties of (300) Geraldina support the hypothesis that it is a primordial asteroid. These results make (300) Geraldina a valuable target for further studies of the primordial collisional and dynamical evolution of the asteroid belt.

Acknowledgements. This article is based on data collected with the telescopes of the Rozhen National Astronomical Observatory. The authors gratefully acknowledge observing grant support from the Institute of Astronomy and Rozhen National Astronomical Observatory, Bulgarian Academy of Science. The research that led to these results was partially carried out with the help of infrastructure purchased under the National Roadmap for Research Infrastructure, financially coordinated by the Ministry of Education and Science of Republic of Bulgaria. G.B. and A.K. acknowledge partial support by grant: КП-06-Н88/5 "Physical properties and chemical composition of asteroids and comets - a key to increasing our knowledge of the Solar System origin and evolution." by the Bulgarian Scientific Research Fund of the Ministry of Education and Science. The observations at AS Vidojevica and funding for N.T. were financed from the Ministry of Science, Technological Development and Innovation of the Republic of Serbia, under the contract number 451-03-33/2026-03/200002. The authors are grateful to D. Athanasopoulos for valuable discussions and insights on ancient asteroids. The authors gratefully acknowledge Violeta Ivanova, Bonka Bilkina, and Vasko Umlenski for their contribution to the observational data collected at the National Astronomical Observatory Rozhen and used in this study.

References

Apostolovska, G., Todorović, N., & Vchkova Bebekovska, E., Lightcurve Analysis of Asteroids at the Astronomical Station Vidojevica for the first half of 2022. 2023, in *11th International Conference of the Balkan Physical Union*, 41

Athanasopoulos, D., Hanuš, J., Avdellidou, C., et al., Asteroid spin-states of a 4 Gyr collisional family. 2022, *Astronomy and Astrophysics*, **666**, A116, DOI:10.1051/0004-6361/202243905

Athanasopoulos, D., Hanuš, J., Avdellidou, C., et al., Spin states of X-complex asteroids in the inner main belt: I. Investigating Athor and Zita collisional families. 2024, *Astronomy and Astrophysics*, **690**, A215, DOI:10.1051/0004-6361/202451363

Bebekovska, E. V., Apostolovska, G., Kostov, A., & Donchev, Z., Lightcurve analysis on asteroids from NAO Rozhen observations in 2021. 2023, in *11th International Conference of the Balkan Physical Union*, 39

Bebekovska, E. V., Kostov, A., Donchev, Z., & Apostolovska, G., Asteroid photometry in 2017 from national astronomical observatory Rozhen. 2019, in American Institute of Physics Conference Series, Vol. **2075**, *10th Jubilee International Conference of the Balkan Physical Union* (AIP), 090016

Borisov, G., Todorović, N., Vchkova-Bebekovska, E., Kostov, A., & Apostolovska, G., The possible dual nature of the asteroid (12499) 1998 FR47. 2024, *Contributions of the Astronomical Observatory Skalnate Pleso*, **54**, 57, DOI:10.31577/caosp.2024.54.4.57

Brož, M., Vokrouhlický, D., Roig, F., et al., The population of asteroids in the 2:1 mean motion resonance with Jupiter revised. 2005a, in *IAU Colloquium 197: Dynamics of Populations of Planetary Systems*, ed. Z. Knežević & A. Milani, 179–186

Brož, M., Vokrouhlický, D., Roig, F., et al., Yarkovsky origin of the unstable asteroids in the 2/1 mean motion resonance with Jupiter. 2005b, *Monthly Notices of the RAS*, **359**, 1437, DOI:10.1111/j.1365-2966.2005.08995.x

Buie, M. W., CCDPHOT—An IDL Widget Based CCD Photometry Reduction System. 1996, in Astronomical Society of the Pacific Conference Series, Vol. **101**, *Astronomical Data Analysis Software and Systems V*, ed. G. H. Jacoby & J. Barnes, 135

Carvano, J. M., Hasselmann, P. H., Lazzaro, D., & Mothé-Diniz, T., SDSS-based taxonomic classification and orbital distribution of main belt asteroids. 2010, *Astronomy and Astrophysics*, **510**, A43, DOI:10.1051/0004-6361/200913322

Chrenko, O., Brož, M., Nesvorný, D., Tsiganis, K., & Skoulidou, D. K., The origin of long-lived asteroids in the 2:1 mean-motion resonance with Jupiter. 2015, *Monthly Notices of the RAS*, **451**, 2399, DOI:10.1093/mnras/stv1109

Delbo', M., Walsh, K., Bolin, B., Avdellidou, C., & Morbidelli, A., Identification of a primordial asteroid family constrains the original planetesimal population. 2017, *Science*, **357**, 1026, DOI:10.1126/science.aam6036

Durech, J., Sidorin, V., & Kaasalainen, M., DAMIT: a database of asteroid models. 2010, *Astronomy and Astrophysics*, **513**, A46, DOI:10.1051/0004-6361/200912693

Ferrone, S., Delbo, M., Avdellidou, C., et al., Identification of a 4.3 billion year old asteroid family and planetesimal population in the Inner Main Belt. 2023, *Astronomy and Astrophysics*, **676**, A5, DOI:10.1051/0004-6361/202245594

Froeschlé, C., Gonczi, R., & Lega, E., The fast Lyapunov indicator: a simple tool to detect weak chaos. Application to the structure of the main asteroidal belt. 1997a, *Planetary Space Science*, **45**, 881, DOI:10.1016/S0032-0633(97)00058-5

Froeschlé, C., Lega, E., & Gonczi, R., Fast Lyapunov Indicators. Application to Asteroidal Motion. 1997b, *Celestial Mechanics and Dynamical Astronomy*, **67**, 41, DOI:10.1023/A:1008276418601

Gaia Collaboration, Vallenari, A., Brown, A. G. A., et al., Gaia Data Release 3. Summary of the content and survey properties. 2023, *Astronomy and Astrophysics*, **674**, A1, DOI:10.1051/0004-6361/202243940

Ivanova, V. G., Apostolovska, G., Borisov, G. B., & Bilkina, B. I., Results from photometric studies of asteroids at Rozhen National Observatory, Bulgaria. 2002, in ESA Special Publication, Vol. **500**, *Asteroids, Comets, and Meteors: ACM 2002*, ed. B. Warmbein, 505–508

Kaasalainen, M. & Torppa, J., Optimization Methods for Asteroid Lightcurve Inversion. I. Shape Determination. 2001, *Icarus*, **153**, 24, DOI:10.1006/icar.2001.6673

Kaasalainen, M., Torppa, J., & Muinonen, K., Optimization Methods for Asteroid Lightcurve Inversion. II. The Complete Inverse Problem. 2001, *Icarus*, **153**, 37, DOI:10.1006/icar.2001.6674

Klinglesmith, III, D. A. & Hendrickx, S., Asteroid Lightcurve Observations at Etscorn Observatory. 2018, *Minor Planet Bulletin*, **45**, 162

Licchelli, D., Lightcurve analysis of asteroids 300 Geraldina, 573 Recha, 629 Bernardina 721 Tabora, 1547 Nele, and 1600 Vyssotsky. 2006, *Minor Planet Bulletin*, **33**, 50

Mahlke, M., Carry, B., & Mattei, P.-A., Asteroid taxonomy from cluster analysis of spectrometry and albedo. 2022, *Astronomy and Astrophysics*, **665**, A26, DOI:10.1051/0004-6361/202243587

Masiero, J. R., Grav, T., Mainzer, A. K., et al., Main-belt Asteroids with WISE/NEOWISE: Near-infrared Albedos. 2014, *Astrophysical Journal*, **791**, 121, DOI:10.1088/0004-637X/791/2/121

Masiero, J. R., Mainzer, A. K., Grav, T., et al., Preliminary Analysis of WISE/NEOWISE 3-Band Cryogenic and Post-cryogenic Observations of Main Belt Asteroids. 2012, *Astrophysical Journal, Letters*, **759**, L8, DOI:10.1088/2041-8205/759/1/L8

Nesvorný, D., Brož, M., & Carruba, V., Identification and Dynamical Properties of Asteroid Families. 2015, in *Asteroids IV*, ed. P. Michel, F. E. DeMeo, & W. F. Bottke, 297–321

Nesvorný, D., Roig, F., Vokrouhlický, D., & Brož, M., Catalog of Proper Orbits for 1.25 Million Main-belt Asteroids and Discovery of 136 New Collisional Families. 2024, *Astrophysical Journal, Supplement*, **274**, 25, DOI:10.3847/1538-4365/ad675c

Nugent, C. R., Mainzer, A., Bauer, J., et al., NEOWISE Reactivation Mission Year Two: Asteroid Diameters and Albedos. 2016, *Astronomical Journal*, **152**, 63, DOI:10.3847/0004-6256/152/3/63

Polakis, T., Lightcurve Analysis for Eleven Main-belt Asteroids. 2018, *Minor Planet Bulletin*, **45**, 199

Romanishin, W., 300 Geraldina: Possibly a Binary With a Tilted Rotational Axis. 2024, *Minor Planet Bulletin*, **51**, 213

Stephens, R. & Warner, B. D., The ALCDEF Database and the NASA SBN/PDS: The Perfect Merger. 2018, in AAS/Division for Planetary Sciences Meeting Abstracts, Vol. **50**, *AAS/Division for Planetary Sciences Meeting Abstracts #50*, 417.03

Tanga, P., Pauwels, T., Mignard, F., et al., Gaia Data Release 3. The Solar System survey. 2023, *Astronomy and Astrophysics*, **674**, A12, DOI:10.1051/0004-6361/202243796

Todorović, N., The precise and powerful chaos of the 5:2 mean motion resonance with Jupiter. 2017, *Monthly Notices of the RAS*, **465**, 4441, DOI:10.1093/mnras/stw3070

Todorović, N., Apostolovska, G., & Bebekovska, E. V., Lightcurve Photometry of (2525) O'Steen with the new "Milanković" 1.4 m telescope. 2020, in *IAU General Assembly*, 39–39

Vchkova Bebekovska, E., Todorović, N., Kostov, A., Donchev, Z., & Borisov, G., The Physical and Dynamical Characteristics of the Asteroid 4940 Polenov. 2021, *Serbian Astronomical Journal*, **202**, 39, DOI:10.2298/SAJ2102039V

Waszczak, A., Chang, C.-K., Ofek, E. O., et al., Asteroid Light Curves from the Palomar Transient Factory Survey: Rotation Periods and Phase Functions from Sparse Photometry. 2015, *Astronomical Journal*, **150**, 75, DOI:10.1088/0004-6256/150/3/75

Zappala, V., Cellino, A., Barucci, A. M., Fulchignoni, M., & Lupishko, D. F., An analysis of the amplitude-phase relationship among asteroids. 1990, *Astronomy and Astrophysics*, **231**, 548

Contrib. Astron. Obs. Skalnaté Pleso **56/3**, 24 – 34, (2026)
https://doi.org/10.31577/caosp.2026.56.3.24

Rotational characteristics of five photometrically variable stars

P. Rutová[1], M. Skarka[2], J. Žák[2] and P. Gajdoš[3,2]

[1] *Department of Theoretical Physics and Astrophysics, Faculty of Science, Masaryk University, Kotlářská 267/2, 611 37 Brno, Czech Republic (E-mail: 534281@mail.muni.cz)*

[2] *Astronomical Institute of the Czech Academy of Sciences 251 65 Ondřejov, The Czech Republic*

[3] *Institute of Physics, Faculty of Science, Pavol Jozef Šafárik University, 04001 Košice, Slovakia*

Received: February 11, 2026; Accepted: April 22, 2026

Abstract. This study explores photometric variability in a sample of hot stars in order to test whether variability arises from rotational modulation due to surface temperature spots. Frequencies determined from the projected rotational velocities were compared with frequencies estimated on the basis of TESS light curves. In all five cases, the spectroscopic frequency was lower than the photometric one preserving possibility that the observed brightness variations can be rotationally induced. In two of our targets, HT Cet and HD 219487, the photometric frequency spectra suggest more complex variability, likely pulsations. Our results suggest that spot activity inducing rotational modulation may exist in stars hotter than 6500 K, highlighting the value of combined spectroscopic and photometric analysis of variations.

Key words: rotational variability; spectra; light curve; TESS

1. Introduction

Photometric variability in hot stars is not yet fully understood, in contrast to solar-like stars where star spots and rotation are well-established causes of quasi-periodic variations (e.g. Reinhold et al., 2013; McQuillan et al., 2014; Santos et al., 2021). In hotter stars, variability may result from surface inhomogeneities and rotation, effects in close binaries, and pulsations (e.g. Skarka et al., 2022; Skarka & Henzl, 2024). Surface inhomogeneities can arise from two different mechanisms. In chemically peculiar stars, abundance spots produced by diffusion in strong magnetic fields can result in highly stable light curves with typically low photometric amplitudes (e.g. Kochukhov, 2017). In contrast, temperature spots associated with magnetic activity, similar to starspots on the Sun, can produce rotational modulation and evolve on observable timescales (e.g. Berdyugina, 2005). In this work, we consider the possibility that temperature spots produce rotational modulation. However, the relative roles of these factors are unclear. The objective of our study is to determine whether rotational modulation can offer an explanation for the observed photometric variability in a sample of stars hotter than 6500 K, where this kind of stellar variability is not expected but also not ruled out (Cantiello & Braithwaite, 2019; Balona, 2022; Kraft, 1967). This goal is achieved by measuring projected rotational velocities ($v \sin i$) estimated from spectra and comparing them with frequencies estimated from the data series gathered by the *Transiting Exoplanet Survey Satellite* (*TESS,* Ricker et al., 2015).

2. Observations

Candidate stars were selected from the TESS input Catalogue (TIC v8.2, Paegert et al., 2021), based on light curves that exhibit signs of potential rotational variability identified by Skarka et al. (2022). The selection criteria included apparent brightness (Johnson V magnitude ≤ 9), good visibility from the Ondřejov Observatory (Czech Republic), and effective temperatures above 6500 K. We selected five targets for this purpose: HD 197039, HD 204485, HD 219487, 5 Peg, and HT Cet (see Table 1 with the basic parameters from the TIC catalogue).

Table 1. Basic parameters of the sample stars from TIC. Values of $v_{\rm mic}$ and $v_{\rm mac}$ were calculated from empirical relations (see the text for further information).

Star ID	$T_{\rm eff}$ (K)	$\log g$	R ($R_\odot$)	$v_{\rm mic}$ (km/s)	$v_{\rm mac}$ (km/s)
HD 197039	6533	3.91	2.146	1.48	9.50
HD 204485	7186	4.13	1.801	1.88	5.50
HD 219487	6869	4.33	1.308	1.63	12.99
5 Peg	7112	3.37	4.306	2.77	3.85
HT Cet	6929	4.00	2.020	1.70	14.06

We obtained high-resolution spectroscopic data using the Ondřejov Echelle Spectrograph (OES, resolving power $R = \Delta\lambda/\lambda = 50000$ at Hα, Koubský et al., 2004; Kabáth et al., 2020). In 2024-2025, we obtained one spectrum for each target reaching signal-to-noise ratio between 70 and 120 (measured at 660 nm). The SNR of each spectrum is shown in Fig. 2. All the steps of data reduction and processing including bias-subtraction, flat field correction, wavelength calibration and normalization were done using the Image Reduction and Analysis Facility (IRAF, Tody, 1986). For 5 Peg, the OES spectra were of insufficient quality; therefore, high-quality data were retrieved from the public Melchiors archive (Royer et al., 2024), based on observations with the HERMES spectrograph on the Mercator telescope (Raskin & Van Winckel, 2014).

Photometric data were obtained from the TESS mission through the Science Processing Operations Center (SPOC, Jenkins et al., 2016; Caldwell et al., 2020). We used Pre-search Data Conditioning Simple Aperture Photometry

Table 2. Determined parameters from the analysis. Spectroscopic ($f_{\rm sp}$) and photometric ($f_{\rm ph}$) frequencies in the first two columns are in cycles per day, velocities in km/s. Column $(v \sin i)_{\rm lit}$ and 'Ref' give the literature values and the corresponding references, respectively. Inclination angles (i (deg)) were derived in this work from a comparison of spectroscopic and photometric frequencies (see Section 4).The errors are in the parentheses.

Star ID	$f_{\rm sp}$	$f_{\rm ph}$	$v \sin i$	$(v \sin i)_{\rm lit}$	i (deg)	Ref
HD 197039	0.25(3)	0.236(4)	27(3)	26	90(-)	1
HD 204485	0.10(2)	0.146(4)	9(2)	9.3	43(12)	2
HD 219487	0.40(6)	0.581(4)	28(4)	22-35	44(8)	1
5 Peg	0.73(4)	0.828(4)	159(5)	155, 170	62(6)	3,4
HT Cet	0.28(5)	0.912(4)	29(5)	28	18(3)	1

References: 1 – Głębocki & Gnaciński (2005), 2 – Luck (2017), 3 – Abt & Morrell (1995), 4 – Royer et al. (2002)

(PDCSAP) light curves with a 2-minute cadence. We downloaded four available sectors per star, providing sufficient temporal coverage for our analysis, by using LIGHTKURVE package (Lightkurve Collaboration et al., 2018). The lightcurves from a single sectors are shown in Fig. 1.

3. Analysis

3.1. Spectra

Spectral analysis was conducted via the ISPEC framework (Blanco-Cuaresma et al., 2014). The process began with the re-normalisation of the spectra because IRAF normalisation was usually not of sufficient quality, and then cosmic ray artefacts were removed. Each spectrum was then corrected for radial velocity shifts by cross-correlating it with a synthetic mask based on atomic line data from the Vienna Atomic Line Database (VALD, Kupka et al., 1999).

The wavelength range used for the cross-correlation analysis excluded regions contaminated by telluric lines. Balmer lines were not included in the fitting process due to their strong pressure broadening. Instead, we fitted as many Fe and metal lines as possible.

The initial atmospheric parameters — effective temperature ($T_{\rm eff}$ and surface gravity ($\log g$) — were adopted from the TESS Input Catalogue (TIC), accessed via the VizieR server (Ochsenbein et al., 2000). The microturbulent ($v_{\rm mic}$) and macroturbulent velocities ($v_{\rm mac}$) were estimated using the empirical relations given in Doyle et al. (2014), Blanco-Cuaresma (2019) and Worley et al. (2024). The instrumental resolution was set to $R = 50000$ for the OES spectra and $R = 85000$ for the Hermes spectra (Kabáth et al., 2020; Raskin et al., 2011).

The model atmospheres were based on ATLAS9 (Castelli & Kurucz, 2003), optimised for hotter stars. Spectral synthesis was performed using the MOOG (Sneden et al., 2012) code, with solar abundances taken from Grevesse et al. (2007). The adopted line list spanned 300–1100 nm and was sourced from VALD. The alpha-enhancement and limb-darkening parameters were kept at their default values ($\alpha = 0.0$, linear limb-darkening coefficient = 0.6). The parameters used are given in Tables 1 and 2.

During fitting, the metallicity ([Fe/H]) and projected rotational velocity ($v \sin i$) were treated as free parameters. However, for HD 197039, HD 204485 and HD 219487, allowing [Fe/H] to vary resulted in increased uncertainty in $v \sin i$ without improving the fit. In these cases, we assumed the metallicity to be zero and fixed it. For 5 Peg we got [Fe/H]= −0.44(2) and HT Cet -0.2(2). Each fit was iterated six times to ensure the convergence and stability of the

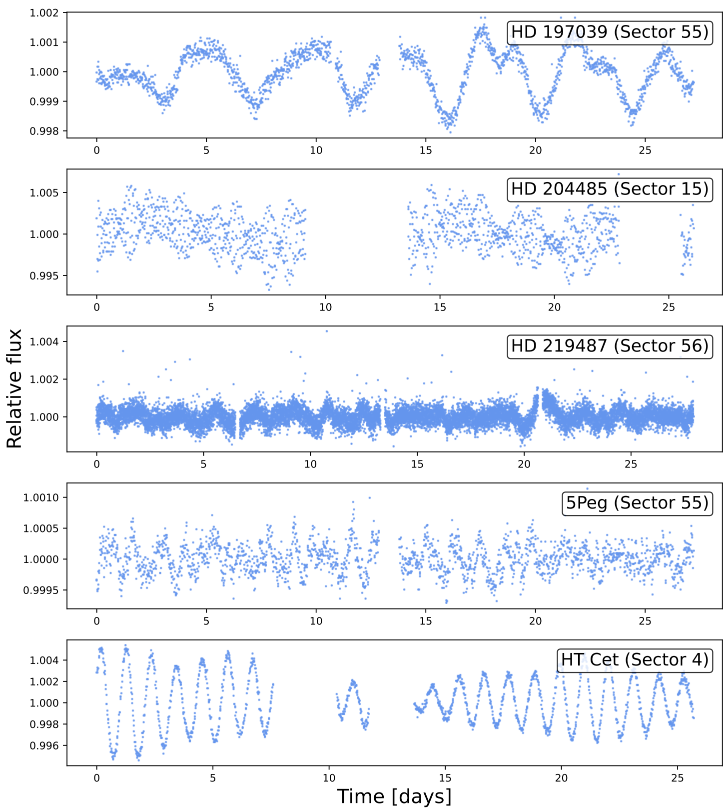

Figure 1. Light curves of selected objects from single sectors showing the basic features of the light variations. Note the different vertical scales.

solution. The final fits are shown in Fig. 2. The fits are reasonably good for most of the stars, with differences given mainly by the normalisation. In case of 5 Peg, the fit is the worst but still reasonably good for the estimation of $v \sin i$.

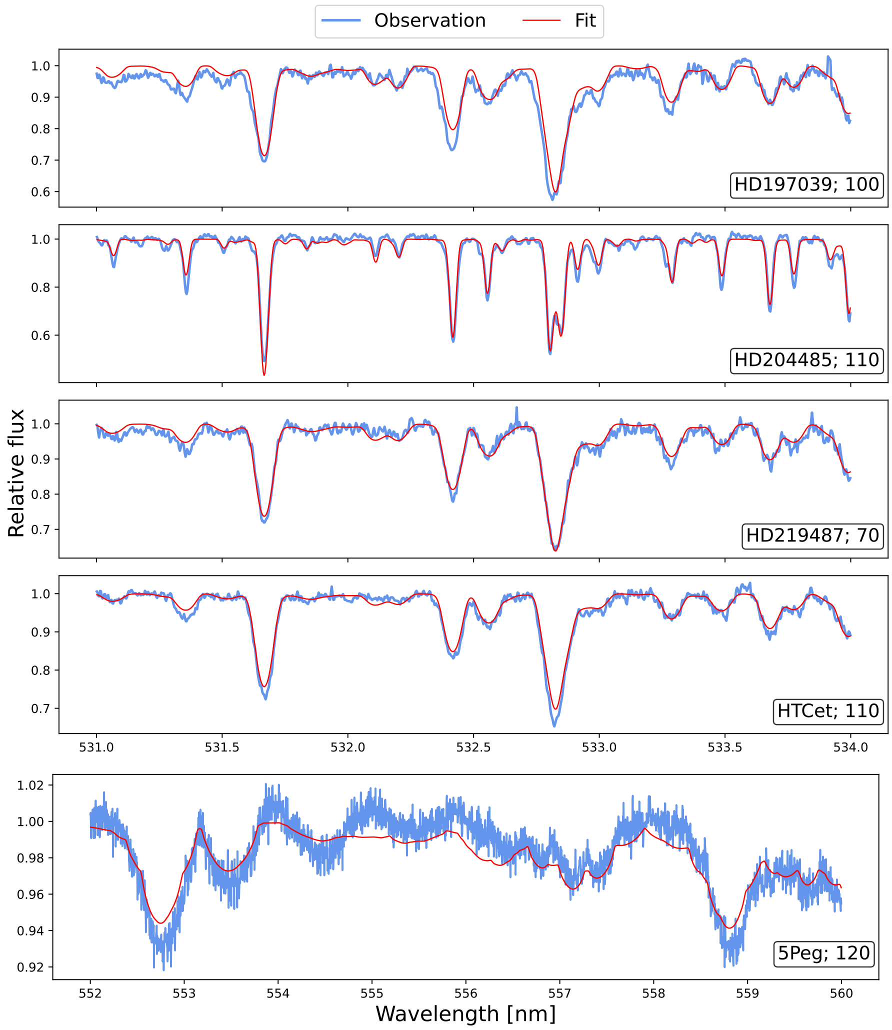

Figure 2. The final fits of the spectra. Each panel is labeled with the star ID and its signal-to-noise ratio.

The values of $v \sin i$ that we determined are in perfect agreement with the literature values (see Table 2) showing a good reliability of our results.

3.2. Photometry

We processed photometric time series data using the LIGHTKURVE Python package (Lightkurve Collaboration et al., 2018) and computed Lomb–Scargle periodograms (Lomb, 1976; Scargle, 1982) to identify the frequencies at which variability was most pronounced. We plotted the amplitude in relative flux units (Fig. 3).

Using the projected rotational velocities obtained from our spectroscopic analysis (Table 1) and the stellar radii from the TIC catalogue, we calculated the expected minimal rotational frequencies as

$$f_{\rm sp} = \frac{v \sin i}{2\pi R} \tag{1}$$

The values $f_{\rm sp}$ represent the lower limits of the rotational frequency because $v \sin i$ gives the bottom boundary of the real rotational velocity. By comparing the photometric and spectroscopic frequencies, we assessed whether the observed variability is consistent with rotational modulation or whether alternative mechanisms are more likely. The comparison of spectroscopic and photometric variability frequencies is shown in Fig. 3.

4. Discussion and conclusions

This study examined whether the photometric variability observed in a sample of hot stars could be attributed to rotational modulation caused by surface spots. The projected rotational velocities derived from spectroscopy ($f_{\rm sp}$) were compared with the photometric frequencies ($f_{\rm ph}$) obtained from TESS data (see Table 2). In HD 197039, HD 204485 and 5 Peg, $f_{\rm sp}$ and $f_{\rm ph}$ are close to each other (see Fig. 3). In addition, the frequency spectra of these three stars show well-defined peaks and, in the case of HD 197039, HD 204485, there are harmonics of the peaks suggesting rotational nature of the photometric variations due to surface inhomogeneities.

In contrast, HT Cet — and possibly HD 219487 — exhibit complex frequency spectra indicative of γ Doradus type pulsations (Balona et al., 1994; Kaye et al., 1999). However, we cannot rule out the possibility that some of the peaks originate from rotation. Assuming that the highest peaks in the frequency spectra reflect the real rotation frequencies, we can easily estimate the inclination of the rotation axes of the stars from the comparison of photometric and spectroscopic frequencies. The inclinations are shown in the last column of Table 1. From the proximity of $f_{\rm sp}$ and $f_{\rm ph}$ (see Table 2 and Fig. 3) it is obvious that, under assumption of rotation, the inclinations of HD 197039 and HD 204485 are close to 90 degrees.

Although this method does not provide definitive proof of the rotational nature of the brightness variability, it can be used as a rough indicator. Our findings suggest that spot activity may extend to stars with effective temperatures in

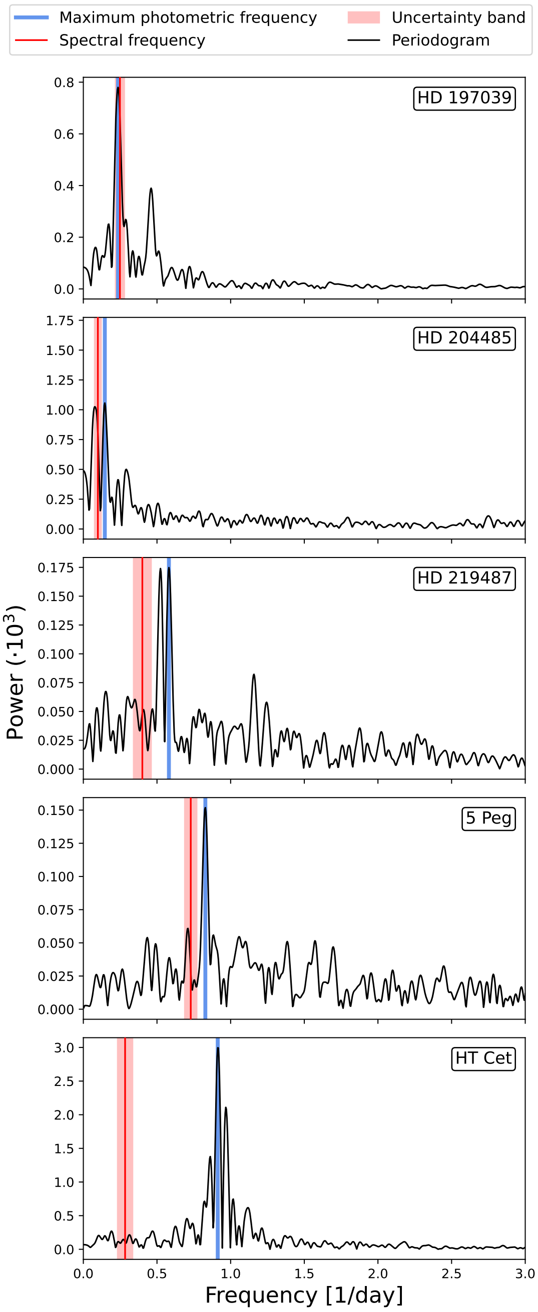

Figure 3. Periodogram with the assumed spectroscopic rotational frequency f_{sp} (red) and the brightness change frequency f_{ph} (blue).

the range 6500–7200 K, which is consistent with recent evidence of complex local magnetic fields generated in the (sub)surface layers of stars (Henriksen et al., 2023; Antoci et al., 2025).

One of the sample stars, HD 204485, was identified as a metallic chemically peculiar star by Maitzen et al. (1998). Stars of this type (usually marked as CP1 or Am-Fm stars) show an underabundance of Ca and Sc and an overabundance of Fe-group and rare-earth elements (Preston, 1974; Michaud et al., 1983). Am-Fm stars are usually slowly rotating stars (Abt & Morrell, 1995), which is the case of HD 204485. In addition, this star appeared to be a δ Sct type pulsator (Breger, 2000) with the dominant frequency at 15.716 c/d (see Fig. 1). Pulsating stars of this type are quite common among Am-Fm stars (Dürfeldt-Pedros et al., 2024). On the other hand, 5 Peg should show δ Sct pulsation (Perry et al., 1987) but we did not detect any significant peak above 5 c/d characteristic for this type of pulsations (Uytterhoeven et al., 2011). The remaining stars in our sample also do not show any additional variability.

Our results highlight the importance of combining photometric and spectroscopic data to identify spot candidates among hot stars. Further confirmation of the rotation and revelation of the nature of the spots would benefit from long-term spectroscopic monitoring enabling line-profile variation studies, Doppler imaging, and detailed chemical abundance analysis.

Acknowledgements. MS acknowledges financial support of the Inter-transfer grant no LTT-20015. We acknowledge the usage of the data taken with the Perek telescope at the Astronomical Institute of CAS. The research of P.G. was supported by the Slovak Research and Development Agency under contract No. APVV-24-0160, and by internal grant No. VVGS-2023-2784 of the P. J. Šafárik University in Košice and funded by the EU NextGenerationEU through the Recovery and Resilience Plan for Slovakia under project No. 09I03-03-V05-00008. The results are based on a bachelor project at the Masaryk university in Brno, Czech Republic.

References

Abt, H. A. & Morrell, N. I., The Relation between Rotational Velocities and Spectral Peculiarities among A-Type Stars. 1995, *Astrophysical Journal, Supplement*, **99**, 135, DOI:10.1086/192182

Antoci, V., Cantiello, M., Khalack, V., et al., Magnetic fields or overstable convective modes in HR 7495: Exploring the underlying causes of the spike in the 'hump and spike' features. 2025, *Astronomy and Astrophysics*, **696**, A111, DOI:10.1051/0004-6361/202450640

Balona, L. A., Rotation of hot normal, peculiar and Be stars from space photometry. 2022, *Monthly Notices of the RAS*, **516**, 3641, DOI:10.1093/mnras/stac2515

Balona, L. A., Krisciunas, K., & Cousins, A. W. J., Gamma Doradus : evidence for a new class of pulsating star. 1994, *Monthly Notices of the RAS*, **270**, 905, DOI:10.1093/mnras/270.4.905

Berdyugina, S. V., Starspots: A Key to the Stellar Dynamo. 2005, *Living Reviews in Solar Physics*, **2**, 8, DOI:10.12942/lrsp-2005-8

Blanco-Cuaresma, S., Modern stellar spectroscopy caveats. 2019, *Monthly Notices of the RAS*, **486**, 2075, DOI:10.1093/mnras/stz549

Blanco-Cuaresma, S., Soubiran, C., Heiter, U., & Jofré, P., Determining stellar atmospheric parameters and chemical abundances of FGK stars with iSpec. 2014, *Astronomy and Astrophysics*, **569**, A111, DOI:10.1051/0004-6361/201423945

Breger, M., δ Scuti stars (Review). 2000, in Astronomical Society of the Pacific Conference Series, Vol. **210**, *Delta Scuti and Related Stars*, ed. M. Breger & M. Montgomery, 3

Caldwell, D. A., Tenenbaum, P., Twicken, J. D., et al., TESS Science Processing Operations Center FFI Target List Products. 2020, *Research Notes of the American Astronomical Society*, **4**, 201, DOI:10.3847/2515-5172/abc9b3

Cantiello, M. & Braithwaite, J., Envelope Convection, Surface Magnetism, and Spots in A and Late B-type Stars. 2019, *Astrophysical Journal*, **883**, 106, DOI:10.3847/1538-4357/ab3924

Castelli, F. & Kurucz, R. L., New Grids of ATLAS9 Model Atmospheres. 2003, in IAU Symposium, Vol. **210**, *Modelling of Stellar Atmospheres*, ed. N. Piskunov, W. W. Weiss, & D. F. Gray, A20

Doyle, A. P., Davies, G. R., Smalley, B., Chaplin, W. J., & Elsworth, Y., Determining stellar macroturbulence using asteroseismic rotational velocities from Kepler. 2014, *Monthly Notices of the RAS*, **444**, 3592, DOI:10.1093/mnras/stu1692

Dürfeldt-Pedros, O., Antoci, V., Smalley, B., et al., Variability and stellar pulsation incidence in Am and Fm stars using TESS and Gaia data. 2024, *Astronomy and Astrophysics*, **690**, A104, DOI:10.1051/0004-6361/202349076

Głębocki, R. & Gnaciński, P., Systematic errors in the determination of stellar rotational velocities. 2005, in ESA Special Publication, Vol. **560**, *13th Cambridge Workshop on Cool Stars, Stellar Systems and the Sun*, ed. F. Favata, G. A. J. Hussain, & B. Battrick, 571

Grevesse, N., Asplund, M., & Sauval, A. J., The Solar Chemical Composition. 2007, *Space Science Reviews*, **130**, 105, DOI:10.1007/s11214-007-9173-7

Henriksen, A. I., Antoci, V., Saio, H., et al., Rotational modulation in A and F stars: magnetic stellar spots or convective core rotation? 2023, *Monthly Notices of the RAS*, **520**, 216, DOI:10.1093/mnras/stad153

Jenkins, J. M., Twicken, J. D., McCauliff, S., et al., The TESS science processing operations center. 2016, in Society of Photo-Optical Instrumentation Engineers (SPIE) Conference Series, Vol. **9913**, *Software and Cyberinfrastructure for Astronomy IV*, ed. G. Chiozzi & J. C. Guzman, 99133E

Kabáth, P., Skarka, M., Sabotta, S., et al., Ondřejov Echelle Spectrograph, Ground Based Support Facility for Exoplanet Missions. 2020, *Publications of the ASP*, **132**, 035002, DOI:10.1088/1538-3873/ab6752

Kaye, A. B., Handler, G., Krisciunas, K., Poretti, E., & Zerbi, F. M., Gamma Doradus Stars: Defining a New Class of Pulsating Variables. 1999, *Publications of the ASP*, **111**, 840, DOI:10.1086/316399

Kochukhov, O., Doppler imaging of chemical spots on magnetic Ap/Bp stars. Numerical tests and assessment of systematic errors. 2017, *Astronomy and Astrophysics*, **597**, A58, DOI:10.1051/0004-6361/201629768

Koubský, P., Mayer, P., Čáp, J., et al., Ondřejov Echelle Spectrograph - OES. 2004, *Publications of the Astronomical Institute of the Czechoslovak Academy of Sciences*, **92**, 37

Kraft, R. P., Studies of Stellar Rotation. V. The Dependence of Rotation on Age among Solar-Type Stars. 1967, *Astrophysical Journal*, **150**, 551, DOI:10.1086/149359

Kupka, F., Piskunov, N., Ryabchikova, T. A., Stempels, H. C., & Weiss, W. W., VALD-2: Progress of the Vienna Atomic Line Data Base. 1999, *Astronomy and Astrophysics, Supplement*, **138**, 119, DOI:10.1051/aas:1999267

Lightkurve Collaboration, Cardoso, J. V. d. M., Hedges, C., et al. 2018, Lightkurve: Kepler and TESS time series analysis in Python, Astrophysics Source Code Library, record ascl:1812.013

Lomb, N. R., Least-Squares Frequency Analysis of Unequally Spaced Data. 1976, *Astrophysics and Space Science*, **39**, 447, DOI:10.1007/BF00648343

Luck, R. E., Abundances in the Local Region II: F, G, and K Dwarfs and Subgiants. 2017, *Astronomical Journal*, **153**, 21, DOI:10.3847/1538-3881/153/1/21

Maitzen, H. M., Pressberger, R., & Paunzen, E., Delta a and Stroemgren photometry of stars in the Renson-catalogue of AP and AM stars. 1998, *Astronomy and Astrophysics, Supplement*, **128**, 573, DOI:10.1051/aas:1998164

McQuillan, A., Mazeh, T., & Aigrain, S., Rotation Periods of 34,030 Kepler Main-sequence Stars: The Full Autocorrelation Sample. 2014, *Astrophysical Journal, Supplement*, **211**, 24, DOI:10.1088/0067-0049/211/2/24

Michaud, G., Tarasick, D., Charland, Y., & Pelletier, C., Diffusion, meridional circulation, and mass loss in Fm-Am stars. 1983, *Astrophysical Journal*, **269**, 239, DOI:10.1086/161034

Ochsenbein, F., Bauer, P., & Marcout, J., The VizieR database of astronomical catalogues. 2000, *Astronomy and Astrophysics, Supplement*, **143**, 23, DOI:10.1051/aas:2000169

Paegert, M., Stassun, K. G., Collins, K. A., et al., TESS Input Catalog versions 8.1 and 8.2: Phantoms in the 8.0 Catalog and How to Handle Them. 2021, *arXiv* [eprint: 2108.04778], DOI:10.48550/arXiv.2108.04778

Perry, C. L., Olsen, E. H., & Crawford, D. L., A catalog of bright UVBY beta standard stars. 1987, *Publications of the ASP*, **99**, 1184, DOI:10.1086/132103

Preston, G. W., The chemically peculiar stars of the upper main sequence. 1974, *Annual Review of Astron and Astrophys*, **12**, 257, DOI:10.1146/annurev.aa.12.090174.001353

Raskin , G. & Van Winckel, H., HERMES at Mercator, competitive high-resolution spectroscopy with a small telescope. 2014, *Astronomische Nachrichten*, **335**, 32, DOI:10.1002/asna.201312009

Raskin, G., van Winckel, H., Hensberge, H., et al., HERMES: a high-resolution fibre-fed spectrograph for the Mercator telescope. 2011, *Astronomy and Astrophysics*, **526**, A69, DOI:10.1051/0004-6361/201015435

Reinhold, T., Reiners, A., & Basri, G., Rotation and differential rotation of active Kepler stars. 2013, *Astronomy and Astrophysics*, **560**, A4, DOI:10.1051/0004-6361/201321970

Ricker, G. R., Winn, J. N., Vanderspek, R., et al., Transiting Exoplanet Survey Satellite (TESS). 2015, *Journal of Astronomical Telescopes, Instruments, and Systems*, **1**, 014003, DOI:10.1117/1.JATIS.1.1.014003

Royer, F., Grenier, S., Baylac, M.-O., Gómez, A. E., & Zorec, J., Rotational velocities of A-type stars in the northern hemisphere. II. Measurement of v sin i. 2002, *Astronomy and Astrophysics*, **393**, 897, DOI:10.1051/0004-6361:20020943

Royer, P., Merle, T., Dsilva, K., et al., MELCHIORS. The Mercator Library of High Resolution Stellar Spectroscopy. 2024, *Astronomy and Astrophysics*, **681**, A107, DOI:10.1051/0004-6361/202346847

Santos, A. R. G., Breton, S. N., Mathur, S., & García, R. A., Surface Rotation and Photometric Activity for Kepler Targets. II. G and F Main-sequence Stars and Cool Subgiant Stars. 2021, *Astrophysical Journal, Supplement*, **255**, 17, DOI:10.3847/1538-4365/ac033f

Scargle, J. D., Studies in astronomical time series analysis. II. Statistical aspects of spectral analysis of unevenly spaced data. 1982, *Astrophysical Journal*, **263**, 835, DOI:10.1086/160554

Skarka, M. & Henzl, Z., Periodic variable A-F spectral type stars in the southern TESS continuous viewing zone. I. Identification and classification. 2024, *Astronomy and Astrophysics*, **688**, A25, DOI:10.1051/0004-6361/202450711

Skarka, M., Žák, J., Fedurco, M., et al., Periodic variable A-F spectral type stars in the northern TESS continuous viewing zone. I. Identification and classification. 2022, *Astronomy and Astrophysics*, **666**, A142, DOI:10.1051/0004-6361/202244037

Sneden, C., Bean, J., Ivans, I., Lucatello, S., & Sobeck, J. 2012, MOOG: LTE line analysis and spectrum synthesis, Astrophysics Source Code Library, record ascl:1202.009

Tody, D., The IRAF Data Reduction and Analysis System. 1986, in Society of Photo-Optical Instrumentation Engineers (SPIE) Conference Series, Vol. **627**, *Instrumentation in astronomy VI*, ed. D. L. Crawford, 733

Uytterhoeven, K., Moya, A., Grigahcène, A., et al., The Kepler characterization of the variability among A- and F-type stars. I. General overview. 2011, *Astronomy and Astrophysics*, **534**, A125, DOI:10.1051/0004-6361/201117368

Worley, C. C., Smiljanic, R., Magrini, L., et al., The Gaia-ESO Survey: The DR5 analysis of the medium-resolution GIRAFFE and high-resolution UVES spectra of FGK-type stars. 2024, *Astronomy and Astrophysics*, **684**, A148, DOI:10.1051/0004-6361/202347558

Contrib. Astron. Obs. Skalnaté Pleso **56/3**, 35 – 53, (2026)
https://doi.org/10.31577/caosp.2026.56.3.35

A Gaia DR3–LAMOST reassessment of high-velocity star candidates with geometric-distance-aware kinematics

F. Li[1], G. Huang[2] and L. Yang[3]

[1] *School of Artificial Intelligence, Nanjing Vocational College of Information Technology, Nanjing, China (E-mail: liff@njcit.cn) (corresponding author)*

[2] *College of Information Engineering, Northwest A&F University, Yangling, China (E-mail: harry.huang@nwafu.edu.cn)*

[3] *College of Applied Technology, Nanjing University of Information Science and Technology, Nanjing, China (E-mail: 190302282228@csit.edu.cn)*

Received: May 1, 2026; Accepted: May 20, 2026

Abstract. We revisit three published high-velocity-star catalogues drawn from Gaia and LAMOST – Li et al. (2021, 591 stars), Li et al. (2023, 88 stars) and Liao et al. (2024, 519 stars) – and quantify how the published unbound classification of these candidates changes with the choice of distance estimator and with the choice of radial-velocity catalogue. After Gaia DR3 source_id resolution and de-duplication our master sample contains 1101 unique stars. 675 of them satisfy ruwe < 1.4, $\varpi/\sigma_\varpi > 5$ and carry a Gaia DR3 radial velocity (the Gaia-only clean sample). 356 additionally pass a 1 arcsec LAMOST DR9 LRS cross-match, atmospheric-parameter cuts and a $50\,\mathrm{km\,s^{-1}}$ Gaia–LAMOST RV agreement test (the final-strict sample). For every star in this strict subset, the three-dimensional Galactocentric rest-frame speed v_grf and the local escape speed v_esc are computed with a 1000-draw Monte Carlo under the MWPotential2014 potential of Bovy (2015), once with inverse-parallax distances ($1000/\varpi$) and once with the geometric distances of Bailer-Jones et al. (2021). Switching from inverse parallax to Bailer-Jones distances on the same 356 stars reduces the count with $P_\mathrm{unbound} = P(v_\mathrm{grf} > v_\mathrm{esc}) > 0.5$ from **48 to 3**, and the count with $P_\mathrm{unbound} > 0.9$ from **12 to 1**; 45 stars are downgraded across the $P_\mathrm{unbound} = 0.5$ threshold and none are gained. Substituting LAMOST radial velocities for Gaia radial velocities on the same subset changes the median v_grf by $0.00\,\mathrm{km\,s^{-1}}$ ($p_{90}|\Delta v_\mathrm{grf}| = 5.7\,\mathrm{km\,s^{-1}}$) and flips the $P_\mathrm{unbound} = 0.5$ classification of one star out of 356. The unbound classification of these published candidates is therefore set by the distance estimator, not by the choice of radial-velocity catalogue. The final-strict sample, a Top-15 main candidate table, and a Top-30 machine-readable supplementary CSV are released with this paper; the three highest-confidence candidates are metal-poor giants that warrant targeted spectroscopic follow-up.

[1]F. Li and G. Huang contributed equally to this work. Correspondence and material requests should be addressed to F. Li ((E-mail: liff@njcit.cn)).

Key words: high-velocity stars – Galaxy: kinematics and dynamics – stars: distances – catalogues – methods: data analysis

1. Introduction

High-velocity stars (HVS) trace the most extreme end of Galactic stellar kinematics. The classical picture of Hills (1988) predicts that tidal disruption of close binaries by the central massive black hole ejects stars at speeds well above the local Galactic escape speed; this mechanism was placed on a firm theoretical footing by Yu & Tremaine (2003) and observationally established by Brown et al. (2005), who reported the first unbound HVS in the Milky Way halo. The subsequent decade-and-a-half of dedicated surveys (Brown et al., 2007; Kenyon et al., 2008; Brown et al., 2014, and references therein) consolidated HVSs as a distinct dynamical class, reviewed comprehensively by Brown (2015).

The advent of Gaia astrometry transformed the HVS landscape. Both Boubert et al. (2018) and Marchetti et al. (2019) revisited literature HVS catalogues using Gaia DR2 phase-space information and showed that the published unbound classification of many candidates depended sensitively on the assumed distance scale and on the propagation of parallax uncertainties. The combination of Gaia DR3 with LAMOST DR9 (Cui et al., 2012; Yan et al., 2022) now provides 6D phase-space coverage with self-consistent atmospheric parameters for a substantial fraction of bright candidates, and three recent VizieR-published catalogues (Li et al., 2021, 2023; Liao et al., 2024) compile a combined 1198 candidate rows that are the natural starting point for any contemporary reassessment.

The interpretation of these candidates as bound or unbound, however, hinges on the choice of distance estimator. Inverse parallax, $1/\varpi$, is biased toward larger distances and increased random errors precisely in the high-velocity regime where parallax signal-to-noise is small (Bailer-Jones, 2015; Luri et al., 2018; Lindegren et al., 2021). The geometric-distance catalogue of Bailer-Jones et al. (2021), which folds in a Galactic prior, returns systematically smaller distances for parallax-uncertain stars and is now the standard product for kinematic work.

In this paper the unbound classification of the three published catalogues is re-derived under both distance estimators, with uncertainties propagated through a 1000-draw Monte Carlo sampler, and the robustness of the conclusion is tested against the choice of radial-velocity catalogue (Gaia DR3 vs. LAMOST DR9). The comparison is carried out on the final-strict sample of 356 stars defined in Section 2.4, so that the inverse-parallax and Bailer-Jones passes share identical proper motions, radial velocities, LAMOST-quality cuts and Monte Carlo error budgets. Any change in the unbound count then reflects the distance estimator alone. For this fixed subset, $P_{\rm unbound} > 0.5$ falls from 48 to 3 and $P_{\rm unbound} > 0.9$ falls from 12 to 1 between the two distance choices. The radial-velocity catalogue has almost no effect: the median $v_{\rm grf}$ shifts by $0\,{\rm km\,s^{-1}}$ ($p_{90}|\Delta v_{\rm grf}| = 5.7\,{\rm km\,s^{-1}}$).

The unbound classification of the published candidates is therefore set by the distance estimator.

The present work is complementary to the recent CAOSP study by Elsanhoury (2025), which used a similar combination of Gaia DR3 and LAMOST DR9 high-velocity-star catalogues to derive Galactic kinematic parameters: velocity ellipsoids, the solar motion and the Oort constants. The questions are different. The U, V, W statistics and the Oort constants are not recomputed here, and no new candidate sample is reported. Instead, the three published catalogues, the cross-match and the quality cuts are kept fixed, and the analysis isolates a single methodological choice: the distance estimator that enters the unbound probability. Elsanhoury (2025) characterises the kinematic distribution of high-velocity stars; the present analysis characterises the sensitivity of their unbound classification to the distance prescription.

The paper is organised as follows. Section 2 describes the sample construction. Section 3 details the kinematic methods, Bailer-Jones distance upgrade, and the Monte Carlo error propagation. Section 4 presents the results, anchored on seven figures and three tables. Section 5 discusses the distance-driven downgrade, the physical context of the surviving Top-3 candidates, and the limitations of the analysis. Section 6 concludes.

2. Data and sample construction

2.1. Source catalogues

Three published high-velocity-star candidate catalogues serve as input. All of them are available through VizieR (Ochsenbein et al., 2000) and downloaded with ASTROQUERY (Ginsburg et al., 2019):

- **li2021**: `J/ApJS/252/3/hivelscs`, the Li et al. (2021) catalogue of 591 high-velocity-star candidates selected from LAMOST DR7 and Gaia DR2.
- **li2023**: `J/AJ/166/12/table5`, the 88-row Table A1 of Li et al. (2023); we deliberately use the full Table A1 rather than the 52-row escape-velocity-filtered subset (`table2`) as our parent sample.
- **liao2024**: `J/AJ/167/76/table6`, the 519-star catalogue of Liao et al. (2024) that incorporates the gravitational impact of the Large Magellanic Cloud.

The combined raw input is 1198 catalogue rows.

2.2. Gaia DR3 enrichment

For every catalogue source we resolve the Gaia DR3 source_id via VizieR and run an asynchronous TAP upload-join against `gaiadr3.gaia_source` (Gaia Collaboration et al., 2023) to retrieve `parallax`, `parallax_error`, $\mu_{\alpha*}$, μ_δ and their errors, the Gaia radial velocity `radial_velocity` with its error, `phot_g_mean_mag`, phot_bp_mean_mag, phot_rp_mean_mag, and ruwe. Ten of the 591 li2021 source_ids do not resolve in DR3 (merged or removed between EDR3 and DR3). Combined across the three catalogues, we obtain 1188 successful Gaia DR3 matches; deduplication across catalogues yields 1101 unique source_ids that constitute the master sample.

2.3. LAMOST DR9 cross-match

The public LAMOST DR9 LRS stellar parameter catalogue, containing 6 921 466 rows after sentinel-value cleanup, is adopted for the cross-match. Atmospheric parameters and radial velocities are produced by the LSP3 pipeline (Xiang et al., 2015); the survey design and decadal status are described in Zhao et al. (2012); Deng et al. (2012); Yan et al. (2022). Cross-matching the 1101 master sources against this catalogue with `astropy.coordinates.SkyCoord` (Astropy Collaboration et al., 2013, 2018) at 1 arcsec yields 928 Gaia–LAMOST pairs (multi-epoch) and 651 unique Gaia sources matched. For multi-epoch matches we retain the highest-snrg record per Gaia source. The full angular separation distribution has median 0.31 arcsec and 99% percentile 0.91 arcsec, well within the match radius.

2.4. Quality cuts and analysis samples

We define the following Boolean flags (motivated by Lindegren et al., 2021; Luri et al., 2018):

– `q_gaia_astrometry`: ruwe < 1.4 AND $\varpi > 0$ AND $\varpi/\sigma_\varpi > 5$.

– `q_gaia_rv`: Gaia DR3 radial velocity available.

– `q_lamost`: 1 arcsec LAMOST cross-match success.

– `q_lamost_quality`: `q_lamost` AND $T_{\rm eff}$, $\log g$, [Fe/H] all reported AND continuum $S/N \geq 20$.

– `q_rv_consistent`: both Gaia and LAMOST RV reported, $|\Delta v_{\rm RV}| \leq 50\,{\rm km\,s^{-1}}$.

Two analysis populations follow from these flags. The *Gaia-only clean* sample is the conjunction of `q_gaia_astrometry` and `q_gaia_rv` (N=675), used as the kinematic background. The *final strict* sample additionally requires `q_lamost_quality` and `q_rv_consistent` (N=356), and forms the population on which all candidate statistics are based. Two stars exceed the $|\Delta v_{\rm RV}| > 50\,{\rm km\,s^{-1}}$ threshold but otherwise satisfy every gate; they are kept in the master table and exported separately as RV-outlier follow-up candidates rather than included in the final strict subset.

The full sample-construction funnel is shown in Fig. 1 and tabulated in Table 1.

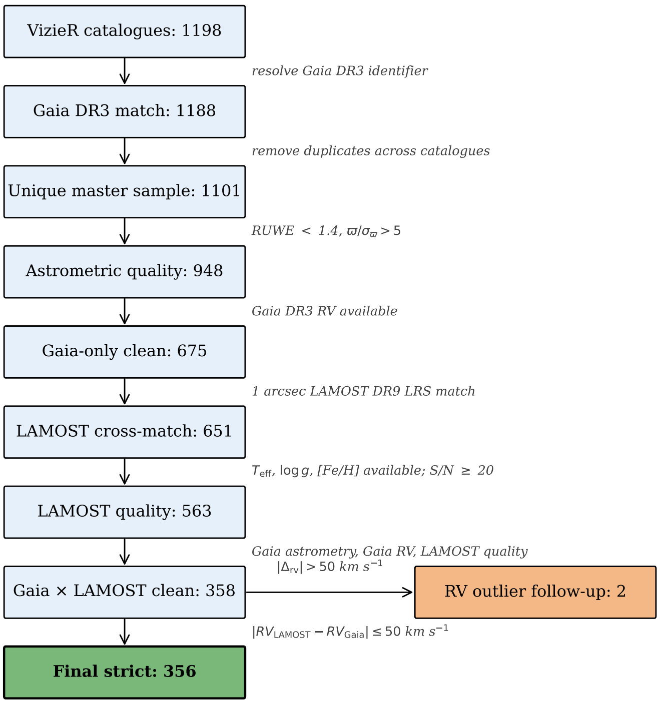

Figure 1. Sample construction. The vertical chain shows the row count after each filter, with the gate criterion annotated to the right of the arrows. The final-strict analysis sample (356 stars; dark green) is the population used for the Top-30 candidate table; the RV-outlier follow-up subset (2 stars; orange side branch) is reported separately and is not part of the final-strict sample.

3. Methods

3.1. Coordinate frame and solar parameters

All kinematic quantities are computed in the Galactocentric frame implemented in `astropy.coordinates` (Astropy Collaboration et al., 2013, 2018). We adopt $R_\odot = 8.122\,\mathrm{kpc}$ (Gravity Collaboration et al., 2018), $z_\odot = 0.0208\,\mathrm{kpc}$ (Bennett & Bovy, 2019), and a solar Galactocentric Cartesian velocity of $(12.9, 245.6, 7.78)\,\mathrm{km\,s^{-1}}$, drawn from Reid & Brunthaler (2020) for the absolute

Table 1. Sample construction and quality cuts.

Stage	N	Definition
VizieR rows	1198	All three high-velocity-star catalogues.
Gaia DR3 hit	1188	VizieR `Gaia` ids that resolve in `gaiadr3.gaia_source`.
Unique Gaia source_id (master)	1101	After de-duplication across catalogues.
`q_gaia_astrometry`	948	RUWE < 1.4 and $\varpi > 0$ and $\varpi/\sigma_\varpi > 5$.
Gaia-only clean	675	`q_gaia_astrometry` and Gaia RV available.
Gaia × LAMOST matched	651	1 arcsec sky cross-match (any quality).
`q_lamost_quality`	563	LAMOST $T_{\rm eff}$, $\log g$, [Fe/H] all reported and SNR ≥ 20.
Gaia × LAMOST clean	358	`q_gaia_astrometry` and Gaia RV and `q_lamost_quality`.
Final strict	356	Above and $\lvert v_{\rm RV,LAMOST} - v_{\rm RV,Gaia}\rvert \leq 50\ {\rm km\,s^{-1}}$.
RV-outlier follow-up	2	Above gates and $\lvert \Delta v_{\rm RV}\rvert > 50\ {\rm km\,s^{-1}}$; reported separately.

component and from Schönrich et al. (2010) for the local peculiar component.

The (U, V, W) components reported in Fig. 4 and the supplementary Top-30 CSV are heliocentric Galactic Cartesian, with U positive toward the Galactic centre, V positive in the direction of Galactic rotation, and W positive toward the North Galactic Pole; they are not LSR-corrected. The Galactocentric speed $v_{\rm grf}$ and the planar local escape speed $v_{\rm esc}(R_{\rm gc})$ are evaluated under MWPotential2014 (Bovy, 2015); alternative potentials of comparable parameter quality (McMillan, 2017; Piffl et al., 2014; Monari et al., 2018) change $v_{\rm esc}(R_\odot)$ at the few-percent level and are folded into the discussion of systematics in Sect. 5.4.

3.2. Distance estimators

Two distance estimators are compared. The *preliminary* distance is the inverse-parallax distance $d_\varpi = 1000/\varpi$ pc, with the well-known biases for parallax-uncertain stars (Bailer-Jones, 2015; Luri et al., 2018). The *primary* distance is the Bailer-Jones geometric distance $r_{\rm med,geo}$ from Bailer-Jones et al. (2021), queried as the `r_med_geo` column of the `external.gaiaedr3_distance` table on the Gaia archive; we also retrieve the 16th and 84th percentiles $r_{\rm lo,geo}$ and $r_{\rm hi,geo}$ for Monte Carlo sampling. All 1101 master sources match the Bailer-Jones catalogue successfully; EDR3↔DR3 source_id compatibility is 100% in our sample. Figure 3 compares the two estimators directly and is discussed in Sect. 4.2.

3.3. Monte Carlo error propagation

For each star we draw $N_{\rm MC} = 1000$ jointly sampled realizations of (ϖ *or* $r_{\rm med,geo}$), $\mu_{\alpha*}$, μ_δ, and the adopted radial velocity. Distances under the inverse-parallax pass are sampled from a normal $\mathcal{N}(\varpi, \sigma_\varpi)$ truncated at $\varpi > 0$. Distances under the BJ pass are sampled log-normally with $\sigma_{\log d} = (\log_{10} r_{\rm hi,geo} - \log_{10} r_{\rm lo,geo})/2$ to handle the typical asymmetry of the BJ percentiles. Proper motions and RV are sampled from independent normals with their reported errors. For each draw we compute (U, V, W), $v_{\rm grf}$, $V_{\rm tot,helio}$, the local escape speed $v_{\rm esc}(R_{\rm gc})$, and the ratio $v_{\rm grf}/v_{\rm esc}$; the unbound probability is the MC fraction with $v_{\rm grf} > v_{\rm esc}$.

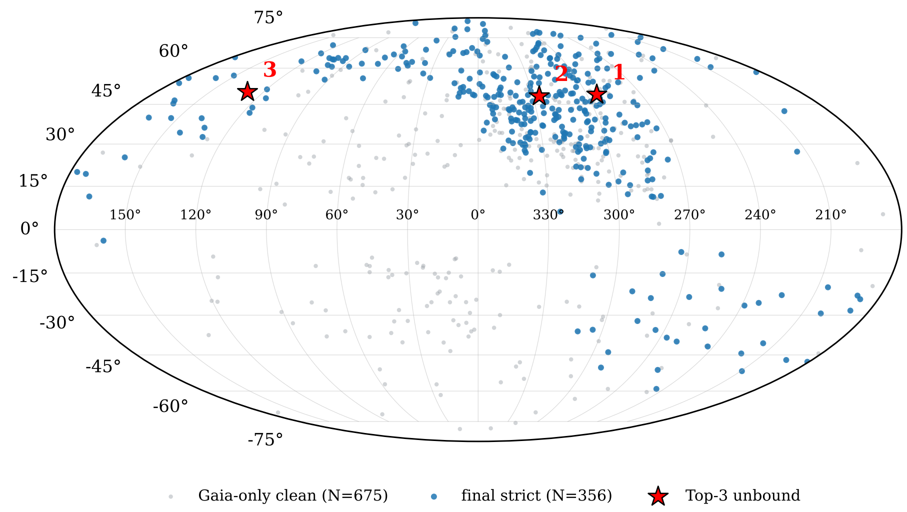

Figure 2. Galactic sky distribution of the Gaia-only clean background (grey), the final-strict sample (blue) and the three highest-confidence unbound candidates (red stars, labelled 1–3). Catalogue provenance is not encoded by colour to keep the figure legible.

3.4. Radial-velocity sensitivity check

On the final-strict sample we re-run the kinematic solution with the LAMOST radial velocity replacing the Gaia DR3 value, keeping every other input identical. We label the two resulting estimates $v_{\rm grf}^{\rm Gaia}$ and $v_{\rm grf}^{\rm LAMOST}$; their per-star difference $\Delta v_{\rm grf} = v_{\rm grf}^{\rm LAMOST} - v_{\rm grf}^{\rm Gaia}$ underpins Sect. 4.5 and Fig. 7.

4. Results

4.1. Sky distribution

Figure 2 shows the Galactic-coordinate distribution of the 675 Gaia-only-clean sources (light grey), the 356 final-strict sources (blue) and the three highest-confidence unbound candidates (red stars). The footprint is dominated by the LAMOST-accessible northern declinations, with a strong concentration above the Galactic plane consistent with halo-tracer kinematics. The 88-star Li et al. (2023) subset is retained in the Gaia-only analysis but contributes no objects to the final-strict sample under our LAMOST cross-match and quality criteria; conclusions involving atmospheric parameters are therefore based primarily on the Li et al. (2021) and Liao et al. (2024) subsets.

Table 2. Distance and kinematic sensitivity summary. All counts are computed on the same 356-star final-strict sample; the two columns differ only in the distance estimator.

Quantity	Inverse parallax	Bailer–Jones
Sample size	356	356
$P_{\mathrm{unbound}} > 0.5$	48	3
$P_{\mathrm{unbound}} > 0.7$	29	1
$P_{\mathrm{unbound}} > 0.9$	12	1
Stars downgraded across $P = 0.5$	—	45
Stars promoted across $P = 0.5$	—	0
Median $r_{\mathrm{med,geo}}/(1000/\varpi)$	—	0.88

4.2. Distance reassessment

Figure 3 compares inverse-parallax and Bailer-Jones distances on the master sample. Bailer-Jones distances are systematically smaller, with median $r_{\mathrm{med,geo}}/(1000/\varpi) = 0.88$ across the master sample and 0.76 on the 50 candidates with the largest preliminary P_{unbound} (red triangles). For tangentially-dominated objects the implied total peculiar speed scales linearly with distance; the 24% distance shrinkage on the Top-50 therefore translates directly into a $\sim$ 24% reduction in v_{grf}, which is enough to push many candidates below the local v_{esc}. Five li2023 stars in the master have $\varpi < 0$; the Bailer-Jones catalogue gives them physically sensible distances of 2–5 kpc.

The main impact on the unbound classification is summarised in Table 2. *All counts in Table 2 are computed on the same final-strict sample of 356 stars; the two passes differ only in the distance estimator.* On this fixed sample, the count of likely-unbound stars ($P_{\mathrm{unbound}} > 0.5$) drops from 48 (inverse parallax) to 3 (Bailer-Jones), and the count of high-confidence unbound stars ($P_{\mathrm{unbound}} > 0.9$) drops from 12 to 1. Of the 48 stars classified as $P_{\mathrm{unbound}} > 0.5$ under inverse parallax, 45 are downgraded across the 0.5 threshold by the Bailer-Jones pass and 3 remain; no star is gained by switching estimators. The reduction is therefore not a side-effect of the LAMOST quality or RV-consistency cuts that define the final-strict sample, but a direct consequence of the choice of distance estimator.

4.3. Final kinematics

Figure 4 presents the Toomre diagram for the Gaia-only-clean (grey), final-strict (blue) and Top-3 (red star) populations under Bailer-Jones distances and Gaia radial velocities. The final-strict sample populates the halo-like region of the diagram, with typical $\sqrt{U^2 + W^2}$ in the range 200–400 km s^{-1}. Figure 5 expresses the same kinematics as the unbound ratio $v_{\mathrm{grf}}/v_{\mathrm{esc}}(R_{\mathrm{gc}})$ versus Bailer-Jones distance: the dashed horizontal line at $v_{\mathrm{grf}} = v_{\mathrm{esc}}$ is the unbound boundary, and only three stars from the final-strict sample sit at or above it.

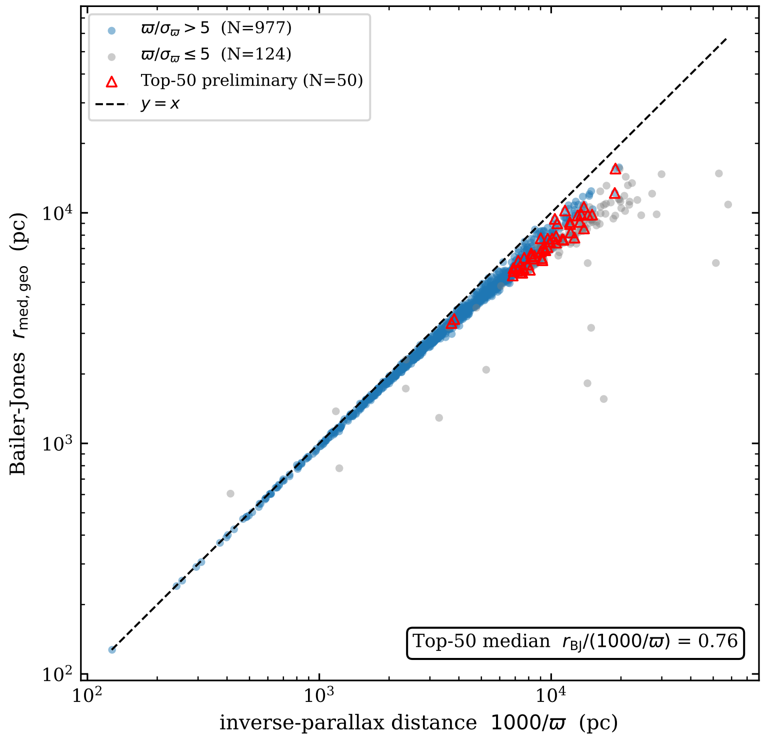

Figure 3. Pairwise comparison of inverse-parallax distances ($1000/\varpi$) and Bailer-Jones (2021) geometric distances ($r_{\mathrm{med,geo}}$). Triangles mark the 50 candidates with the largest preliminary P_{unbound}. Bailer-Jones distances are systematically smaller; the median ratio $r_{\mathrm{med,geo}}/(1000/\varpi)$ is 0.88 across the full 1101-star master sample and 0.76 on the preliminary Top-50.

4.4. Final candidate table

Figure 6 ranks the 30 final-strict candidates with the largest P_{unbound} (Top-30). The upper panel shows the Monte Carlo mean v_{grf} with $\pm 1\sigma$ error bars; the lower panel shows P_{unbound} with the rank-1, 2 and 3 candidates highlighted in red, orange and gold. Only 3 of 30 stars retain $P_{\mathrm{unbound}} > 0.5$ and a single star (rank 1) has $P_{\mathrm{unbound}} > 0.9$. Table 3 lists the Top-15 together with their LAMOST DR9 atmospheric parameters. The full Top-30 with the Monte Carlo dispersions, heliocentric $V_{\mathrm{tot,helio}}$, the per-star escape speed and Δv_{RV} is released as a machine-readable supplementary CSV (`tableA1_supplementary_top30.csv`).

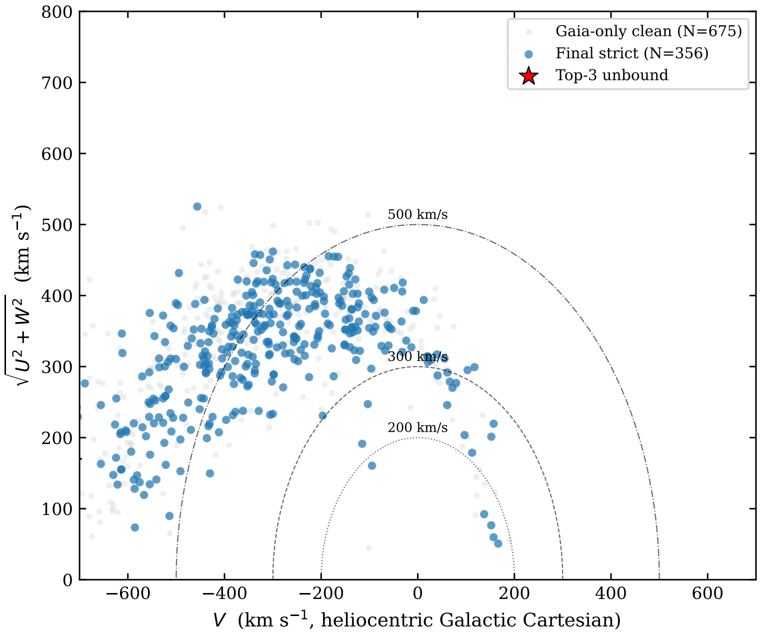

Figure 4. Toomre diagram showing $\sqrt{U^2 + W^2}$ versus V for the Gaia-only clean (grey), the final-strict sample (blue) and the highest-confidence Top-3 unbound candidates (red stars). The velocities are heliocentric Galactic Cartesian, with U positive toward the Galactic centre, V positive in the direction of Galactic rotation and W positive toward the North Galactic Pole; they are not LSR-corrected. Dashed circles mark constant heliocentric peculiar speeds of 200, 300 and 500 $\mathrm{km\,s^{-1}}$.

4.5. Radial-velocity sensitivity

Figure 7 presents the radial-velocity sensitivity check on the final-strict sample. Per-star $v_{\rm grf}$ from Gaia DR3 and LAMOST DR9 radial velocities (panel a) lie almost exactly on the $y = x$ line; the distribution of the difference $\Delta v_{\rm grf}$ = LAMOST − Gaia (panel b) has median 0.00 $\mathrm{km\,s^{-1}}$, $p_{90}|\Delta| = 5.7\,\mathrm{km\,s^{-1}}$ and max $|\Delta| = 32.0\,\mathrm{km\,s^{-1}}$. Of the 356 final-strict stars only one flips $P_{\rm unbound}$ across the 0.5 threshold between the two RV passes. The LAMOST DR9 LRS radial velocities are known to carry an $\approx -5.7\,\mathrm{km\,s^{-1}}$ zero-point offset relative to Gaia DR3 in our matched subset; because we propagate uncertainties through the Monte Carlo, this offset does not propagate to a meaningful change in the main classification.

5. Discussion

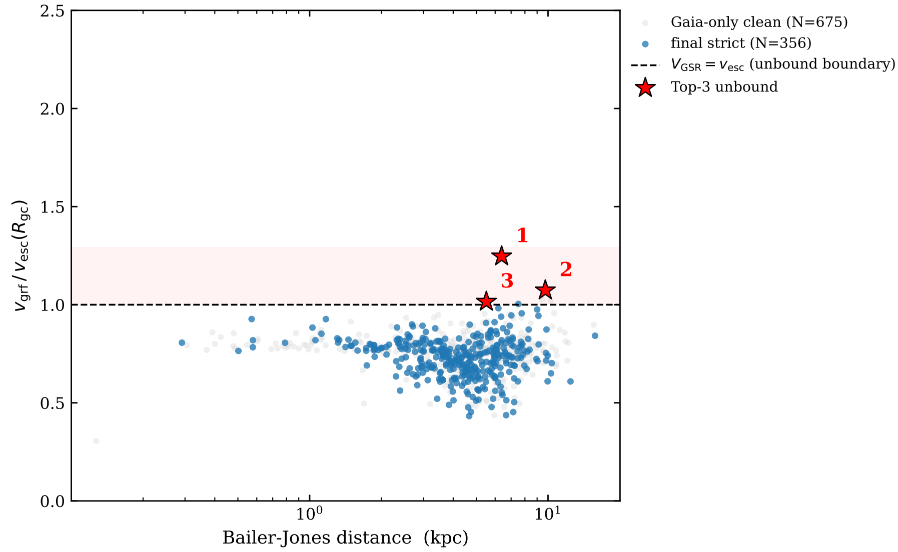

Figure 5. Ratio of the Galactocentric speed $v_{\rm grf}$ to the local escape speed $v_{\rm esc}(R_{\rm gc})$ under MWPotential2014, plotted against Bailer-Jones distance. The dashed horizontal line at $v_{\rm grf}/v_{\rm esc} = 1$ marks the unbound boundary; the lightly shaded region above it is the candidate-unbound zone. The Top-3 stars (red) are the only objects in the final-strict sample that sit close to or above this line.

5.1. Why most preliminary candidates are downgraded

The 24% median distance shrinkage of the Bailer-Jones estimator on the inverse-parallax-flagged unbound subset (Sect. 4.2) is sufficient to explain the same-sample drop from 48 to 3 stars with $P_{\rm unbound} > 0.5$. For tangentially dominated stars the inferred peculiar speed scales linearly with distance; combined with proper-motion uncertainties at the 0.05–0.5 mas yr^{-1} level a 24% distance reduction translates to $O(150\,{\rm km\,s^{-1}})$ change in $V_{\rm tot,helio}$, comparable to the $v_{\rm esc}$–$V_{\rm tot,helio}$ margin in the high-velocity tail. Our results are consistent with the Gaia-DR2-era reassessment of Boubert et al. (2018) and with the Gaia-DR2 fastest-stars analysis of Marchetti et al. (2019), both of which highlighted the strong dependence of unbound classifications on the distance prescription.

5.2. The Top-3 candidates

The three highest-confidence unbound candidates in the final strict sample are:

- **Rank 1**: Gaia DR3 source_id 1383279090527227264, present in both Li et al. (2021) and Liao et al. (2024); $d_{\rm BJ} = 6.39\,{\rm kpc}$, $\overline{v_{\rm grf}} = 653 \pm 55\,{\rm km\,s^{-1}}$,

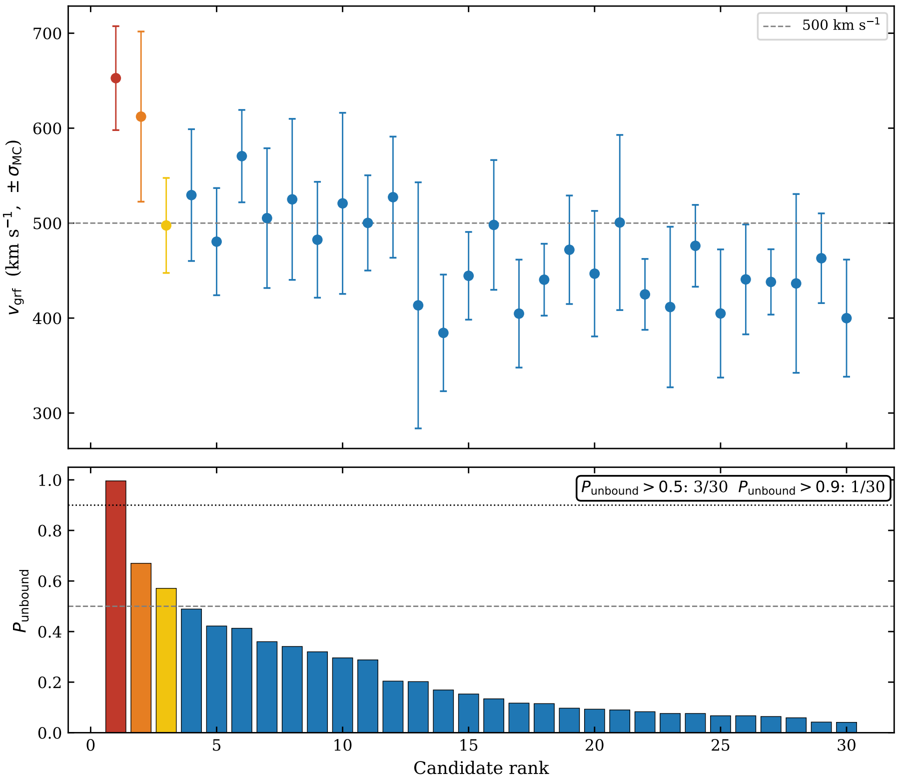

Figure 6. Top-30 final candidates ranked by $P_{\rm unbound}$. *Top:* Monte Carlo mean $v_{\rm grf}$ with $\pm 1\sigma$ error bars (1000 draws per star). *Bottom:* $P_{\rm unbound}$, with the rank-1, 2 and 3 candidates highlighted in red, orange and gold. Reference lines: $P = 0.5$ (dashed), $P = 0.9$ (dotted), and $v_{\rm grf} = 500\,{\rm km\,s^{-1}}$ in the upper panel. After adopting Bailer-Jones geometric distances only 3/30 stars retain $P_{\rm unbound} > 0.5$ and 1/30 retains $P_{\rm unbound} > 0.9$, indicating that the unbound classification is highly sensitive to the choice of distance estimator.

$P_{\rm unbound} = 0.996$; LAMOST atmospheric parameters $T_{\rm eff} = 4801\,{\rm K}$, $\log g = 1.88$, [Fe/H] $= -1.40$, i.e. a metal-poor giant. Independent inclusion in two literature catalogues lends support; recent chemical work on extreme-velocity stars (Nelson et al., 2024) provides relevant context for the population to which this object likely belongs.

- **Rank 2**: Gaia DR3 source_id 1204061267883975040 (liao2024 only), $d_{\rm BJ} = 9.74\,{\rm kpc}$, $\overline{v_{\rm grf}} = 612 \pm 90\,{\rm km\,s^{-1}}$, $P_{\rm unbound} = 0.670$; very metal-poor ([Fe/H] $= -2.38$).

Table 3. Top-15 final high-velocity candidates ranked by $P_{\rm unbound}$. The full Top-30 with the Monte Carlo dispersions, heliocentric $V_{\rm tot,helio}$ and $\Delta v_{\rm RV}$ is released as a machine-readable supplementary CSV (`tableA1_supplementary_top30.csv`).

rank	Gaia DR3 source_id	catalogues [kpc]	$d_{\rm BJ}$ [$\mathrm{km\,s^{-1}}$]	$\overline{v_{\rm grf}}$	$P_{\rm unbound}$ [K]	$T_{\rm eff}$	$\log g$	[Fe/H]	notes
1	1383279090527227264	li2021,liao2024	6.39	653	0.996	4801	1.88	-1.40	high-confidence unbound; dual-catalogue
2	1204061267883975040	liao2024	9.74	612	0.670	4612	1.18	-2.38	likely unbound
3	3877058564258758656	liao2024	5.51	498	0.571	5143	2.29	-1.21	likely unbound
4	1375165725506487424	li2021,liao2024	7.51	530	0.489	4242	0.75	-1.29	dual-catalogue
5	2105847208541125248	liao2024	9.00	480	0.422	4507	1.08	-1.22	—
6	4450458649852400640	liao2024	6.19	571	0.413	4758	1.72	-1.59	—
7	1477675943342041472	liao2024	7.75	505	0.360	4799	1.67	-1.66	—
8	1297316350890352000	liao2024	9.11	525	0.341	4431	1.25	-1.23	—
9	3960007851762445696	li2021,liao2024	6.36	482	0.320	4928	2.13	-1.34	dual-catalogue
10	3651065597121243648	liao2024	5.50	521	0.296	5059	2.35	-2.11	—
11	1480182073940289024	liao2024	7.02	500	0.288	5667	3.54	-1.78	—
12	4429980078286167424	liao2024	5.97	527	0.204	4988	2.37	-1.67	—
13	3696393857329932672	liao2024	5.66	413	0.202	6523	4.29	-1.07	—
14	2125719266307162240	liao2024	15.75	384	0.169	4148	1.17	-0.73	—
15	1850497933774341504	liao2024	6.90	445	0.153	5595	3.13	-1.12	—

– **Rank 3**: Gaia DR3 source_id 3877058564258758656 (liao2024 only), $d_{\rm BJ} = 5.51\,\mathrm{kpc}$, $\overline{v_{\rm grf}} = 498 \pm 50\,\mathrm{km\,s^{-1}}$, $P_{\rm unbound} = 0.571$; metal-poor giant ($T_{\rm eff} = 5143\,\mathrm{K}$, $\log g = 2.29$, $[\mathrm{Fe/H}] = -1.21$).

All three are giant or sub-giant late-type stars with metallicities typical of the Galactic halo, consistent with the late-type HVS candidate populations discussed by Li et al. (2020) and the Gaia–LAMOST high-velocity samples of Du et al. (2018a,b).

We checked the three sources against SIMBAD on 2026 April 30. Rank-1 is catalogued there as UCAC4 656-058031, with the SIMBAD position imported directly from Gaia DR3 (2020yCat.1350); rank-2 is present only as the Gaia DR3 entry itself; rank-3 has no SIMBAD record within 5 arcsec of its Gaia coordinates. None of the three carries a published variability, binarity or spectroscopic-binary flag at the time of writing. The only external corroboration we identify is the dual-catalogue inclusion of rank-1 in both Li et al. (2021) and Liao et al. (2024); this is also the only object in our sample with $P_{\rm unbound} > 0.9$. The absence of flags is, of course, not equivalent to a confirmation of single-star status: targeted multi-epoch spectroscopy of the kind reported by Hattori et al. (2019) for LAMOST-HVS1 remains the most direct test. We do not claim discovery; the Top-3 are reassessments of stars already present in the literature.

5.3. Gaia versus LAMOST radial velocities

The median difference LAMOST − Gaia $= -5.66\,\mathrm{km\,s^{-1}}$ in the matched subset (Sect. 4.5) reflects the well-documented LAMOST DR9 LRS zero-point offset. We have not applied a zero-point correction in the primary kinematic solution, because the main classification is insensitive to it: the median $\Delta v_{\rm grf}$ on the

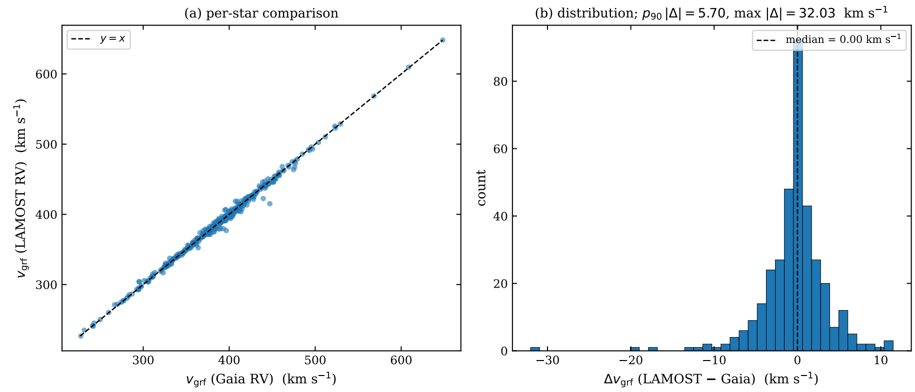

Figure 7. Radial-velocity sensitivity on the final-strict sample (N=356). *Panel (a):* per-star $v_{\rm grf}$ computed with Gaia DR3 radial velocities versus the same quantity computed with LAMOST DR9 radial velocities. *Panel (b):* histogram of the difference $\Delta v_{\rm grf}$ = LAMOST − Gaia; median = $0.00\,{\rm km\,s^{-1}}$, $p_{90}|\Delta| = 5.7\,{\rm km\,s^{-1}}$, $\max|\Delta| = 32.0\,{\rm km\,s^{-1}}$. The unbound classification is essentially insensitive to the choice of RV.

final-strict sample is $0.00\,{\rm km\,s^{-1}}$, the p_{90} absolute deviation is $5.7\,{\rm km\,s^{-1}}$, and the chemical tagging arguments of Hawkins & Wyse (2018) and Bromley et al. (2018) also do not require sub-${\rm km\,s^{-1}}$ RV accuracy.

5.4. Limitations and follow-up

Four sources of systematic uncertainty affect the main numerical results. The first is the escape-speed approximation: $v_{\rm esc}$ is evaluated in the disk plane ($z = 0$), and off-plane corrections under MWPotential2014 are at the few-percent level. Because rank-2 and rank-3 sit close to the unbound boundary at $P_{\rm unbound} = 0.670$ and 0.571, their classification can flip under alternative potentials such as those of McMillan (2017) and Piffl et al. (2014); Monari et al. (2018). Only rank-1 ($P_{\rm unbound} = 0.996$) survives such variations as a robust unbound candidate; ranks 2 and 3 should be treated as marginal pending external confirmation. The second concerns the Bailer-Jones prior: it is tuned to the Galactic disk and may itself shrink the distances of genuine halo high-velocity tracers. The 48-to-3 reduction is therefore prior-dependent rather than a definitive measurement, and we phrase it that way throughout. The third systematic is sample geometry. LAMOST coverage is largely restricted to the northern hemisphere and the Li et al. (2023) subset contributes zero objects to the final-strict sample under our cross-match and quality criteria. Conclusions about atmospheric parameters therefore rest on the Li et al. (2021) and Liao et al. (2024) subsets only. The fourth is unresolved binarity: it can inflate the apparent radial velocity, and the two stars with $|\Delta v_{RV}| > 50\,km\,s^{-1}$ that otherwise pass our quality gates are the natural targets for multi-epoch follow-up.

The follow-up programme implied by these results is therefore: (a) targeted high-resolution spectroscopy of the Top-3 candidates to confirm or refute their unbound status under a panel of Galactic potentials (e.g. McMillan, 2017; Piffl et al., 2014; Monari et al., 2018); (b) multi-epoch radial-velocity monitoring of the two RV-outlier follow-up targets; and (c) re-running the present pipeline with Gaia DR4 parallaxes once they become available—we expect the parallax error budget to halve and the BJ-vs-inverse-parallax distance gap to narrow.

6. Conclusions

1. For the 356-star final-strict subset of three published HVS catalogues (Li et al., 2021, 2023; Liao et al., 2024), replacing inverse-parallax distances with Bailer-Jones geometric distances reduces the count of likely-unbound stars ($P_{unbound} > 0.5$) from *48* to *3* and the count of high-confidence unbound stars ($P_{unbound} > 0.9$) from *12* to *1*. 45 stars are downgraded across $P_{unbound} = 0.5$ and none are promoted.

2. The reduction is driven by a systematic distance shrinkage of 12 % across the strict sample, rising to 24 % on the subset that the inverse-parallax pass had flagged as $P_{unbound} > 0.5$. Substituting LAMOST radial velocities for Gaia radial velocities on the same sample changes the median v_{grf} by $0\,km\,s^{-1}$ ($p_{90}|\Delta| = 5.7\,km\,s^{-1}$) and flips the $P_{unbound} = 0.5$ classification of only one star. The unbound classification is therefore distance-dominated, not RV-dominated.

3. We release a final-strict sample of 356 stars, a Top-15 main candidate table (Table 3) and a supplementary Top-30 as a machine-readable CSV. The three highest-confidence candidates are the metal-poor giants Gaia DR3 `1383279090527227264`, `1204061267883975040` and `3877058564258758656`; targeted spectroscopic follow-up is recommended.

4. Two stars with $|\Delta_{rv}\,(\mathrm{LAMOST} - \mathrm{Gaia})| > 50\,km\,s^{-1}$ are flagged as binary or variable-RV candidates; we do not include them in the principal unbound list and report them separately as follow-up targets.

All raw queries, the kinematic solver, the figure- and table-generation scripts and the unit tests are publicly available at `https://github.com/Harry33t/caosp-hivel-pipeline` under the MIT license. A versioned snapshot will be assigned a permanent DOI upon acceptance. The Top-30 machine-readable supplementary CSV is included with the submission package.

Acknowledgements

We thank the anonymous referee whose detailed comments substantially improved the robustness analysis and the presentation of this work. This work has made use of data from the European Space Agency mission *Gaia* (https://www.cosmos.esa.int/gaia), processed by the *Gaia* Data Processing and Analysis Consortium. Funding for the DPAC has been provided by national institutions, in particular the institutions participating in the *Gaia* Multilateral Agreement. Guoshoujing Telescope (LAMOST) is a National Major Scientific Project built by the Chinese Academy of Sciences. This research has made use of the VizieR catalogue access tool, CDS, Strasbourg, France (Ochsenbein et al., 2000). Software: `astropy` (Astropy Collaboration et al., 2013, 2018), `astroquery` (Ginsburg et al., 2019), `galpy` (Bovy, 2015).

References

Astropy Collaboration, Price-Whelan, A. M., Sipőcz, B. M., et al., The Astropy Project: Building an Open-science Project and Status of the v2.0 Core Package. 2018, *Astronomical Journal*, **156**, 123, DOI:10.3847/1538-3881/aabc4f

Astropy Collaboration, Robitaille, T. P., Tollerud, E. J., et al., Astropy: A community Python package for astronomy. 2013, *Astronomy and Astrophysics*, **558**, A33, DOI:10.1051/0004-6361/201322068

Bailer-Jones, C. A. L., Estimating Distances from Parallaxes. 2015, *Publications of the ASP*, **127**, 994, DOI:10.1086/683116

Bailer-Jones, C. A. L., Rybizki, J., Fouesneau, M., Demleitner, M., & Andrae, R., Estimating Distances from Parallaxes. V. Geometric and Photogeometric Distances to 1.47 Billion Stars in Gaia EDR3. 2021, *Astronomical Journal*, **161**, 147, DOI:10.3847/1538-3881/abd806

Bennett, M. & Bovy, J., Vertical waves in the solar neighbourhood in Gaia DR2. 2019, *Monthly Notices of the RAS*, **482**, 1417, DOI:10.1093/mnras/sty2813

Boubert, D., Guillochon, J., Hawkins, K., et al., Revisiting hypervelocity stars after Gaia DR2. 2018, *Monthly Notices of the RAS*, **479**, 2789, DOI:10.1093/mnras/sty1601

Bovy, J., galpy: A python Library for Galactic Dynamics. 2015, *Astrophysical Journal, Supplement*, **216**, 29, DOI:10.1088/0067-0049/216/2/29

Bromley, B. C., Kenyon, S. J., Brown, W. R., & Geller, M. J., Nearby High-speed Stars in Gaia DR2. 2018, *Astrophysical Journal*, **868**, 25, DOI:10.3847/1538-4357/aae83e

Brown, W. R., Hypervelocity Stars. 2015, *Annual Review of Astron and Astrophys*, **53**, 15, DOI:10.1146/annurev-astro-082214-122230

Brown, W. R., Geller, M. J., & Kenyon, S. J., The MMT Hypervelocity Star Survey. III. The Complete Survey. 2014, *Astrophysical Journal*, **787**, 89, DOI:10.1088/0004-637X/787/1/89

Brown, W. R., Geller, M. J., Kenyon, S. J., & Kurtz, M. J., Discovery of an Unbound Hypervelocity Star in the Milky Way Halo. 2005, *Astrophysical Journal, Letters*, **622**, L33, DOI:10.1086/429378

Brown, W. R., Geller, M. J., Kenyon, S. J., & Kurtz, M. J., Hypervelocity Stars. II. The Bound Population. 2007, *Astrophysical Journal*, **660**, 311, DOI:10.1086/513595

Cui, X.-Q., Zhao, Y.-H., Chu, Y.-Q., et al., The Large Sky Area Multi-Object Fiber Spectroscopic Telescope (LAMOST). 2012, *Research in Astronomy and Astrophysics*, **12**, 1197, DOI:10.1088/1674-4527/12/9/003

Deng, L.-C., Newberg, H. J., Liu, C., et al., LAMOST Experiment for Galactic Understanding and Exploration (LEGUE)—The Survey's Science Plan. 2012, *Research in Astronomy and Astrophysics*, **12**, 735, DOI:10.1088/1674-4527/12/7/003

Du, C., Li, H., Liu, S., Donlon, T., & Newberg, H. J., The High-velocity Stars in the Local Stellar Halo from Gaia and LAMOST. 2018a, *Astrophysical Journal*, **863**, 87, DOI:10.3847/1538-4357/aad088

Du, C., Li, H., Yan, Y., et al., The Origin of High-velocity Stars Considering the Impact of the Galactic Bar. 2018b, *Astrophysical Journal, Letters*, **869**, L31, DOI:10.3847/2041-8213/aaf578

Elsanhoury, W. H., Kinematics of high-velocity stars utilizing LAMOST and Gaia DR3 archives within 100 kpc. 2025, *Contributions of the Astronomical Observatory Skalnaté Pleso*, **55**, 38, DOI:10.31577/caosp.2025.55.1.38

Gaia Collaboration, Vallenari, A., Brown, A. G. A., et al., Gaia Data Release 3: Summary of the content and survey properties. 2023, *Astronomy and Astrophysics*, **674**, A1, DOI:10.1051/0004-6361/202243940

Ginsburg, A., Sipőcz, B. M., Brasseur, C. E., et al., astroquery: An Astronomical Web-querying Package in Python. 2019, *Astronomical Journal*, **157**, 98, DOI:10.3847/1538-3881/aafc33

Gravity Collaboration, Abuter, R., Amorim, A., Anugu, N., et al., Detection of the gravitational redshift in the orbit of the star S2 near the Galactic centre massive black hole. 2018, *Astronomy and Astrophysics*, **615**, L15, DOI:10.1051/0004-6361/201833718

Hattori, K., Valluri, M., Castro, N., et al., Origin of a Massive Hyper-runaway Subgiant Star LAMOST-HVS1: Implication from Gaia and Follow-up Spectroscopy. 2019, *Astrophysical Journal*, **873**, 116, DOI:10.3847/1538-4357/ab05c8

Hawkins, K. & Wyse, R. F. G., The fastest travel together: chemical tagging of the fastest stars in Gaia DR2 to globular clusters. 2018, *Monthly Notices of the RAS*, **481**, 1028, DOI:10.1093/mnras/sty2282

Hills, J. G., Hyper-velocity and tidal stars from binaries disrupted by a massive Galactic black hole. 1988, *Nature*, **331**, 687, DOI:10.1038/331687a0

Kenyon, S. J., Bromley, B. C., Geller, M. J., & Brown, W. R., Hypervelocity Stars: From the Galactic Center to the Halo. 2008, *Astrophysical Journal*, **680**, 312, DOI:10.1086/587738

Li, J., Liu, C., Xue, X.-X., et al., Three new late-type hypervelocity star candidates from SDSS, LAMOST and Gaia. 2020, *Research in Astronomy and Astrophysics*, **20**, 42, DOI:10.1088/1674-4527/20/3/42

Li, Q.-Z., Lu, Y.-J., Yang, T.-G., Qiu, K.-N., & Liao, J., On the Origins of Extreme Velocity Stars as Revealed by Large-scale Galactic Surveys. 2023, *Astronomical Journal*, **166**, 12, DOI:10.3847/1538-3881/acd1dc

Li, Y.-B., Luo, A.-L., Lu, Y.-J., et al., 591 High-velocity Stars in the Galactic Halo Selected from LAMOST DR7 and Gaia DR2. 2021, *Astrophysical Journal, Supplement*, **252**, 3, DOI:10.3847/1538-4365/abc16e

Liao, J., Lu, Y.-J., Mu, H.-J., & Yang, T.-G., The Origin of High-velocity Stars Considering the Impact of the Large Magellanic Cloud. 2024, *Astronomical Journal*, **167**, 76, DOI:10.3847/1538-3881/ad18c4

Lindegren, L., Bastian, U., Biermann, M., et al., Gaia Early Data Release 3. Parallax bias versus magnitude, colour, and position. 2021, *Astronomy and Astrophysics*, **649**, A4, DOI:10.1051/0004-6361/202039653

Luri, X., Brown, A. G. A., Sarro, L. M., et al., Gaia Data Release 2. Using Gaia parallaxes. 2018, *Astronomy and Astrophysics*, **616**, A9, DOI:10.1051/0004-6361/201832964

Marchetti, T., Rossi, E. M., & Brown, A. G. A., Gaia DR2 in 6D: searching for the fastest stars in the Galaxy. 2019, *Monthly Notices of the RAS*, **490**, 157, DOI:10.1093/mnras/sty2592

McMillan, P. J., The mass distribution and gravitational potential of the Milky Way. 2017, *Monthly Notices of the RAS*, **465**, 76, DOI:10.1093/mnras/stw2759

Monari, G., Famaey, B., Carrillo, I., et al., The escape speed curve of the Galaxy obtained from Gaia DR2 implies a heavy Milky Way. 2018, *Astronomy and Astrophysics*, **616**, L9, DOI:10.1051/0004-6361/201833748

Nelson, T., Ting, Y.-S., Hawkins, K., et al., A detailed chemical study of the extreme velocity stars in the Galaxy. 2024, *Monthly Notices of the RAS*, **532**, 2875, DOI:10.1093/mnras/stae1656

Ochsenbein, F., Bauer, P., & Marcout, J., The VizieR database of astronomical catalogues. 2000, *Astronomy and Astrophysics, Supplement*, **143**, 23, DOI:10.26093/cds/vizier

Piffl, T., Scannapieco, C., Binney, J., et al., The RAVE survey: the Galactic escape speed and the mass of the Milky Way. 2014, *Astronomy and Astrophysics*, **562**, A91, DOI:10.1051/0004-6361/201322531

Reid, M. J. & Brunthaler, A., The Proper Motion of Sagittarius A*. III. The Case for a Supermassive Black Hole. 2020, *Astrophysical Journal*, **892**, 39, DOI:10.3847/1538-4357/ab76cd

Schönrich, R., Binney, J., & Dehnen, W., Local kinematics and the local standard of rest. 2010, *Monthly Notices of the RAS*, **403**, 1829, DOI:10.1111/j.1365-2966.2010.16253.x

Xiang, M.-S., Liu, X.-W., Yuan, H.-B., et al., The LAMOST stellar parameter pipeline at Peking University – LSP3. 2015, *Monthly Notices of the RAS*, **448**, 822, DOI:10.1093/mnras/stu2692

Yan, H.-L., Zhou, Y.-T., Zhang, X., et al., Overview of the LAMOST survey in the first decade. 2022, *The Innovation*, **3**, 100224, DOI:10.1016/j.xinn.2022.100224

Yu, Q. & Tremaine, S., Ejection of Hypervelocity Stars by the (Binary) Black Hole in the Galactic Center. 2003, *Astrophysical Journal*, **599**, 1129, DOI:10.1086/379546

Zhao, G., Zhao, Y.-H., Chu, Y.-Q., Jing, Y.-P., & Deng, L.-C., LAMOST spectral survey – An overview. 2012, *Research in Astronomy and Astrophysics*, **12**, 723, DOI:10.1088/1674-4527/12/7/002

Contrib. Astron. Obs. Skalnaté Pleso **56/3**, 54 – 67, (2026)
https://doi.org/10.31577/caosp.2026.56.3.54

Multivariate analysis of globular cluster system scaling relations: The roles of galaxy structure and evolution

Ahmed H. Abdullah, Anas Salman Taha and Abdullah K. Ahmed

Department of Astronomy and Space, College of Science, University of Baghdad, Baghdad, Iraq (E-mail: ahmed.h.abdullah@sc.uobaghdad.edu.iq)

Received: March 25, 2026; Accepted: May 25, 2026

Abstract. In this work, we present improved scaling relations for globular cluster systems (GCS) and examine how type, elliptic shape (ϵ), systemic velocity ($V_{\rm sys}$), Sérsic index (n), dynamic index ($R_e \times \sigma$), light profile slope (α, γ) and age affect the number of globular clusters ($N_{\rm GCs}$). To get a better understanding of the formation and development mechanisms of globular clusters, we separate the influence of the structural and dynamic parameter using several source data from SLUGGS, ACSVCS, and Forbes et al. (2018). Our findings support the presence of a precise co-evolution scenario where the halo's age, shape, and depth all have distinct effects on globular cluster abundance.

Key words: globular clusters – number of globular clusters – age – galaxy formation – dynamical parameters

1. Introduction

Among the earliest stellar systems, globular clusters are essential to comprehending the history and evolution of galaxies, De Bórtoli et al. (2022). These systems have endured over several cosmic epochs, offering important insights into the early universe's star formation circumstances, Al-Mashhadani & Abdullah (2020). The stars within GC are in a compact structure distinguished by very high stellar density, low metallicities and relatively uniform ages. These GCs are important for studying the formation and history of their host systems because they exist in a wide range of environments, from dwarf satellites to massive elliptical galaxies Gieles et al. (2025).

The number of globular cluster ($N_{\rm GC}$) along with the properties of the host galaxy, has revealed scaling relations which enable us to comprehend how a galaxy's mass is obtained and evolves over time, Le & Cooper (2025). The previous studies (e.g., Harris & Van den Bergh (1981); Ashman & Zepf (1992)) well established a crucial relation between the number of GCs and the host galaxy's luminosity, stellar mass, and DM halo mass.

Recently, the new datasets from space based imaging and wide field ground-based surveys have polished these relations. The strong correlation between the galactic halo mass and the total mass of the globular cluster system are confirmed by Hudson et al. (2015) and Harris et al. (2015).

A primary motivation for these studies is the scaling relation that lies in the contradictory aspect of GCs: they are both outgrowth of hierarchical mergers and in situ remnants of ancient stellar population. Their spatial distribution, abundance and structural characteristics reflect the local of star formation condition, also the expanding halo growth history of the host system, Park et al. (2022).

The improvement of simulation techniques and the emergence of cosmological models, such as E-MOSAICS (Kruijssen et al., 2019), provided enhanced prospects to interpret the scaling relation within a physical framework that links them to the temporal and environmental evolution of galaxies and their mass sequences.

This paper expands a field of analyses to incorporate structural and dynamic variables, which includ the dynamic proxy, Sérsic index and light profile slope. We examine the effects of these parameters, individually and together, on $N_{\rm GC}$ to uncover secondary factors contributing to the diversity of GC populations. The paper is divided into the following : Section 2 presents data, and the methodology . Section 3 explores relation between the $N_{\rm GC}$ and the type and examines additional correlations with ellipticity, the product of the effective radius and velocity dispersion ($R_e \times \sigma$), and stellar age. Finally, we discuss the implications of our findings for GC and galaxy formation models.

2. Data and methodology

To understand how the GC scaling relation vary among galaxy types, we assembled a carefully selected sample. This sample covers a comprehensive range for systems., from early to the late type, with star masses $\log(M_*/M_\odot)$ ranging from approximately 10.2 to 11.8. The fundamental was to obtain the right measurements, for both directly observed and to accurately calculated. Which aim to get the number, shapes, and the internal motions for GCs.

SLUGGS data (SAGES Leacy Unifying Globulars and GalaxieS Survey), Brodie et al. (2014) form the core of study's dataset. Which supplying a wide range of the spectral and optical observations detailed for GCs, in nearby-early types galaxies. The SLUGGS data used in the work covers a much wider range of effective radii, enabling us to estimate masses of the galaxies at the edges, regions critical to understand how GCs form. For smaller radii in cluster environments, we included data from the ACS Virgo Cluster Survey, (ACSVCS) Jordán et al. (2009).

Globular clusters and their structure in the Virgo Cluster are precisely measured thanks to the Hubble Space Telescope mission. Additionally, we have integrated systems from the Forbes et al. (2018) catalog. This assemblage connects galactic properties like star masses and dark matter halos to globular cluster data, such as the masses of globular clusters and N_{GC}. It allows us to understand how the environment affects the efficiency of globular cluster formation since it covers a broad range of environments, from dense cluster to isolate galaxies. When combined, these data provide us a comprehensive and detailed understanding of the relationship between globular clusters and the characteristics of their host galaxy.

Linear fits were performed using the ordinary least squares (OLS) method after verifying the approximate normal distribution of the residuals. The strength of the correlation was reported using the Pearson correlation coefficient (r), with two-tailed P values to test the zero hypothesis for no correlation.

3. Results and analysis

3.1. Number of GC and galaxy types

The distribution of the number of globular clusters (N_{GCs}) among various morphological types of galaxies in the sample under analysis is shown in Figure 1. In contrast to later galaxies, such as spiral (Sa) galaxies, early galaxies, especially lenticular (S0) and elliptical (E) galaxies, tend to contain richer globular clusters, as the figure illustrates.

This distribution offers many significant insights. With a distinct tail that extends into systems with hundreds of globular clusters, E-type galaxies have the largest range. This notable variation is presumably due to the varied formation history of E-type galaxies, whose globular cluster formation efficiency was likely significantly increased by huge mergers and abundant early star formation, Abdullah & Kroupa (2021); De Lucia et al. (2024).

The S0-type galaxies, on the other hand, have a considerably denser distribution, indicating a more uniform evolutionary path that may be controlled by passive aging and small accretion events, even if they still occupy the upper end of the distribution.

The inclusion of the composite E/S0 galaxies category has enable us to link the two classes, indicating a gradation in structural properties and formation history, which is reflected in their stock of GCs Meantime, Sa-type spiral galaxies usually occupy the lower end of the spectrum.

3.2. The number of globular clusters and ellipticity (ϵ)

There is a definite inverse relationship between the number of globular cluster systems and the elliptical shape of the galaxy (Figure 2). The falling curve shows that richer GC systems are often found in more spherical galaxies (low ϵ value), while fewer GC systems are associated with more elongated galaxies (higher ϵ value). The history of galaxy formation and structure evolution is implicitly reflected in this inverse relationship. Intense early star formation and the violent dynamical conditions are frequently linked to the elliptical galaxies, for the dense

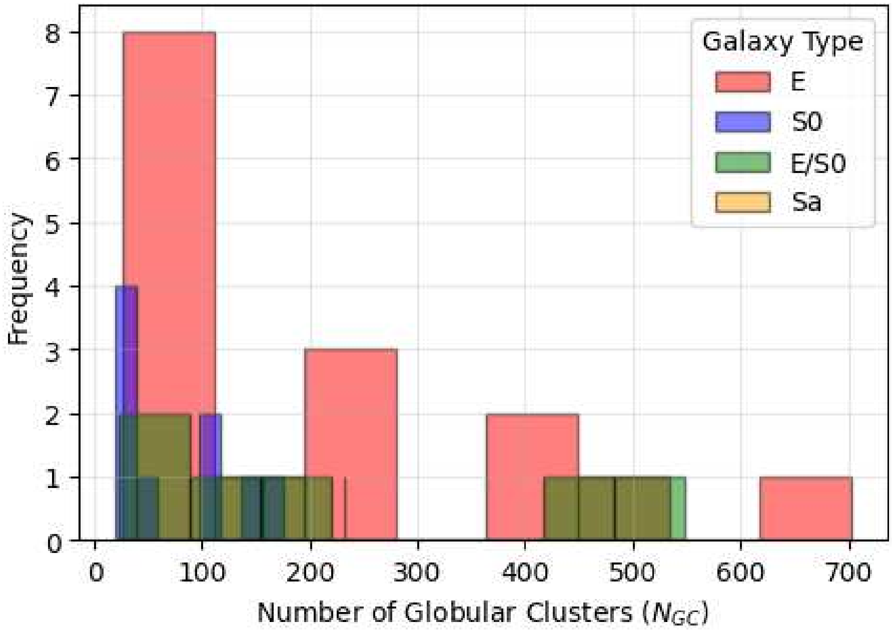

Figure 1. Frequency distribution of the number of GCs over morphological classes, (E= elliptical, $S0$= lenticular, Sa =spiral type a). This displays a clear bias for earlier – type galaxies and emphasizes the tendency of E and S0 galaxies to host richer GCs compared to their later complement.

central bulge (and lower elongation) provide a favorable environment for the formation of numerous massive GCs during bursts of star formation, Valenzuela et al. (2025); Berkheimer et al. (2026). On the other hand, the more elongated shapes may be a sign of rotational effects, a different merger history, or a less intensive star forming environment, that would lead to less effective cluster formation or retention.

The best linear fit can be expressed as follows:

$$N_{\rm GC} = (-392.96 \pm 141.38) \times \epsilon + (299.93 \pm 51.81), \quad (1)$$

with Pearson correlation coefficient (r)=-0.453, p- value (significance)= 0.0093 and coefficient of determination (R^2)= 0.205.

3.3. The number of globular clusters and systemic velocity ($V_{\rm sys}$)

Figure 3 illustrates the relationship between the number of globular clusters in a galaxy and the system velocity ($V_{\rm sys}$), a measure of the galaxy's radial velocity relative to the observer. Unlike some other internal physical measurements

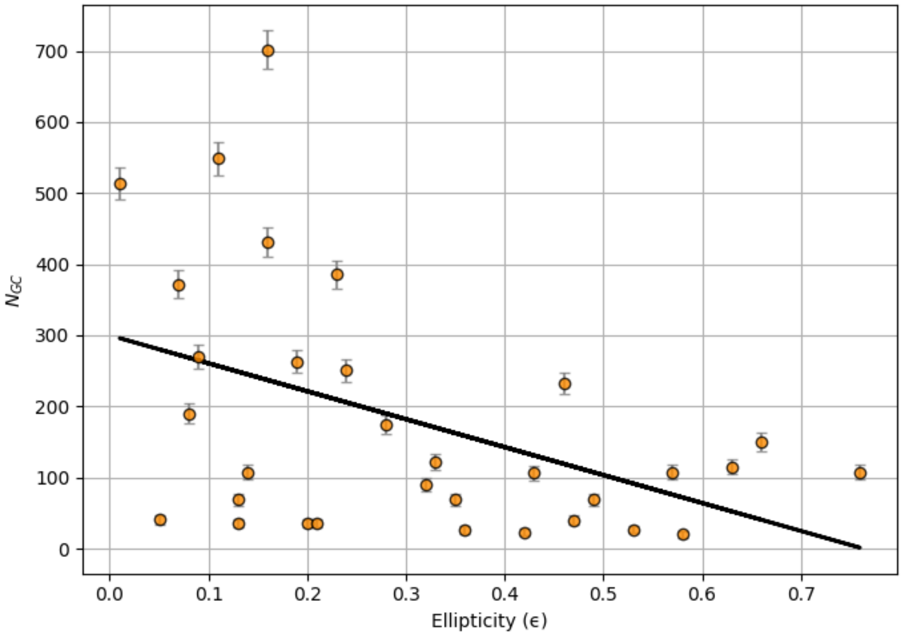

Figure 2. The relationship between the number of globular clusters and the ellipticity of the galaxy. Vertical error bars represent Poisson uncertainties ($\sqrt{N_{\rm GC}}$).This inverse relationship shows that galaxies with a lower ellipticity (more spherical) tend to contain a larger number of globular clusters.

analyzed in this study, the data here show a wide dispersion without a clear linear or statistically significant trend. This wide dispersion of points around the general trend line suggests that the system velocity, in itself, is not a major factor in determining globular cluster abundance. The linear fit is given by:

$$N_{\rm GC} = (-0.0268 \pm 0.0708) \times V_{\rm sys} + (210.84 \pm 89.47), \tag{2}$$

with r=-0.069, p- value $= 0.707$ and $R^2 = 0.0048$.

From an astrophysical perspective, this conclusion is not surprising. The $V_{\rm sys}$ primarily reflects the relative motion of a galaxy within the local or cluster cosmic framework and is strongly influenced by the galaxy's position within the large-scale cosmic web and its own motion, Issa & Abdullah (2024); Dolfi et al. (2021). Therefore, this velocity is not directly related to the internal processes of formation and evolution that govern the efficiency of globular cluster formation and survival, such as the depth of the gravitational well, the history of mergers, or the density of the interstellar medium in the early cosmic ages.

The weak correlation shown in Figure 3 confirms a key hypothesis that the richness of a globular cluster system is a local record of the internal structural and dynamic evolution of the host galaxy. The systemic velocity is still an external quantity that does not directly display the conditions that generated the cluster system, even if properties like mass, centripetal dispersion velocity, or appearance shape may show closer relationships with the host galaxy.

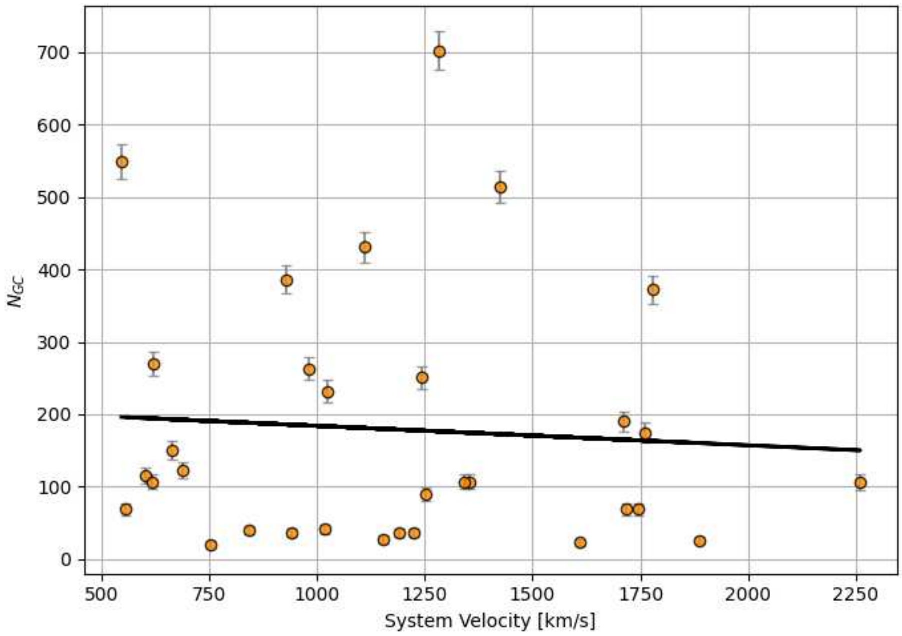

Figure 3. The total number of globular star clusters in proportion to the system velocity ($V_{\rm sys}$). The large dispersion indicates that local forces predominate.Vertical error bars represent Poisson uncertainties ($\sqrt{N_{\rm GC}}$).

3.4. The number of globular clusters and the dynamical mass proxy ($R_e \times \sigma$)

The total number of globular clusters is shown as a function of the dynamic mass proxy ($R_e \times \sigma$) in Figure 4. The assumption that the depth of gravitational potential, not just merely stellar mass, determines the capacity to form and maintain GCs is supported by the dispersion plot, which shows a strong and obvious association.

The following is an expression for the best-fit linear relation:

$$N_{\rm GC} = (0.0665 \pm 0.0215) \times R_e \cdot \sigma + (89.50 \pm 39.93), \tag{3}$$

with r=0.492, p- value = 0.0042 and R^2= 0.242.

Dynamic mass is resolved by multiplying the effective radius (R_e) by the velocity dispersion (σ). The assumption that gravitational efforts are more effective in producing and sustaining GCs is supported by our results, which show a rather high correlation with $N_{\rm GC}$. This supports the theoretical prediction that the development of GCs is more closely associated with the halo binding energy than with baryonic mass indices alone, Kruijssen et al. (2019).

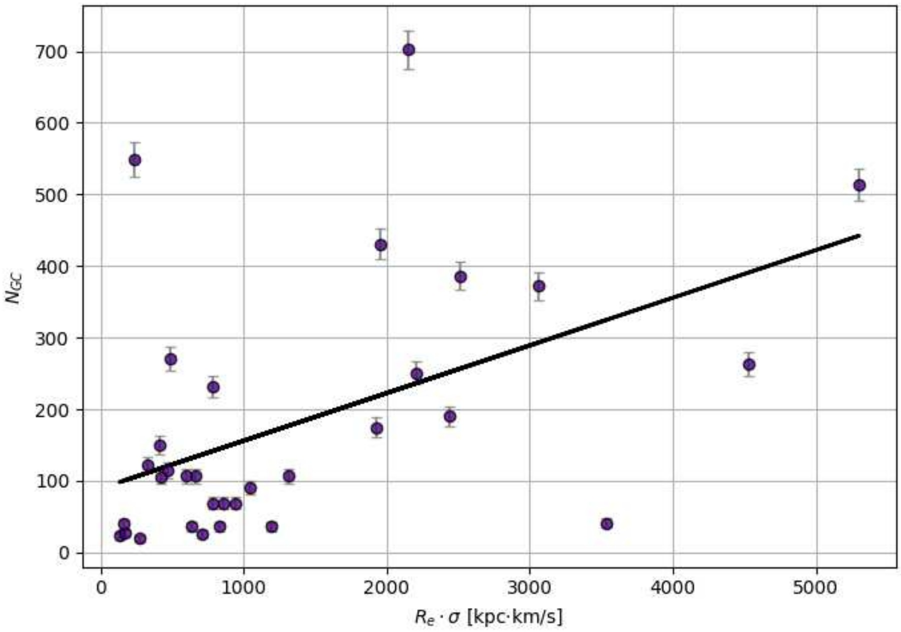

Figure 4. The total number of globular clusters in relation with the dynamic mass proxy ($R_e \times \sigma$).Vertical error bars represent Poisson uncertainties ($\sqrt{N_{\rm GC}}$).

3.5. The number of globular cluster and Sérsic index (n)

The relation between the $N_{\rm GC}$ and the Sérsic index (n), a structural parameter that determines a galaxy's concentration of light profile, is shown in Figure 5. The best linear relationship is

$$N_{\rm GC} = (33.45 \pm 18.80) \times n + (15.07 \pm 96.96), \tag{4}$$

with r=0.4667, p- value = 0.0071 and R^2= 0.217.

A high number of globular clusters are often found in galaxies with higher concentrations toward centers, as indicated by a larger value of n. This is perhaps due to earlier phases of central bulge development and a stronger central gravitational field.

As n increases, we observe a slight rise in $N_{\rm GC}$. This trend implies that there are more GCs in galaxies with higher center star densities. This might point out to early bulge formation conditions that facilitate the production of huge clusters, such as high gas density and quick dynamic times, Lim et al. (2025).

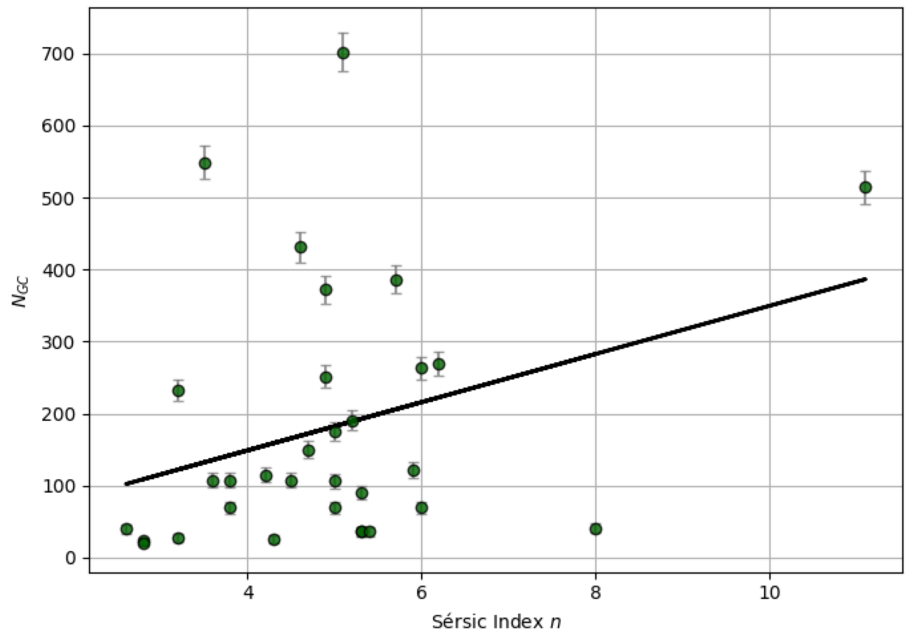

Figure 5. Total number of globular cluster in relation to the Sérsic Index (n).Vertical error bars represent Poisson uncertainties ($\sqrt{N_{\rm GC}}$). Richer cluster systems are typically found in galaxies with more concentrated light distributions.

3.6. The number of globular clusters and light profile slope (α)

We model the galaxy surface brightness profile $I(R)$ as a broken power law :

$$I(R) \propto \begin{cases} R^{-\gamma}, & \text{for } R \leq R_{\rm break}, \\ R^{-\alpha}, & \text{for } R > R_{\rm break}, \end{cases} \tag{5}$$

where γ is the inner slope and α is the outer slope, taken from the SLUGGS catalog, Brodie et al. (2014).

The relation between $N_{\rm GC}$ and the outward slope (α) of the galactic surface brightness profile is shown in Figure 6. Flatter outer slopes indicate more extended, denser stellar halos, which are associated with more globular clusters, likely as a result of past accretion processes. The linear fit reveals a negative trend:

$$N_{\rm GC} = (-471.19 \pm 154.00) \times \alpha + (259.95 \pm 38.20), \quad (6)$$

with r=-0.488, p- value = 0.0046 and R^2= 0.238.

The outward slope (α) of the galactic surface brightness profile is only weakly correlated with $N_{\rm GC}$. However, systems with steep outer profiles tend to have a greater number of globular clusters. This suggests that the extended stellar halos that retain information about accretion satellites may be GCs, Brodie et al. (2014); Elmegreen & Efremov (1997).

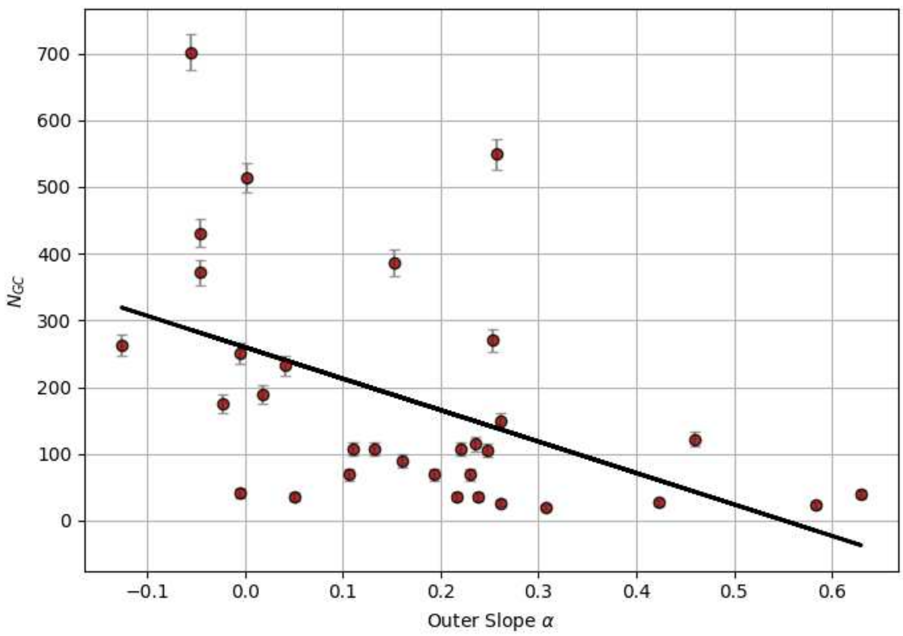

Figure 6. Total number of globular clusters versus the outer light profile of the galaxy (α). The weak negative trend indicates that flatter outer halos are associated with richer globular cluster systems.

3.7. The number of globular clusters and inner light profile slope (γ)

The number of GCs is plotted against the inner light slope (γ) (Figure 7). The inverse trend is expressed by the following equation:

$$N_{\mathrm{GC}} = (-324.78 \pm 62.4) \times \gamma + (1138.86 \pm 175.76) \quad (7)$$

With r=-0.689, p- value = 1.43×10^{-5} and R^2= 0.474.

The light concentration, as indicated by the internal slope, shows a limited but significant correlation with the N_{GC}, with low γ values tending to have a greater number of GCs and, consequently, flatter inner profiles. This may arise from dynamic heating resulting from early merger, linking GCs to ancient structural assembly events, Forbes et al. (2020).

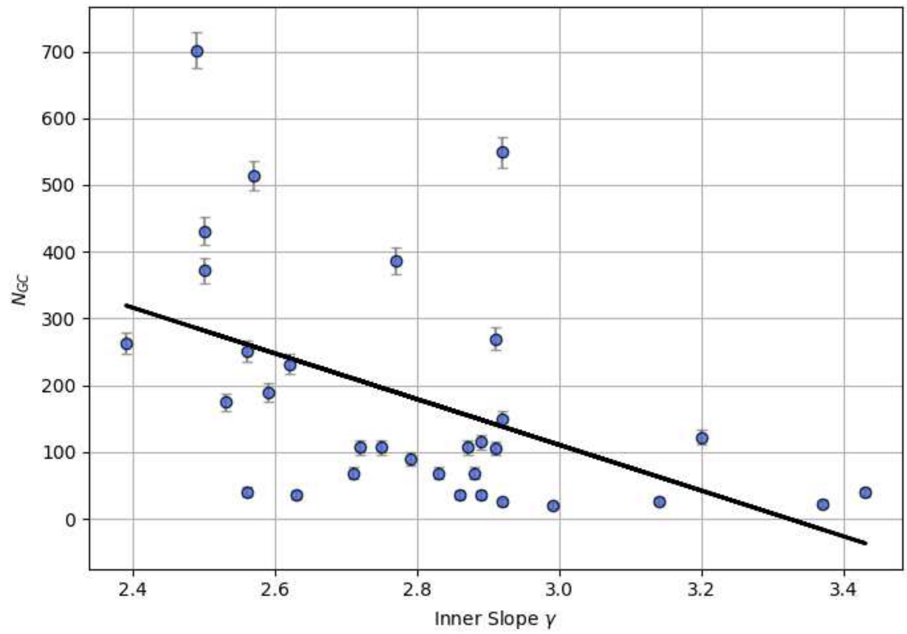

Figure 7. Number of GCs versus the inner slope (γ) of the surface brightness profile. Vertical error bars represent Poisson uncertainties ($\sqrt{N_{\mathrm{GC}}}$).The weak inverse trend suggests that flatter central profiles may be associated with early cluster formation resulting from a merger.

3.8. The number of globular clusters and stellar age

Figure 8 illustrates the relationship between the total number of globular clusters and the mean stellar population age of galaxies. The resulting linear relationship is given by

$$, N_{\rm GC} = (23.51 \pm 8.24) \times \text{age} - (95.84 \pm 95.88), \tag{8}$$

with r=0.4752, p- value = 0.0068 and R^2= 0.2258.

This fit reveals a gradual positive trend: older galaxies tend to contain more globular clusters. This finding supports the hypothesis that globular cluster formation was more efficient in the early universe, when the interstellar medium was denser and star-forming conditions were more extreme. The slight but consistent increase in the $N_{\rm GC}$ value with age, particularly for galaxies older than 10 Gyr, suggests a fossil imprint of early cosmic conditions. The GC formation might have resulted from more frequent or dominant star formation bursts in systems that formed earlier, likely in high density regions of the cosmic web.

The correlations discussed in this work will need to be explained by the theory of galaxy formation and evolution. Therefore, a useful window into the time and environment of early galaxy formation epochs is provided by the correlation between the ages and $N_{\rm GC}$. The positive correlation between age and $N_{\rm GC}$ is qualitatively consistent with the downsizing scenario. More massive early-type galaxies formed their stars earlier and also assembled more GCs (see Yan et al. (2021); Thomas et al. (2005); Thomas et al. (2010)). However, our partial correlation analysis suggests that age contributes beyond mass alone, indicating a direct link between the formation epoch and the GC formation efficiency.

4. Conclusion

This study clarifies the multitudinous relationships that control the richness of GCs in nearby galaxies. Our expanded parameter, for incorporates dynamic proxies ($R_e \times \sigma$), structural indices (n, α, γ), and the stellar population age, that reveals a more complex story of the GC formation and survival. Although, the established relation for total $N_{\rm GC}$ and the stellar mass remains robust.

Our results has confirmed notion that a galaxy's ability to form, and maintain the GCs is mostly dependent on the gravitational potential rather than just on the baryonic mass. This dynamic correlation is emphasized by a very close relationship for $N_{\rm GC}$ and the product of the effective radius, and velocity dispersion. Also, the supports theoretical models that link halo binding energy to abundance of the GCs. Concurrently, the connections with light profile parameters are observed, particularly the Sérsic index and surface brightness gradients which indicate that internal structure and accumulation history leave distinct imprints on globular clusters.

Perhaps much more interesting is the relation between the number of globular clusters and their age. The consistent rise in the globular cluster number

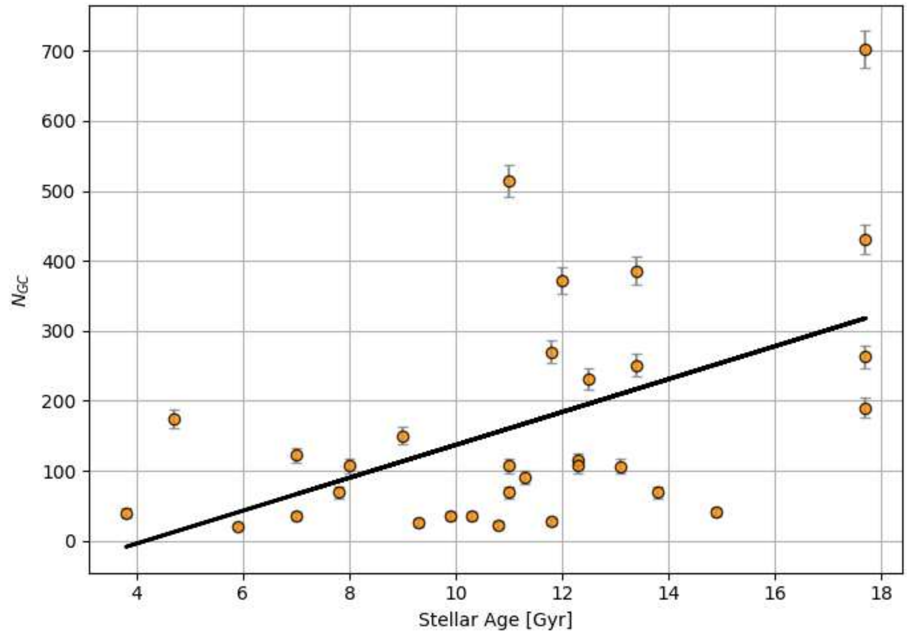

Figure 8. The total number of globular clusters with the age of the stellar population.Vertical error bars represent Poisson uncertainties ($\sqrt{N_{\rm GC}}$). Globular clusters are more common in older galaxies.

with age points to previous systems that most likely developed in denser cosmic environments, creating the perfect circumstances for the production of enormous clusters that are no longer present in the universe.

Acknowledgements. We thank the contributors to the ACSVCS, SLUGGS, and Forbes et al. catalogs for making their data publicly available. This work has benefited from discussions within the international globular cluster research community.

References

Abdullah, A. H. & Kroupa, P., The Dichotomy of the Mass-radius Relation and the Number of Globular Clusters. 2021, *Astronomy Letters*, **47**, 170, DOI:10.1134/S1063773721030014

Al-Mashhadani, L. Y. S. & Abdullah, A. H., A cosmological view for the time-variation of the fundamental constants of nature. 2020, *NeuroQuantology*, **18**, 18, DOI:10.14704/nq.2020.18.12.NQ20233

Ashman, K. M. & Zepf, S. E., The formation of globular clusters in merging and interacting galaxies. 1992, *Astrophysical Journal, Part 1 (ISSN 0004-637X), vol. 384, Jan. 1, 1992, p. 50-61.*, **384**, 50, DOI:10.1086/170850

Berkheimer, J. M., Windhorst, R. A., Harris, W. E., et al., Globular Clusters in the Galaxy Cluster MACS0416 at z= 0.397. 2026, *The Astronomical Journal*, **171**, 48, DOI:10.3847/1538-3881/ae209a

Brodie, J. P., Romanowsky, A. J., Strader, J., et al., The SAGES legacy unifying globulars and galaxies survey (SLUGGS): sample definition, methods, and initial results. 2014, *The Astrophysical Journal*, **796**, 52, DOI:"10.1088/0004-637X/796/1/52

De Bórtoli, B. J., Caso, J. P., Ennis, A. I., & Bassino, L. P., Scaling relations for globular cluster systems in early-type galaxies – II. Is there an environmental dependence? 2022, *Monthly Notices of the Royal Astronomical Society*, **510**, 5725, DOI:10.1093/mnras/stac010

De Lucia, G., Kruijssen, J. M. D., Trujillo-Gomez, S., Hirschmann, M., & Xie, L., On the origin of globular clusters in a hierarchical universe. 2024, *Monthly Notices of the RAS*, **530**, 2760, DOI:10.1093/mnras/stae1006

Dolfi, A., Forbes, D. A., Couch, W. J., et al., The SLUGGS survey: combining stars, globular clusters, and planetary nebulae to understand the assembly history of early-type galaxies from their large radii kinematics. 2021, *Monthly Notices of the RAS*, **504**, 4923, DOI:10.1093/mnras/stab1023

Elmegreen, B. G. & Efremov, Y. N., A Universal Formation Mechanism for Open and Globular Clusters in Turbulent Gas. 1997, *Astrophys. J.*, **480**, 235, DOI:10.1086/303966

Forbes, D. A., Bastian, N., Gieles, M., et al., Globular cluster formation and evolution in the context of cosmological galaxy assembly: open questions. 2018, *Proceedings of the Royal Society of London Series A*, **474**, 20170616, DOI:10.1098/rspa.2017.0616

Forbes, D. A., Ferré-Mateu, A., Durré, M., Brodie, J. P., & Romanowsky, A. J., Keck Cosmic Web Imager (KCWI) spectra of globular clusters and ultracompact dwarfs in the halo of M87. 2020, *Monthly Notices of the RAS*, **497**, 765, DOI:10.1093/mnras/staa1924

Gieles, M., Padoan, P., Charbonnel, C., Vink, J. S., & Ramírez-Galeano, L., Globular cluster formation from inertial inflows: accreting extremely massive stars as the origin of abundance anomalies. 2025, *Monthly Notices of the Royal Astronomical Society*, **544**, 483, DOI:doi:10.1093/mnras/staf1314

Harris, W. E., Harris, G. L., & Hudson, M. J., Dark matter halos in galaxies and globular cluster populations. II. Metallicity and morphology. 2015, *The Astrophysical Journal*, **806**, 36, DOI:10.1088/0004-637X/806/1/36

Harris, W. E. & Van den Bergh, S., Globular clusters in galaxies beyond the local group. I-New cluster systems in selected northern ellipticals. 1981, *Astronomical Journal, vol. 86, Nov. 1981, p. 1627-1642. Research supported by the Canada-France-Hawaii-Telescope Corp. and Natural Sciences and Engineering Research Council.*, **86**, 1627, DOI:10.1086/113047

Hudson, M. J., Gillis, B. R., Coupon, J., et al., CFHTLenS: co-evolution of galaxies and their dark matter haloes. 2015, *Monthly Notices of the Royal Astronomical Society*, **447**, 298, DOI:10.1093/mnras/stu2367

Issa, M. S. & Abdullah, A. H., Physical Properties of Globular Clusters in Several Kinds of Galaxies: A Review. 2024, *Basrah Journal of Science*, **42**, 443, DOI:10.29072/basjs.20240218

Jordán, A., Peng, E. W., Blakeslee, J. P., et al., The ACS Virgo Cluster Survey XVI. Selection Procedure and Catalogs of Globular Cluster Candidates. 2009, *Astrophysical Journal, Supplement*, **180**, 54, DOI:10.1088/0067-0049/180/1/54

Kruijssen, J. D., Pfeffer, J. L., Crain, R. A., & Bastian, N., The E-MOSAICS project: tracing galaxy formation and assembly with the age–metallicity distribution of globular clusters. 2019, *Monthly Notices of the Royal Astronomical Society*, **486**, 3134, DOI:10.1093/mnras/stz968

Le, M. N. & Cooper, A. P., Globular Cluster Counts around 700 Nearby Galaxies. 2025, *Astrophys. J.*, **978**, 33, DOI:10.3847/1538-4357/ad932d

Lim, S., Peng, E. W., Côté, P., et al., The Spatial Distribution of Globular Cluster Systems in Early-type Galaxies: Estimation Procedure and Catalog of Properties for Globular Cluster Systems Observed with Deep Imaging Surveys. 2025, *The Astrophysical Journal Supplement Series*, **276**, 34, DOI:10.3847/1538-4365/ad97b7

Park, S.-M., Shin, J., Smith, R., & Chun, K., Properties of Globular Clusters in Galaxy Clusters: Sensitivity from the Formation and Evolution of Globular Clusters. 2022, *The Astrophysical Journal*, **941**, 91, DOI:10.3847/1538-4357/ac9df9

Thomas, D., Maraston, C., Bender, R., & De Oliveira, C. M., The epochs of early-type galaxy formation as a function of environment. 2005, *The Astrophysical Journal*, **621**, 673, DOI:10.1086/426932

Thomas, D., Maraston, C., Schawinski, K., Sarzi, M., & Silk, J., Environment and self-regulation in galaxy formation. 2010, *Monthly Notices of the RAS*, **404**, 1775, DOI:10.1111/j.1365-2966.2010.16427.x

Valenzuela, L. M., Forbes, D. A., & Remus, R.-S., Globular cluster ages and their relation to high-redshift stellar cluster formation times from different globular cluster models. 2025, *Mon. Not. R. Astron. Soc.*, **537**, 306, DOI:10.1093/mnras/staf015

Yan, Z., Jeřábková, T., & Kroupa, P., Downsizing revised: Star formation timescales for elliptical galaxies with an environment-dependent IMF and a number of SNIa. 2021, *Astronomy and Astrophysics*, **655**, A19, DOI:10.1051/0004-6361/202140683

Contrib. Astron. Obs. Skalnaté Pleso **56/3**, 68 – 82, (2026)
https://doi.org/10.31577/caosp.2026.56.3.68

DSLR times of minima of selected eclipsing binaries

M. Kamenec, P. Gajdoš and Š. Parimucha

Institute of Physics, Faculty of Science, University of Pavol Jozef Šafárik 040 01 Košice, The Slovak Republic (E-mail: matus.kamenec@student.upjs.sk)

Received: June 23, 2026; Accepted: July 6, 2026

Abstract. We present a collection of eclipse timings of eclipsing binary stars obtained over the extended time interval 2014–2024. In all observations, a DSLR camera was used as the detector. The presented dataset contains 250 previously unpublished minima of 86 eclipsing binary systems obtained at three observing sites. The minima were determined from calibrated light curves using the phenomenological modelling approach, and their uncertainties were estimated by bootstrap resampling. The presented measurements extend the available timing coverage of the observed systems and may contribute to future studies of orbital period variations and other long-term phenomena in eclipsing binaries.

Key words: eclipsing binaries – times of minima – digital single lens reflex – photometry

1. Introduction

The rapid development of digital single-lens reflex (DSLR) cameras since the early 2000s has shown that these instruments are useful not only for astrophotography, but also for photometric measurements of variable stars and exoplanetary transits (e.g. Loughney, 2010; Zhang et al., 2016; Kamenec, 2023). Several studies have confirmed that DSLR sensors can serve as practical alternatives to dedicated CCD and, more recently, CMOS cameras (e.g. Zhang et al., 2016; Kamenec, 2023).

Times of minima are among the most important observational quantities in the study of eclipsing binaries. Long-term collections of eclipse timings allow us to investigate orbital period changes caused by light-time effects due to additional companions (Irwin, 1952), apsidal motion in eccentric binaries (Gimenez & Garcia-Pelayo, 1983), dynamical perturbations in multiple systems (Borkovits et al., 2015), mass-transfer processes, and magnetic activity cycles (Applegate, 1992).

In this paper we present 250 DSLR-based times of minima for 86 eclipsing binary systems, obtained between 2014 and 2024. All reported timings are new and have not been published previously. The observations were carried out mainly at the Kolonica Saddle Observatory and at a private observatory in Prešov, with one additional dataset from the observatory in Valašské Meziříčí. The target list was updated continuously based on target visibility, recommendations from the local variable-star community, and the scientific interest of individual systems. We paid particular attention to eclipsing binaries that are regularly monitored because of suspected or known orbital-period variations reflected in their O–C diagrams. Most of the observed targets are short-period systems, which often made it possible to record both primary and secondary minima in a single night, or to observe minima of several different systems consecutively. Since our main goal was to determine eclipse timings rather than to model the light curves in detail, DSLR cameras turned out to be well suited for this kind of work. Timing measurements do not require high-precision multi-band photometry — the time of minimum can be derived reliably from the shape of the eclipse profile even with moderate photometric accuracy.

2. Observation and data reduction

The observations of minima were either planned in advance or obtained as by-products of observations aimed at constructing phase curves and further analysis of selected systems. Observation planning relied on auxiliary tools, namely PozorWin (Pribulla, private communication) and ephemeris predictions available through the International Variable Star Index (Watson et al., 2007). The instrumental setup evolved over the course of the programme; in total, we used two Newtonian reflectors, and one refractor, as summarised in Tab. 1.

Table 1. Telescope systems used for the observations.

System	Telescope	Mount
I	Newton 150/750 mm	EQ3-2 GoTo
II	Apochromatic refractor 102/500 mm	EQ3-2 GoTo
III	Newton 200/1200 mm	NEQ-6

The observing sites are listed in Tab. 2. Kolonica Saddle lies within the Poloniny Dark Sky Park and offers genuinely dark skies, while Prešov and Valašské Meziříčí are situated in urban residential areas and are affected by moderate light pollution.

All observations were made with an uncooled Canon EOS 500D DSLR camera, equipped with a 15.1-megapixel APS-C CMOS sensor measuring 22.3 × 14.9 mm. The detector has a pixel array of 4752 × 3168 pixels with a pixel size of 4.69 μm and 14-bit analogue-to-digital conversion. Like most DSLR sensors, it is covered by a Bayer filter array of red, green, and blue filters placed over individual pixels. Since this filter array cannot be removed, all photometry was performed in the so-called grayscale (or "clear") mode, in which pixel values are recorded regardless of their Bayer-filter colour, allowing the full sensor area to contribute to the photometric signal (Kamenec, 2023).

Table 2. Observing sites.

Site ID	Site	Country	Coordinates	Alt. [m]	SQM	Bortle class
KOL	Kolonica Saddle	Slovakia	48.936N, 22.274E	441	21.89	3
PO	Prešov	Slovakia	48.974N, 21.261E	248	20.26	5
VM	Valašské Meziříčí	Czechia	49.463N, 17.973E	335	20.73	4

Note. Sky Quality Meter (SQM) values in mag arcsec^{-2} and Bortle class values taken from https://www.lightpollutionmap.info/

Both mount control and image acquisition were managed from a computer. ISO settings and exposure times were adjusted for each target to avoid saturation. The observed stars typically fell in the brightness range 10–12 mag, for which ISO settings of 800–1600 and an exposure time of 30 seconds were used. Images were acquired using one of three software packages — MaximDL[1], Astrophotography Tool[2], or CCDCiel[3] — and stored either in native RAW format or directly as FITS files. The computer clock was synchronized using the NetTime[4] software. The acquisition software recorded the UTC start time of each exposure with sub-second precision.

Image processing and calibration were carried out with the Muniwin software package[5] (Hroch, 2014), which natively supports both file formats. All images were calibrated using dark frames and flat fields obtained with the same ISO settings and exposure times as the corresponding science frames; dark frames were recorded at temperatures closely matching those during the observations. As a final step of the reduction, timestamps were converted to Heliocentric Julian Dates (HJD). Standard aperture photometry was then performed, comparison and check stars were selected, and the resulting light curve was constructed and exported for further analysis.

3. Minima times determination

The times of minima were determined from the observed light curves using the phenomenological modelling approach of Mikulášek (2015). In this method, the eclipse profile is approximated by an analytical function that captures the observed shape of the minimum, and the time of minimum is derived as the model parameter corresponding to the centre of symmetry of the eclipse. Because the fit uses the full eclipse profile rather than only observations near the bottom of the minimum, the resulting timings are generally less affected by observational

[1] https://diffractionlimited.com/product/maxim-dl/
[2] https://astrophotography.app/
[3] https://www.ap-i.net/ccdciel/en/start
[4] https://www.timesynctool.com/
[5] https://c-munipack.sourceforge.net/

scatter and incomplete phase coverage. The phenomenological model describes the eclipse shape reliably without requiring any physical modelling of the binary system, and the minimum time follows directly from the fitted profile. This makes the approach both practical and well-suited to datasets of varying photometric quality.

Uncertainties were estimated using a bootstrap resampling procedure following Cagaš & Pejcha (2012). In contrast to analytical error estimates, the bootstrap method derives timing uncertainty directly from the data and therefore naturally reflects the actual noise level, sampling cadence, and photometric quality of each light curve. This generally leads to more realistic uncertainty estimates for eclipse timings (Cagaš & Pejcha, 2012; Efron, 1979; Davison & Hinkley, 1997). All minima presented in Tab. 3 were determined using the same fitting and uncertainty estimation procedure, which ensures consistency across the entire dataset.

Table 3. DSLR times of minima.

HJD	σ_+	σ_-	Type	Site ID	System
W UMa					
2459655.60271	0.00010	0.00009	p	PO	II
RT And					
2456864.48750	0.00011	0.00012	p	KOL	I
2458133.35155	0.00051	0.00050	s	PO	II
2459749.38491	0.00013	0.00012	p	KOL	III
RW Com					
2459750.39162	0.00022	0.00022	p	PO	II
2460100.47968	0.00020	0.00019	p	KOL	III
RZ Com					
2459403.37043	0.00024	0.00024	s	PO	II
SV Cam					
2457240.53436	0.00020	0.00019	p	KOL	I
2457963.48495	0.00036	0.00035	p	KOL	I
2459595.62033	0.00010	0.00010	p	PO	II
SW Lac					
2458134.25625	0.00011	0.00012	p	PO	II
2459512.38900	0.00006	0.00005	p	PO	II
TV UMi					
2457991.43294	0.00174	0.00132	p	KOL	I
TX Cnc					
2458227.39257	0.00047	0.00046	s	PO	II
2460410.39161	0.00031	0.00032	p	KOL	III
TY Boo					
2459420.34065	0.00129	0.00099	p	PO	II

Table 3. Continued.

HJD	σ_+	σ_-	Type	Site ID	System
2460192.27537	0.00021	0.00018	p	PO	II
TY UMi					
2459803.37993	0.00052	0.00052	p	PO	II
TZ Boo					
2457994.39412	0.00024	0.00024	s	KOL	I
2458360.35199	0.00038	0.00116	p	PO	II
2459742.44251	0.00021	0.00020	p	KOL	III
2460170.35273	0.00038	0.00035	p	PO	II
2460175.40441	0.00036	0.00035	p	PO	II
2460181.34458	0.00044	0.00046	p	PO	II
TZ Lyr					
2459811.55309	0.00074	0.00088	p	PO	II
2459870.25284	0.00017	0.00018	p	PO	II
2459871.31030	0.00015	0.00014	p	PO	II
UV Leo					
2458251.37130	0.00025	0.00029	p	PO	II
UV Lyn					
2459667.41873	0.00038	0.00037	p	PO	II
UX UMa					
2459733.37571	0.00035	0.00026	p	PO	II
2459748.51924	0.00017	0.00015	p	PO	II
2460099.38049	0.00014	0.00012	p	KOL	III
VV UMa					
2460435.46899	0.00120	0.00150	s	PO	II
2460443.37132	0.00024	0.00023	p	PO	II
2460445.43294	0.00012	0.00012	p	PO	II
VW Cep					
2459519.40644	0.00028	0.00030	s	PO	II
2459519.26540	0.00000	0.00056	p	PO	II
VW UMi					
2459782.48803	0.00024	0.00021	p	KOL	III
WZ Cep					
2457973.42104	0.00021	0.00022	s	KOL	I
XY UMa					
2458218.34547	0.00019	0.00021	p	PO	II
2458229.36290	0.00013	0.00014	p	PO	II
2459666.59436	0.00061	0.00059	s	PO	II
YY CrB					
2457996.38787	0.00028	0.00025	p	KOL	I

Table 3. Continued.

HJD	σ_+	σ_-	Type	Site ID	System
AA UMa					
2458230.43093	0.00023	0.00026	p	PO	II
2459664.54883	0.00028	0.00028	s	PO	II
2460006.51446	0.00033	0.00019	p	KOL	III
AB And					
2456858.44583	0.00014	0.00014	p	KOL	I
2457577.48605	0.00015	0.00015	s	KOL	I
2458133.23380	0.00010	0.00009	p	PO	II
AC Boo					
2458379.35665	0.00080	0.00043	p	PO	II
2459782.46884	0.00028	0.00024	p	PO	II
2459783.52443	0.00057	0.00056	p	PO	II
2460070.42200	0.00008	0.00010	p	KOL	III
2460171.38856	0.00043	0.00076	s	PO	II
AD And					
2459873.23762	0.00028	0.00027	s	KOL	III
AH Tau					
2458566.28967	0.00009	0.00028	p	PO	II
AO Cam					
2458218.28395	0.00023	0.00024	p	PO	II
2458230.32697	0.00041	0.00059	s	PO	II
2458532.34742	0.00005	0.00079	p	PO	II
2459656.31230	0.00016	0.00015	p	PO	II
2459657.30118	0.00017	0.00017	p	PO	II
2460005.34342	0.00013	0.00013	p	PO	II
AU Ser					
2456867.37266	0.00012	0.00013	p	KOL	I
2458001.35281	0.00062	0.00044	p	KOL	I
2458374.32056	0.00030	0.00034	p	PO	II
2458375.28801	0.00019	0.00040	s	PO	II
2459763.38642	0.00011	0.00010	p	KOL	III
2459767.44550	0.00022	0.00047	s	PO	II
2460057.31694	0.00019	0.00015	s	KOL	III
AV Del					
2459754.39392	0.00162	0.00152	p	KOL	III
2459781.36786	0.00100	0.00109	p	KOL	III
AX Dra					
2460428.50409	0.00009	0.00009	p	KOL	III
2460429.35302	0.00053	0.00117	s	KOL	III
2460435.32036	0.00011	0.00012	p	KOL	III

Table 3. Continued.

HJD	σ_+	σ_-	Type	Site ID	System
AZ Cam					
2459503.28942	0.00047	0.00045	p	PO	II
BD And					
2459811.47406	0.00025	0.00024	s	KOL	III
BE Dra					
2457967.48118	0.00032	0.00033	p	KOL	I
2458382.34409	0.00008	0.00086	p	PO	II
2460445.42959	0.00038	0.00036	s	KOL	III
2460446.47254	0.00028	0.00028	s	KOL	III
BI CVn					
2459402.41870	0.00057	0.00136	p	PO	II
2460122.43049	0.00025	0.00025	p	KOL	III
BS Cas					
2459797.47612	0.00015	0.00017	p	KOL	III
2460134.42994	0.00014	0.00013	p	KOL	III
2460171.42813	0.00020	0.00018	p	KOL	III
BX Peg					
2456865.37891	0.00013	0.00013	p	KOL	I
2457234.40818	0.00030	0.00028	p	KOL	I
2457580.44201	0.00016	0.00016	p	KOL	I
2457939.51836	0.00014	0.00017	s	KOL	I
2458349.34688	0.00017	0.00029	p	KOL	I
2459504.38520	0.00014	0.00015	p	PO	II
2459513.35839	0.00013	0.00018	p	PO	II
BX Tri					
2459519.61286	0.00127	0.00146	p	PO	II
2459824.55583	0.00033	0.00031	p	KOL	III
2459824.45336	0.00066	0.00075	s	KOL	III
2459826.48193	0.00048	0.00038	p	KOL	III
2459826.38027	0.00055	0.00067	s	KOL	III
2459870.29992	0.00065	0.00070	s	KOL	III
2459870.40264	0.00058	0.00048	p	KOL	III
CC Com					
2459658.58499	0.00026	0.00025	p	PO	II
2460006.38161	0.00011	0.00011	p	KOL	III
2460020.28473	0.00010	0.00012	p	KOL	III
CD Cam					
2456746.39357	0.00056	0.00056	p	KOL	I
CE Leo					
2459726.39758	0.00033	0.00034	p	PO	II

Table 3. Continued.

HJD	σ_+	σ_-	Type	Site ID	System
CG Cyg					
2459516.31537	0.00011	0.00012	p	PO	II
2460176.49246	0.00008	0.00009	p	KOL	III
2460177.44011	0.00014	0.00013	s	KOL	III
2460178.38626	0.00011	0.00012	p	KOL	III
2460181.54189	0.00006	0.00007	p	KOL	III
CW Cas					
2458352.34338	0.00042	0.00004	p	KOL	I
2459595.24635	0.00016	0.00016	p	PO	II
2459817.33219	0.00011	0.00013	s	KOL	III
2459817.49015	0.00008	0.00008	p	KOL	III
2459968.30968	0.00013	0.00013	p	KOL	III
2460135.39130	0.00024	0.00022	p	KOL	III
CW Sge					
2460193.48318	0.00074	0.00073	p	PO	II
DL CVn					
2459728.43894	0.00079	0.00072	p	PO	II
DN Cam					
2459664.38402	0.00018	0.00017	s	PO	II
EF Cep					
2459780.42807	0.00019	0.00019	p	KOL	III
EF Dra					
2457975.45834	0.00040	0.00038	p	KOL	I
2459826.35536	0.00039	0.00036	p	PO	II
2460020.56310	0.00041	0.00045	p	KOL	III
2460181.48457	0.00037	0.00040	s	KOL	III
2460184.45217	0.00069	0.00073	s	KOL	III
2460199.50290	0.00041	0.00046	p	PO	II
EP And					
2458354.35106	0.00050	0.00127	p	KOL	I
2459880.26265	0.00023	0.00021	p	KOL	III
ES UMa					
2460176.40850	0.00085	0.00129	p	KOL	III
FU Dra					
2457582.46906	0.00011	0.00011	p	KOL	I
2457987.34091	0.00015	0.00015	p	KOL	I
2457990.40826	0.00014	0.00014	p	KOL	I
2458371.35560	0.00056	0.00047	p	PO	II
2458378.40967	0.00062	0.00016	p	PO	II
2459402.54875	0.00111	0.00105	p	PO	II

Table 3. Continued.

HJD	σ_+	σ_-	Type	Site ID	System
2459403.46734	0.00116	0.00050	p	PO	II
2459404.54407	0.00046	0.00053	s	PO	II
2459404.38927	0.00051	0.00051	p	PO	II
2459824.44214	0.00017	0.00025	s	PO	II
2460007.39824	0.00018	0.00018	p	KOL	III
2460137.44779	0.00008	0.00008	p	KOL	III
2460184.37482	0.00041	0.00039	p	KOL	III
GW Cep					
2457964.41394	0.00019	0.00020	p	KOL	I
2459652.31220	0.00024	0.00025	p	PO	II
2459653.42913	0.00038	0.00040	s	PO	II
2459746.36691	0.00012	0.00011	p	KOL	III
2459797.38000	0.00009	0.00008	p	KOL	III
2459990.27421	0.00017	0.00025	p	PO	II
2459991.23055	0.00020	0.00026	p	PO	II
2460149.37097	0.00017	0.00016	p	KOL	III
GZ And					
2457977.45556	0.00026	0.00028	s	KOL	I
2458532.27716	0.00031	0.00022	s	PO	II
HH UMa					
2458229.47158	0.00072	0.00069	p	PO	II
2460066.37353	0.00069	0.00076	p	KOL	III
HL Dra					
2459513.27802	0.00055	0.00063	p	PO	II
HW Cam					
2459731.45795	0.00029	0.00026	p	PO	II
2459743.46873	0.00046	0.00045	p	PO	II
LO And					
2458353.33715	0.00051	0.00018	p	KOL	I
MZ Dra					
2460320.30591	0.00023	0.00022	p	KOL	III
NR Cam					
2458223.45928	0.00030	0.00031	s	PO	II
2458223.32773	0.00021	0.00022	p	PO	II
2458348.45628	0.00004	0.00052	p	PO	I
2459652.45368	0.00025	0.00029	p	PO	II
2459652.57780	0.00034	0.00038	s	PO	II
2459656.41577	0.00031	0.00030	s	PO	II
2459657.43953	0.00038	0.00039	s	PO	II
2460004.55036	0.00018	0.00021	p	KOL	III

Table 3. Continued.

HJD	σ_+	σ_-	Type	Site ID	System
2460085.53583	0.00024	0.00026	s	KOL	III
2460085.40876	0.00064	0.00086	p	KOL	III
2460408.46246	0.00022	0.00021	s	KOL	III
2460408.59109	0.00021	0.00019	p	KOL	III
NU Cam					
2459659.53924	0.00090	0.00094	s	PO	II
2459660.57469	0.00055	0.00052	p	PO	II
OT Cep					
2459745.43858	0.00014	0.00015	p	KOL	III
OU Ser					
2457991.31317	0.00046	0.00039	s	KOL	I
PP Lac					
2458350.35329	0.00025	0.00020	p	KOL	I
2459504.50295	0.00022	0.00021	p	PO	II
2460097.42480	0.00015	0.00016	p	KOL	III
V339 Boo					
2459748.41925	0.00040	0.00041	p	KOL	III
2459750.41184	0.00054	0.00046	s	KOL	III
V344 Lac					
2459517.35800	0.00047	0.00050	p	PO	II
V380 Dra					
2459452.48806	0.00039	0.00049	s	PO	II
2459461.37468	0.00031	0.00029	s	PO	II
2459462.36228	0.00059	0.00057	s	PO	II
2459466.31405	0.00029	0.00027	s	PO	II
2459484.33453	0.00020	0.00019	p	PO	II
2459835.38068	0.00024	0.00022	p	PO	II
2459869.44827	0.00009	0.00016	p	KOL	I
V401 Cyg					
2460168.48169	0.00017	0.00014	p	KOL	III
V405 Dra					
2460443.45278	0.00018	0.00018	s	KOL	III
V432 Per					
2458531.39429	0.00054	0.00019	p	PO	II
2460194.56876	0.00010	0.00009	p	KOL	III
V483 And					
2459785.44377	0.00022	0.00025	p	KOL	III
2459818.41690	0.00028	0.00029	p	KOL	III

Table 3. Continued.

HJD	σ_+	σ_-	Type	Site ID	System
V508 Oph					
2458377.35657	0.00031	0.00053	p	PO	II
2459441.38432	0.00006	0.00006	p	VM	III
V523 Cas					
2457581.45014	0.00010	0.00011	s	KOL	I
2457965.52716	0.00007	0.00007	p	KOL	I
2458531.30138	0.00035	0.00016	p	PO	II
2459510.47663	0.00016	0.00016	p	KOL	III
2459816.49977	0.00008	0.00008	s	KOL	III
2459816.38322	0.00007	0.00008	p	KOL	III
2459821.52463	0.00010	0.00011	p	KOL	III
2459821.40714	0.00008	0.00007	s	KOL	III
2459828.30184	0.00007	0.00007	p	KOL	III
2459828.41811	0.00007	0.00007	s	KOL	III
2460141.45233	0.00006	0.00006	p	KOL	III
2460193.33312	0.00007	0.00008	p	KOL	III
V584 Cam					
2459595.41453	0.00053	0.00050	p	PO	II
V608 Cam					
2459681.30569	0.00070	0.00072	s	PO	II
2459684.44106	0.00074	0.00071	s	PO	II
2459736.41993	0.00101	0.00136	s	PO	II
2459758.37596	0.00042	0.00047	s	KOL	III
2459796.45937	0.00042	0.00042	s	KOL	III
2459871.28252	0.00058	0.00060	s	KOL	III
2459912.28431	0.00010	0.00010	p	KOL	III
2460086.35476	0.00031	0.00035	s	KOL	III
V651 Cas					
2459513.44400	0.00007	0.00009	p	PO	II
V728 Her					
2459493.29475	0.00054	0.00056	p	PO	II
2459502.25215	0.00051	0.00050	p	PO	II
2459802.47311	0.00062	0.00066	p	PO	II
2460171.49534	0.00056	0.00052	p	PO	II
V781 Tau					
2459666.26558	0.00023	0.00022	p	PO	II
2459667.29945	0.00024	0.00024	p	PO	II
V829 Her					
2457984.42564	0.00035	0.00029	s	KOL	I
2459799.39132	0.00069	0.00068	p	KOL	III

Table 3. Continued.

HJD	σ_+	σ_-	Type	Site ID	System
2460169.36116	0.00050	0.00039	p	PO	II
2460170.43614	0.00037	0.00035	p	PO	II
2460193.35769	0.00044	0.00044	p	PO	II
V857 Her					
2459504.27549	0.00064	0.00047	p	PO	II
2459779.48032	0.00033	0.00035	p	PO	II
V902 Cep					
2459516.52088	0.00040	0.00039	p	PO	II
2459517.50695	0.00033	0.00032	p	PO	II
2459534.27012	0.00068	0.00073	p	PO	II
2459535.26110	0.00054	0.00051	p	PO	II
2459562.37442	0.00059	0.00053	s	PO	II
2460065.45629	0.00028	0.00024	p	KOL	III
2460143.52164	0.00109	0.00106	s	KOL	III
V955 Cep					
2459502.56360	0.00072	0.00073	p	PO	II
V1018 Cyg					
2459486.45833	0.00096	0.00096	p	PO	II
V1191 Cyg					
2457964.52597	0.00023	0.00025	p	KOL	I
V1297 Cas					
2459783.44089	0.00020	0.00022	p	KOL	III
V1918 Cyg					
2456865.47915	0.00017	0.00021	p	KOL	I
2457957.50619	0.00021	0.00021	p	KOL	I
2459512.29336	0.00027	0.00025	p	PO	II
2459517.24954	0.00020	0.00018	p	PO	II
2459866.38306	0.00022	0.00019	p	PO	II
2460075.45112	0.00010	0.00011	p	KOL	III
V2277 Cyg					
2459502.37053	0.00015	0.00020	p	PO	II
NSVS 5789962					
2459461.46165	0.00174	0.00399	p	PO	II
2459466.56294	0.00169	0.00464	s	PO	II

Notes. p and s denote primary and secondary minima, respectively. The columns Site ID and System correspond to Tab. 2 and 1, respectively.
The computer readable form of these data can be found at: `https://www.astro.sk/caosp/Eedition/FullTexts/vol56no3/pp68-82.dat/`.

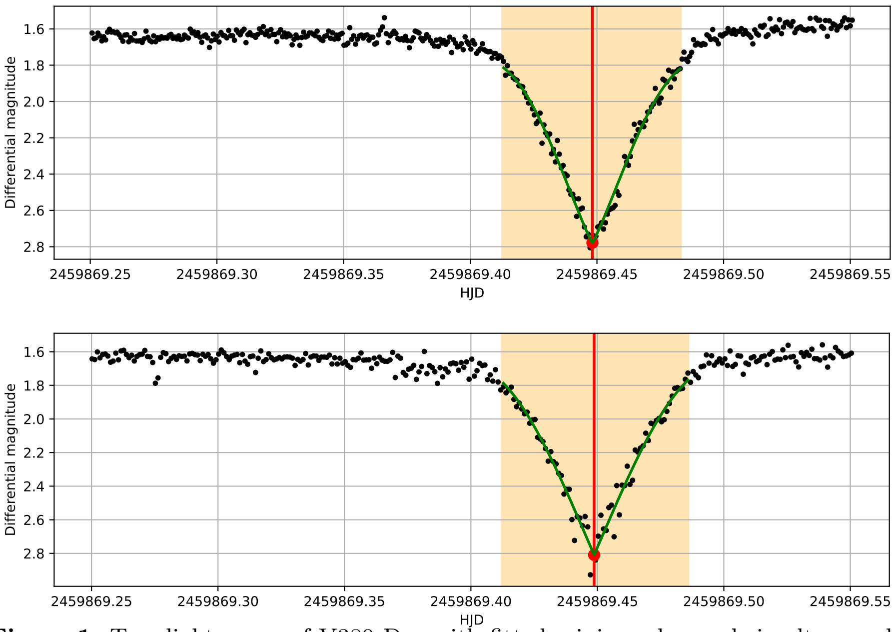

Figure 1. Two lightcurves of V380 Dra with fitted minima observed simultaneously from Kolonica saddle (above) and from Prešov (bottom).

4. Limitations

Several sources of measurement uncertainty are inherent to the use of a DSLR camera as a photometric detector. These include the presence of the Bayer filter array, a lower bit depth compared to dedicated CCD and CMOS cameras, and the absence of sensor cooling, which leads to higher dark current and increased thermal noise — particularly during observations at elevated ambient temperatures. The quantum efficiency of DSLR sensors is also generally lower than that of purpose-built astronomical detectors. Beyond the instrument itself, the observations were acquired under varying conditions, including sites affected by moderate light pollution and changing atmospheric transparency. The observations were also affected by varying atmospheric seeing, although it was not monitored systematically and did not represent a significant limitation for the relatively bright targets included in this study.

To illustrate the effect of observing conditions on DSLR photometry, the same minimum of V380 Dra was observed simultaneously from two sites using different telescope systems: one from Kolonica Saddle within the Dark Sky Park Poloniny, and the other from the urban environment of Prešov (Fig. 1).

As expected, the light curve from the dark-sky site shows noticeably lower point-to-point scatter and a smoother eclipse profile. The urban observation, by contrast, exhibits increased photometric noise, reflecting the combined effect of a brighter sky background, a smaller telescope aperture, and higher detector gain settings. These differences are visible both in the precision of individual measurements and in the uncertainties of the derived eclipse timings (Tab. 4).

Despite the substantially different observing conditions, both datasets produced mutually consistent times of minimum. This comparison shows that DSLR-based eclipse timing remains feasible even in the presence of significant light pollution. While dark-sky observations naturally yield better photometric quality and more precise timing determinations, urban sites can still contribute scientifically useful eclipse timings suitable for long-term period monitoring of eclipsing binaries. For our final compilation, we adopted the timing value derived from the Kolonica Saddle observations.

Table 4. Comparison of two independent observations of the eclipse minimum of V380 Dra obtained under different observing conditions.

Parameter	Kolonica Saddle	Prešov
Site type	Dark-sky site	Urban site
SQM (mag arcsec^{-2})	21.89	20.26
Telescope	Newton 200/1200	APO 102/500
Exposure time (s)	30	60
ISO	800	1800
Point error (mag)	0.005–0.008	0.013–0.016
HJD minimum	2459869.448266	2459869.448703
σ_- (d)	0.0000933	0.0002160
σ_+ (d)	0.0001567	0.0001904

5. Discussion and Conclusions

We have presented a collection of 250 new times of minima for 86 eclipsing binary systems, obtained between 2014 and 2024 using DSLR photometry. All timings were derived from uniformly reduced observations and determined using a consistent fitting and uncertainty estimation procedure, ensuring homogeneity across the entire dataset. The results confirm that DSLR cameras can provide eclipse timings with sufficient precision for many practical applications in eclipsing binary research. While such detectors cannot fully match the performance of modern dedicated CCD and CMOS cameras, they remain a viable and accessible option for long-term photometric monitoring. We have also shown that useful eclipse timings can be obtained not only from dark-sky sites but also from locations affected by moderate light pollution, thereby broadening the potential contribution of amateur and semi-professional observers to this type of systematic monitoring.

The timings presented here extend the available observational coverage of the studied systems and may serve as useful input for future investigations of orbital period variations and other long-term phenomena in eclipsing binaries.

Acknowledgements. The Slovak Research and Development Agency supported this work under contract no APVV-24-0160. M.K. was supported by the internal grant No. VVGS-2025-3480 of the P.J. Šafárik University in Košice.

References

Applegate, J. H., A Mechanism for Orbital Period Modulation in Close Binaries. 1992, *Astrophysical Journal*, **385**, 621, DOI:10.1086/170967

Borkovits, T., Rappaport, S., Hajdu, T., & Sztakovics, J., Eclipse timing variation analyses of eccentric binaries with close tertiaries in the Kepler field. 2015, *Monthly Notices of the RAS*, **448**, 946, DOI:10.1093/mnras/stv015

Cagaš, P. & Pejcha, O., Discovery of a double eclipsing binary with periods near a 3:2 ratio. 2012, *Astronomy and Astrophysics*, **544**, L3, DOI:10.1051/0004-6361/201219815

Davison, A. & Hinkley, D., Bootstrap Methods and Their Application. 1997, *Journal of the American Statistical Association*, **94**, DOI:10.2307/1271471

Efron, B., Bootstrap Methods: Another Look at the Jackknife. 1979, *The Annals of Statistics*, **7**, 1 , DOI:10.1214/aos/1176344552

Gimenez, A. & Garcia-Pelayo, J. M., A New Method for the Analysis of Apsidal Motions in Eclipsing Binaries. 1983, *Astrophysics and Space Science*, **92**, 203, DOI:10.1007/BF00653602

Hroch, F. 2014, Munipack: General astronomical image processing software, Astrophysics Source Code Library, record ascl:1402.006

Irwin, J. B., The Determination of a Light-Time Orbit. 1952, *Astrophysical Journal*, **116**, 211, DOI:10.1086/145604

Kamenec, M., Transformation of DSLR magnitudes to standard photometric system. 2023, *Open European Journal on Variable Stars*, **243**, 1, DOI:10.5817/OEJV2023-0243

Loughney, D., Variable star photometry with a DSLR camera. 2010, *Journal of the British Astronomical Association*, **120**, 157

Mikulášek, Z., Phenomenological modelling of eclipsing system light curves. 2015, *Astronomy and Astrophysics*, **584**, A8, DOI:10.1051/0004-6361/201425244

Watson, C., Henden, A., & Price, A., The International Variable Star Index (VSX). 2007, *Journal of the American Association of Variable Star Observers (JAAVSO)*, **35**, 414

Zhang, M., Bakos, G. Á., Penev, K., et al., Precision Multiband Photometry with a DSLR Camera. 2016, *Publications of the ASP*, **128**, 035001, DOI:10.1088/1538-3873/128/961/035001

PRÁCE ASTRONOMICKÉHO OBSERVATÓRIA
NA SKALNATOM PLESE
LVI, číslo 3

Zostavovateľ:	RNDr. Richard Komžík, CSc.
Vedecký redaktor:	RNDr. Augustín Skopal, DrSc.
Vydal:	Astronomický ústav SAV, Tatranská Lomnica
IČO vydavateľa:	00 166 529
Periodicita:	3-krát ročne
ISSN (on-line verzia):	1336-0337
CODEN:	CAOPF8
Rok vydania:	2026
Počet strán:	84

Contributions of the Astronomical Observatory Skalnaté Pleso are processed using
LaTeX 2_ε CAOSP DocumentClass file 3.10 ver. 2024.